N. Christodoulou,[1] *A. R. Causey,*[1] *R. A. Holt,*[1] *C. N. Tomé,*[2] *N. Badie,*[3] *R. J. Klassen,*[1] *R. Sauvé,*[3] *and C. H. Woo*[2]

Modeling In-Reactor Deformation of Zr-2.5Nb Pressure Tubes in CANDU Power Reactors

REFERENCE: Christodoulou, N., Causey, A. R., Holt, R. A., Tomé, C. N., Badie, N., Klassen, R. J., Sauvé, R., and Woo, C. H, "**Modeling In-Reactor Deformation of Zr-2.5Nb Pressure Tubes in CANDU Power Reactors,**" *Zirconium in the Nuclear Industry: Eleventh International Symposium, ASTM STP 1295*, E. R. Bradley and G. P. Sabol, Eds., American Society for Testing and Materials, 1996, pp. 518–537.

ABSTRACT: Changes in shape of internally pressurized tubes caused by operating temperatures and pressures are enhanced by fast neutron irradiation. Lengths and diameters of Zr-2.5Nb pressure tubes in CANada Deuterium Uranium-Pressurized Heavy Water (CANDU-PHW) power reactors and test reactors have been monitored periodically over the past 20 years. Axial and transverse strain rates have been evaluated in terms of operating variables and the crystallographic texture and anisotropic microstructure of the extruded and cold-drawn tubes. The anisotropic deformation occurring during steady-state irradiation creep and growth is described by a self-consistent model that takes into account the presence of intergranular stresses without building up any discontinuities of strain and stress at the grain boundaries. In this model, it is assumed that climb-assisted glide of dislocations on prismatic, basal, and pyramidal planes is the dominant creep mode and that growth occurs by net fluxes of interstitials and vacancies to a non-random distribution of dislocations and grain boundaries. The predictions from a deformation equation based on data from the Pickering and Point Lepreau Nuclear Generating Stations and the WR1, Osiris, DIDO, and NRU test reactors are in good agreement with measurements of pressure tubes in Bruce units. The equation has been employed as a material subroutine in the 3-D finite element code H3DMAP for predicting the detailed shape change of pressure tubes. The prediction from H3DMAP is a more complete description of shape change than that obtained from the closed-form expression.

KEYWORDS: zirconium alloys, nuclear industry, pressure tubes, in-reactor deformation, irradiation creep, modeling, Zr-2.5Nb, self-consistent, grain interaction stresses, texture, dislocation structure, deformation equation, finite element code

The cold-worked Zr-2.5Nb pressure tubes in service in CANDU reactors undergo irradiation-enhanced changes in shape. Several equations have been proposed to account for the changes in length, diameter, and sag of CANDU pressure tubes in terms of the operating environment and the microstructures produced during fabrication [*1–4*]. These equations have generally described the anisotropic deformation using the concepts of additive separable components [*4,5*] of in-reactor thermal creep, irradiation-induced creep (shape change due to irradiation and

[1] Scientist, senior scientist, branch manager, and scientist, respectively, Reactor Materials Research Branch, Chalk River Laboratories, Chalk River, Ontario, K0J 1J0, Canada.
[2] Scientist and senior scientist, respectively, Reactor Materials Research Branch, Whiteshell Laboratories, Pinawa, Manitoba, R0E 1L0, Canada.
[3] Senior research engineer and principal research engineer, respectively, Ontario Hydro Technologies, 800 Kipling Ave., Toronto, Ontario, M8Z 5S4

applied stress at constant volume), and irradiation growth (shape change due to irradiation in the absence of applied stress at constant volume).

The six main differences between the equation to be presented here and earlier ones [6–8] are: (1) In the past, the anisotropic polycrystalline behavior was predicted using "lower-bound" [1,7] and "upper-bound" [4,8–10] models, which allowed discontinuities of strain or stress at the grain boundaries due to the lack of self-consistency between the deformation of the individual grains and the deformation of the polycrystal. In the development of the present deformation equation, the anisotropy was derived using a self-consistent deformation model [11–15] in which there are no strain or stress discontinuities at the grain boundaries; (2) Due to the lack of irradiation growth data from tests on specimens with the same crystallographic texture and dislocation structure as the power reactor pressure tubes, the relative amounts of creep and growth were not accounted for accurately in the earlier deformation equations; (3) The present equation is based on a data set that includes measurements from both power reactor pressure tubes and small specimens of Zr-2.5Nb pressure tube material in test reactors to much higher fluences than earlier equations; (4) The temperature dependence of the growth term in the present equation was derived from specimens in test reactors and was shown to be negative in contrast to that used in previous equations; (5) The amount of thermal creep is less in this analysis than proposed earlier; (6) The end-to-end variation was determined independently and was not based on an empirical fit to power reactor data.

In this work, strain-producing mechanisms are assumed to operate in each individual crystal, and the sum of strains from all crystals is equal to the observed total deformation measured in the polycrystal. Thus, to predict the total deformation of the polycrystal, a deformation law describing the behavior of single crystals is needed. Three single crystal deformation laws are used: a creep law with a stress exponent larger than 1, a creep law that is linear in stress, and a deformation term due to growth. The self-consistent deformation model was employed in two steps: (1) the thermal creep component of the polycrystal was determined by using a power law describing the single crystal deformation, and (2) the irradiation creep and growth terms were calculated by using a linear creep law and growth law for the single crystal as described in Ref 15.

Pressure tubes in CANDU reactors are typically 6 m in length with an inside diameter of 0.104 m and a wall thickness of 0.0042 m. The internal pressure is about 10 MPa; therefore, under normal operating conditions, the tubes are under an applied hoop stress of about 120 MPa and an axial stress of ~60 MPa. Also, the inlet and outlet temperature in high power channels is about 520 and 562 K, respectively. The data used to derive the values of the constants involved in the equation are measurements of dimensional changes in pressure tubes from the Pickering, Bruce, and Point Lepreau Nuclear Generating Stations (NGS). Creep and growth results from test reactors (i.e., NRU, WR1, OSIRIS in France and DIDO in England) were also used. The equation gives the functional relationships between temperature, T, stress, σ, fast neutron flux, ϕ, and microstructural parameters such as texture, grain size, and dislocation density and can be used to predict the deformation to fluences beyond the envelope of data for current tubes and the behavior of tubes fabricated by different procedures and operated at different conditions.

Pressure Tube Materials

Fabrication procedures and the resulting microstructures of the extruded and cold-worked Zr-2.5Nb tubes have been described in detail elsewhere [4,16]. The major parameters that affect the deformation behavior of the tubes in-reactor are the crystallographic texture and the density and Burgers vectors of the dislocations. The standard pressure tube has the majority of basal poles in the transverse (circumferential) direction in the radial-transverse plane (Fig. 1). The

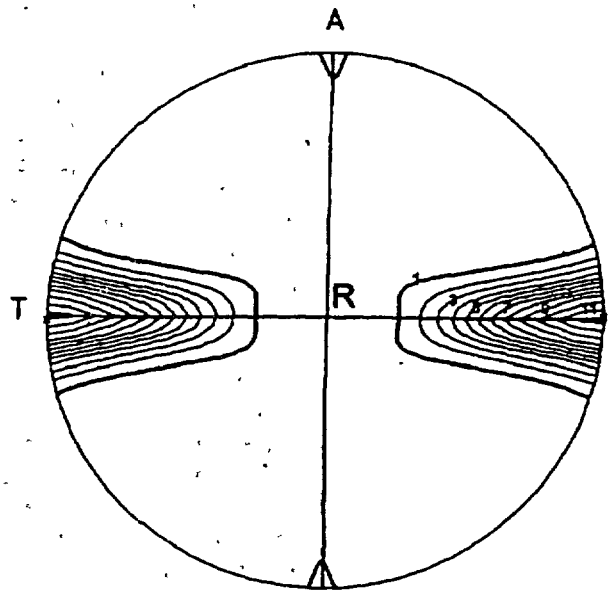

FIG. 1—*A full (0002) pole figure of an "average" Pickering pressure tube. R, T, and A stand for radial, transverse, and axial directions, respectively.*

resolved fractions of basal plane normals in the radial, transverse, and axial directions and the dislocation density of pressure tubes as measured by X-ray line broadening are given in Ref *17*.

The computer code SELFPOLY, based on the self-consistent model needed for deriving the thermal and irradiation creep and growth anisotropy factors, requires as input the crystallographic texture and the average grain shape of the materials considered in the analysis [*14,15*]. Details of the crystallographic texture are presented later. The average grain shape is described in SELFPOLY by the ratio of lengths of unit vectors parallel to the thickness, width, and length of grains in pressure tube materials. The average grain shape used in the derivation of the deformation equation was 0.2/1.0/5.0, respectively, and was established by counting the dimensions of a large number of grains from TEM micrographs [*17*].

Deformation Measurements

The elongation of pressure tubes in CANDU power reactors is measured using equipment and procedures described in Ref *4*. A typical plot of elongation against fluence of a large number of tubes from the Bruce Unit 2 NGS is shown in Fig. 2. The average elongation rate of Pickering reactors used in deriving the constants of the deformation equation is 11.2×10^{-29} m^2/n. The average elongation rates of Bruce and Point Lepreau units, i.e., 11.8 and 13×10^{-29} m^2/n, respectively, were used for comparison with those calculated from the deformation equation to be presented next. The axially averaged fast flux in each type of reactor is 1.96, 2.4, and 2.35×10^{17} n/m^2/s,* respectively. The fast neutron flux peaks at about 2.5, 4, and 3.5×10^{17} n/m^2/s in Pickering, Bruce, and Point Lepreau stations, respectively.

Diameteral profiles along the lengths of the tubes are measured during reactor shutdowns by

* The fast neutron fluxes and fluences mentioned throughout the text are for neutrons with $E > 1$ MeV.

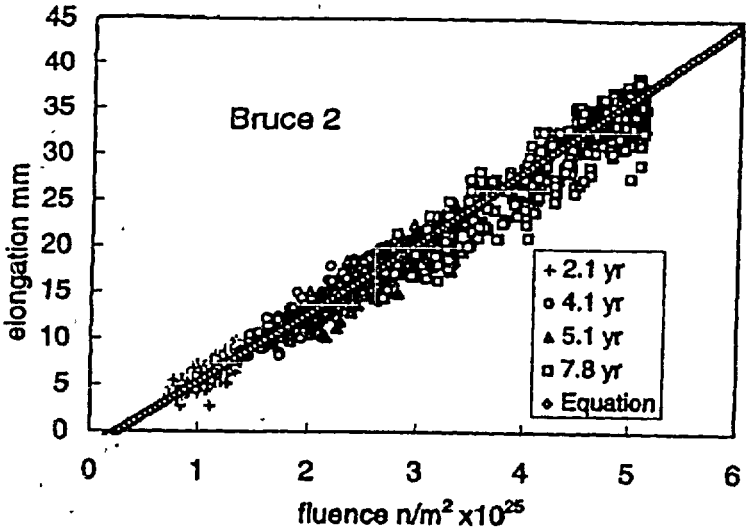

FIG. 2—*Elongation versus fluence of pressure tubes in Bruce Unit 2 power reactor. The line represents the prediction of the deformation equation presented in the Analysis section, as discussed in the Predictions section. The data were not used in deriving the equation.*

passing a gauging tool through the tubes as described in Ref *4*. The strain at the position of the middle of the twelve fuel bundles was plotted against time, and a least squares fit was used to obtain the steady-state strain rates. From the fitting, the strain intercept due to primary creep was also obtained and was related to the steady-state rate by means of a linear expression. A typical example for two Pickering pressure tubes that operated for about 16 years is shown in Fig. 3. Note that tubes with their back ends (i.e., the ends extruded last) at the coolant outlet of the channel exhibit pronounced peaks near the outlet, whereas tubes with their back end at

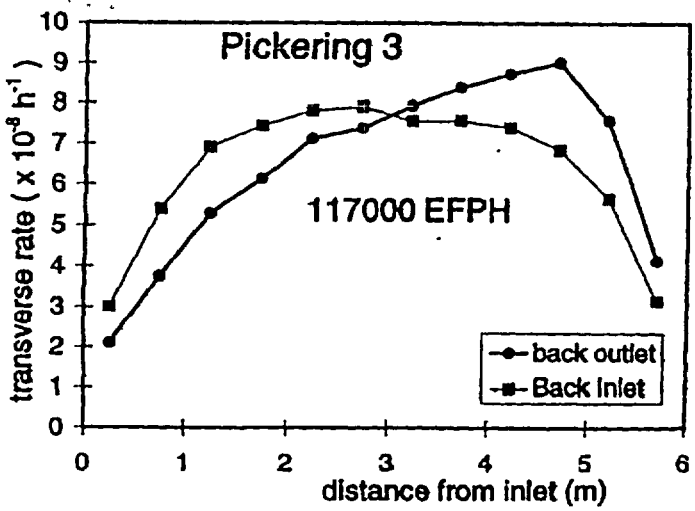

FIG. 3—*Transverse strain rate profile of two Pickering pressure tubes showing two typical types of behavior.*

the coolant inlet have a more uniform strain rate profile [*4*]. As is evident in Fig. 3, the average strain rate increases along the tube from inlet (~523 K) to outlet (~567 K) and is higher in the high flux region of the tube.

Reference irradiation creep rates and creep compliances have been determined experimentally from shear (i.e., springs loaded in tension), bent-beam stress relaxation experiments, and internally pressurized creep capsules [*15*]. In addition, Causey et al. [*18*] measured experimentally irradiation creep rates and creep compliances as a function of stress and temperature on internally pressurized capsules from Zr-2.5Nb micropressure tube material that had the same crystallographic texture and dislocation density as typical pressure tubes. These capsules were irradiated to higher fluences than those described in Ref *15* in the OSIRIS reactor at a fast flux of about 1.8×10^{18} n/m^2/s. The results from these tests were used to verify the predictions from the deformation equation described next.

Irradiation growth data were obtained from Ref *19*, and a typical example (Fig. 4) shows the axial growth behavior of two specimens from a pressure tube irradiated in the DIDO test reactor. Although a linear expression appears to reproduce the measurements fairly accurately, a statistically better fit to the data is obtained if it is assumed that the growth rate changes somewhat with fluence. This apparent increase of growth rate with fluence has also been observed in Zircaloy-2 pressure tubes and has been attributed to an increase with irradiation of the ⟨c⟩ component dislocation density as discussed by Griffiths et al. [*20*]. Thus, the present equation allows for the possibility that the growth rate depends on fluence, unlike the previous one [*4*] where the growth rate was assumed to remain constant with fluence.

Thermal creep is a small, but not a negligible component of strain during irradiation. Two sets of data were used to estimate the magnitude of the in-reactor thermal creep term. For the temperature range between 520 to 570 K, the set of data used here was obtained from the periodic gauging of a pressure tube installed in the NRU reactor and operated for about 54 000 h. The strain profile of the tube included sections where the flux was nearly zero and the creep rate was a minimum [*3*] due to radiation hardening from which the thermal component could be established. Figure 5 shows the evolution of strain with time at the minimum creep locations

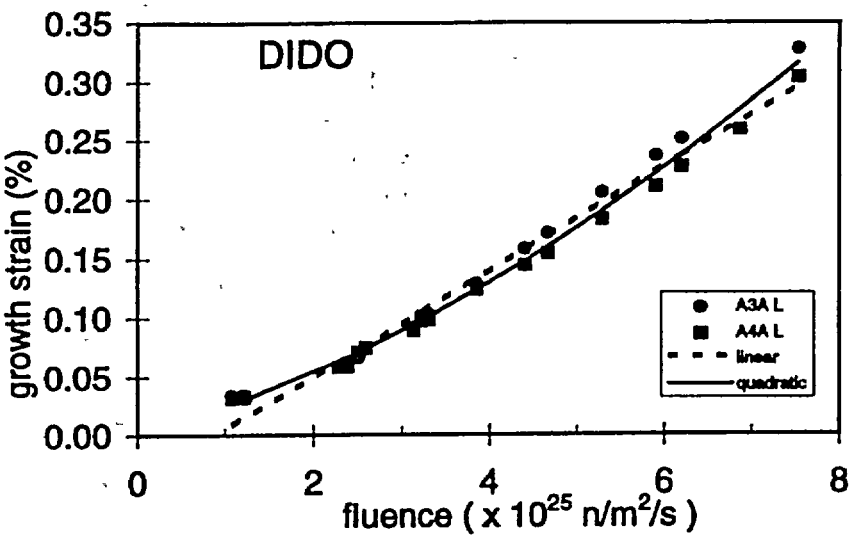

FIG. 4—*Dependence of growth strain on fluence of two pressure tube samples from the longitudinal direction irradiated at DIDO [19]. The best linear and quadratic fits to the data are also shown.*

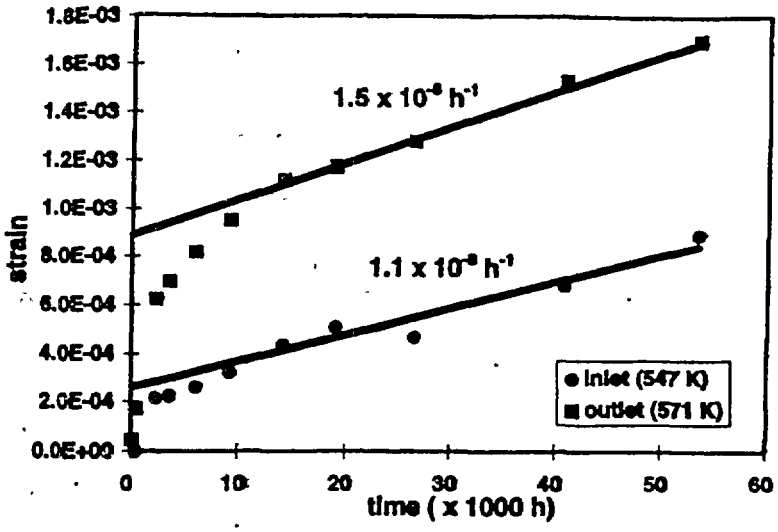

FIG. 5—*Thermal creep strain as a function of time at the inlet and outlet of a NRU pressure tube. The creep rates indicated on the figure were used in Eq 1.*

at the inlet and outlet ends. The steady-state thermal creep rates quoted in the figure were the values used to derive the parameters for the thermal component for the temperature range mentioned above. The contribution due to primary creep is less than 5% of the total strain, and it was neglected. For temperatures in the range of 570 to 680 K, creep rates from pressure tubes operated in the WR1 reactor at Whiteshell and from uniaxial creep tests in NRU were used [*4*].

Analysis

The complex interaction between the effects of temperature and fast neutron flux on the deformation of zirconium alloys has led to the development of analyses that assume that long-term steady-state deformation consists of separable, additive components from thermal creep, irradiation creep, and irradiation growth [*3–5*]. All components are anisotropic and contribute to length as well as diameter changes. The equation describing the deformation of pressure tubes has the form:

$$\dot{\varepsilon}_d = \dot{\varepsilon}_d^{\text{thermal}} + \dot{\varepsilon}_d^{\text{creep}} + \dot{\varepsilon}_d^{\text{growth}} \tag{1}$$

where

$$\dot{\varepsilon}_d^{\text{thermal}} = [K_1 C_1^d \sigma_1 + K_2 C_2^d \sigma_2^2] \exp(-Q_1/T) + K_3 C_1^d \sigma_1 \exp(-Q_3/T) \tag{1a}$$

$$\dot{\varepsilon}_d^{\text{creep}} = K_c K_4(x)\, C_4^d(x)\, \sigma(x)\, \phi\, [\exp(-Q_4/T) + K_5] \tag{1b}$$

$$\dot{\varepsilon}_d^{\text{growth}} = K_g K_6(x,\phi t)\, C_6^d(x)\, \phi \exp(-Q_6/T) \tag{1c}$$

The in-reactor thermal creep component has two terms [*3,4*] that dominate at temperatures above and below 570 K, respectively. The last two terms describe flux-dependent creep and irradiation growth, respectively. The stress exponent for thermal creep varies with stress: for

stresses below 120 MPa, the stress exponent is 1, while for stresses between 120 and 200 MPa, the stress exponent increases to 2 [3]. The parameters in Eq 1 are defined as follows:

$\dot{\varepsilon}_d$ = strain rate in a direction d (i.e., radial, transverse, axial), h^{-1},
$\dot{\varepsilon}K_1$, K_2 = constants for high-temperature in-reactor thermal creep,
K_3 = constant for low-temperature in-reactor thermal creep,
$K_4(x)$ = a function describing the variation of irradiation creep due to variations of microstructure along the length of the tube,
$K_6(x,\phi t)$ = a function describing the variation of irradiation growth due to variations of microstructure along the length of the tube as a function of fluence,
C_1^d, C_2^d = anisotropy factors due to texture for in-reactor thermal creep in a given direction d and for Stress Exponents 1 and 2, respectively,
$C_4^d(x)$, $C_6^d(x)$ = anisotropy factors due to texture for irradiation creep and growth, respectively, in a given direction d along the length of the tube,
K_c, K_g = constants for irradiation creep and growth, respectively,
Q_1, Q_3, Q_4, Q_6, K_5 = activation temperatures and constant, respectively,
σ_1, σ_2 = effective stresses for thermal creep and Stress Exponents of 1 and 2, MPa,
$\sigma(x)$ = effective stress for irradiation creep, MPa,
T = temperature in K,
ϕ = fast flux, $n/m^2/s$ ($E > 1$ MeV), and
t = irradiation time in s.

The equivalent stresses σ_1, σ_2, and $\sigma(x)$ are related to the radial, axial, and transverse stress σ_r, σ_a, and σ_t, respectively, by means of the Hill's anisotropy constants [21], namely:

$$\sigma_i = [F_i (\sigma_a - \sigma_t)^2 + G_i (\sigma_t - \sigma_r)^2 + H_i (\sigma_r - \sigma_a)^2]^{1/2} \quad (2)$$

The subscript i stands for 1 (i.e., $n = 1$), 2 ($n = 2$), or in the case of irradiation creep $\sigma_i = \sigma(x)$. The Hill's anisotropy constants for irradiation creep depend on the distance, x, from the back end of the tubes, and for a 6-m tube this dependence is given by:

$$\begin{aligned} F(x) &= F^b + (F^f - F^b)\, x/6 \\ G(x) &= G^b + (G^f - G^b)\, x/6 \\ H(x) &= 1.5 - F(x) - G(x) \end{aligned} \quad (3)$$

where F^b, F^f, G^b, and G^f are the values of Hill's anisotropy constants F and G at the back and front end of the tube. The dependence of Hill's anisotropy constants F_i, G_i, and H_i ($i = 1, 2$) on x was neglected because of the relatively small magnitude of the thermal component. Using the terminology employed in Eq 2, the anisotropy factors due to texture for in-reactor thermal or irradiation creep are given by:

$$\begin{aligned} C_i^r &= [H_i (\sigma_r - \sigma_a) - G_i (\sigma_t - \sigma_r)] \\ C_i^t &= [G_i (\sigma_t - \sigma_r) - F_i (\sigma_a - \sigma_t)] \\ C_i^a &= [F_i (\sigma_a - \sigma_t) - H_i (\sigma_r - \sigma_a)] \end{aligned} \quad (4)$$

Here $i = 1, 2$, or (x). The coefficient describing the end-to-end effect of irradiation creep along the length of the tube is given by:

$$K_4(x) = K_{4-1} + K_{4-2}\,x \tag{5}$$

The growth coefficient describing the end-to-end effect and the dependence of growth on fluence is given by:

$$K_6(x,\phi\,t) = (K_{6-1} + K_{6-2}\,x)\,(1 + C/B\,[\phi\,t]) \tag{6}$$

where K_{4-1}, K_{4-2}, K_{6-1}, and K_{6-2} are defined later. The growth anisotropy factors are given by:

$$\begin{aligned} C_6^a(x) &= G_a^b + (G_a^f - G_a^b)x/6 \\ C_6^t(x) &= G_t^b + (G_t^f - G_t^b)x/6 \\ C_6^r(x) &= -\,C_6^a(x) - G_6^t(x) \end{aligned} \tag{7}$$

Here (G_a^b, G_t^b) and (G_a^f, G_t^f) are the growth anisotropy constants in the back and front end, and in the axial and transverse direction of the tube, respectively. It should be noted that there is a systematic variation of crystallographic texture along the length of pressure tubes. The dependence of the creep and growth anisotropy factors $C_4^i(x)$ and $C_6^i(x)$ on x is due only to measured texture variations. The axial dependence of $K_4(x)$ and $K_6(x)$ represents the effects of microstructural variations, e.g., dislocation density and grain size. $K_4(x)$ was determined from experimental data and $K_6(x)$ from a growth model.

Derivation of Constants

Hill's Anisotropy Constants

The computer code SELFPOLY, based on the self-consistent model described in Refs *11* to *14*, was used to derive the creep constants (F^b, F^f, G^b, G^f) in Ref *15*. These constants are used in Eqs 3 and 4 to calculate the creep anisotropy constants and coefficients. SELFPOLY requires, as input, the crystallographic texture of pressure tubes in the form of a crystallite orientation distribution function (CODF). The (0002), $(10\bar{1}0)$, $(11\bar{2}0)$, $(11\bar{2}2)$, and $(10\bar{1}1)$ pole figures were determined by X-ray diffraction from 23 Pickering tubes and then were used as input to a computer code that calculates three Euler angles as a function of the volume fraction [22]. The Euler angles were calculated according to Bunge's notation [*23*], and they relate the coordinate system associated with each grain to that of the pressure tube [*14*]. The average value of the resolved basal pole fraction in the radial, transverse, and axial directions, f_R, f_T, and f_L, in the back end and front end of pressure tubes is 0.36, 0.60, 0.05 and 0.30, 0.64, 0.06, respectively. The eigenvalues of the single crystal creep compliance tensor describing pyramidal, prismatic, and basal climb-assisted glide of dislocations in pressure tube materials during in-reactor deformation were derived in Ref *15*, and they are 0.284, 7.086, and 2.84×10^{-30} m^2/n/MPa, respectively. Experimental data from internally pressurized capsules, stress relaxation specimens, and data from the Pickering NGS were used to derive these values in Ref *15*.

A non-linear self-consistent code based on a model described in Ref *24* was used to calculate Hill's thermal creep anisotropy constants F_i, G_i, and H_i, where $i = 1, 2$. As was mentioned above, the single crystal creep law assumed to describe the behavior of the material during

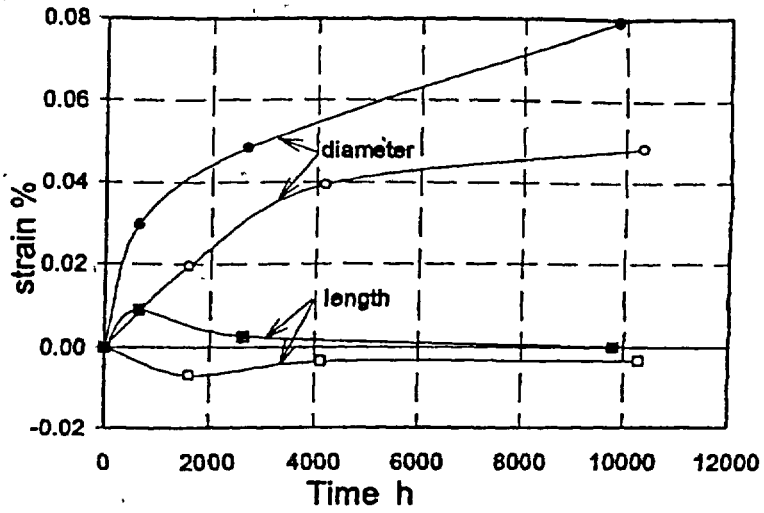

FIG. 6—*Out-reactor creep behavior of internally pressurized capsules from pressure tube material tested at 573 K. Solid symbols correspond to a hoop stress of 175 MPa, while open symbols correspond to a hoop stress of 100 MPa. Note that the strain in the axial direction is much lower than the strain in the transverse direction.*

thermal creep is a power law [*24*]. When the stress is below 120 MPa, the term with $n = 1$ dominates, while when the stress is larger than 200 MPa, the term with $n = 2$ is dominant. The single crystal creep parameters needed for the derivation of Hill's anisotropy constants are the values of critical resolved shear stresses (CRSS) for dislocation glide on prismatic, basal, and pyramidal planes. The values of these three parameters used here are 100, 120, and 240 MPa, respectively. These constants were derived so that the predicted behavior of the polycrystalline material is consistent with out-reactor thermal creep experiments on internally pressurized capsules from small tubes with textures and microstructures like pressure tube materials. Results from out-reactor creep experiments are shown in Fig. 6.

Growth Anisotropy Constants

The values of growth constants (G_r^b, G_t^f, G_a^b, G_a^f) that define the anisotropy factors in Eq 7 were calculated by using SELFPOLY as well. The growth anisotropy of pressure tube materials irradiated in test reactors [*19*] was predicted by using the CODF defined earlier, the single crystal creep compliances mentioned above, and a single crystal growth tensor equal to $(-1.42, 2.13, -0.71) \times 10^{-29}$ m^2/n.

End-to-End Effect

The function $K_4(x)$ in Eq 5 was determined from in-reactor bent-beam stress relaxation tests of pressure tube materials obtained from different locations along the tube. In these tests, the measured deformation rate is due only to irradiation creep and not growth [*25*]. The axial variation in $K_4(x)$ with respect to the middle of the tube was determined from the best fit to the data shown in Fig. 7 to be about ±17%. The end-to-end variation in $K_6(x)$ (i.e., the first term in Eq 6) was calculated from the variation in grain thickness along the length of the tube and the dependence of growth rate on grain thickness [*26*]. The average grain thickness in the front

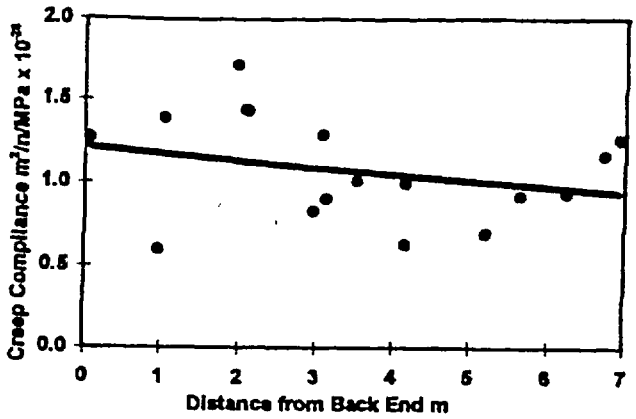

FIG. 7—*Dependence of the axial creep compliance with distance from the back end of the tube.*

end of pressure tubes used here is about 0.39 μm, while that in the back end is about 0.27 μm. The dependence of growth rate on grain thickness is derived from Fig. 18 in Ref *26* and is shown here in Fig. 8. Using the average grain thickness for the front and the back of a pressure tube, the variation of growth rate along the tube with respect to the middle of the tube is about ±8%. The end-to-end effect for creep and growth is shown in Fig. 9. Finally, the dependence of K_6 on ϕt is determined from a number of samples from pressure tube materials mentioned in Ref *19*. The constants (K_{4-1}, K_{4-2}) and (K_{6-1}, K_{6-2}) in Eqs 5 and 6 are the intercept and the slope, respectively; of the two lines in Fig. 9.

Creep and Growth Constants

After determining the above-mentioned constants, the creep and growth constants K_c and K_g were calculated by fitting the diametral and elongation data available from the Pickering NGS. These values were used in Eq 1 to predict the creep compliance in the axial and transverse

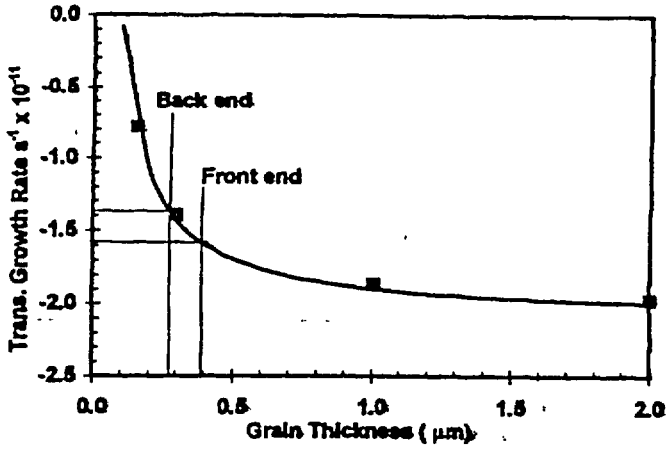

FIG. 8—*Dependence of the transverse growth rate on grain thickness (derived from Ref* 26*).*

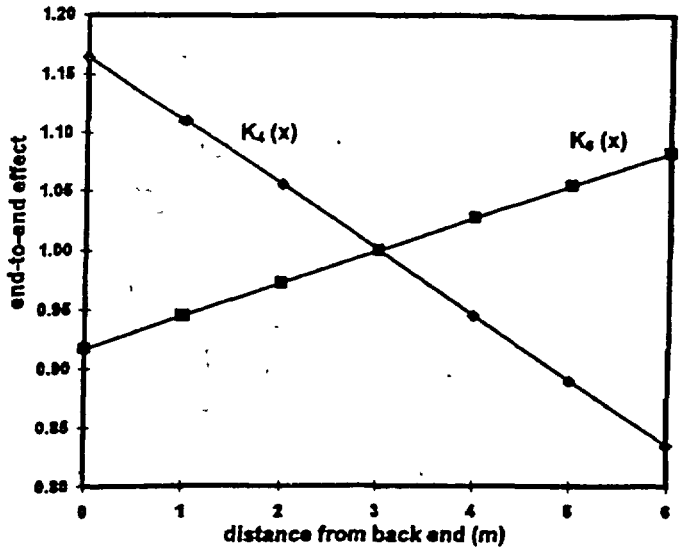

FIG. 9—*End-to-end effect along the length of a pressure tube for the creep and the growth terms in Eq 1.*

directions of micropressure tube material tested in OSIRIS [*18*] and the growth rate of pressure tube materials tested in OSIRIS and DIDO [*19*]. The agreement of the predictions with the measurements was good.

Temperature Dependence

The high-temperature thermal creep term in Eq 1 reflects the high-temperature dependence of creep rate exhibited by the pressure tubes in the WR1 reactor and by the uniaxial creep specimens tested in the NRU reactor (Fig. 1 in Ref *3*). The value of Q_1 that fits the data best is equal to 17 000 K. The value of Q_3 in the low-temperature thermal creep term is derived from Fig. 5 and is equal to 1000 K.

The temperature dependence of creep was derived from power reactor data and that for growth was derived from specimens irradiated in the OSIRIS reactor [*19*] after first removing the thermal creep contribution. Q_4 and K_5 were found equal to 9900 K and 1.1×10^{-7}, respectively, whereas Q_6 is about -3000 K. The temperature dependence of creep does not differ significantly from that in Ref *4*; however, that of the growth component is strongly negative compared to a positive value that was proposed in Ref *4* on the basis of growth data for cold-worked Zircaloy-2 pressure tube material.

Predictions

Using the parameters mentioned above, the predicted deformation rate from Eq 1 is compared to measured values as shown in the following figures. Figure 10 shows the predicted diametral profile of a Pickering tube with its back end in the outlet that was gauged at various time intervals. Figure 11 shows the prediction of the diametral profile of a Pickering tube with its back end in the inlet. In both cases, the calculated rate profile compares well with the measurements. Figure 12 depicts the predicted versus the measured diametral rates for a number

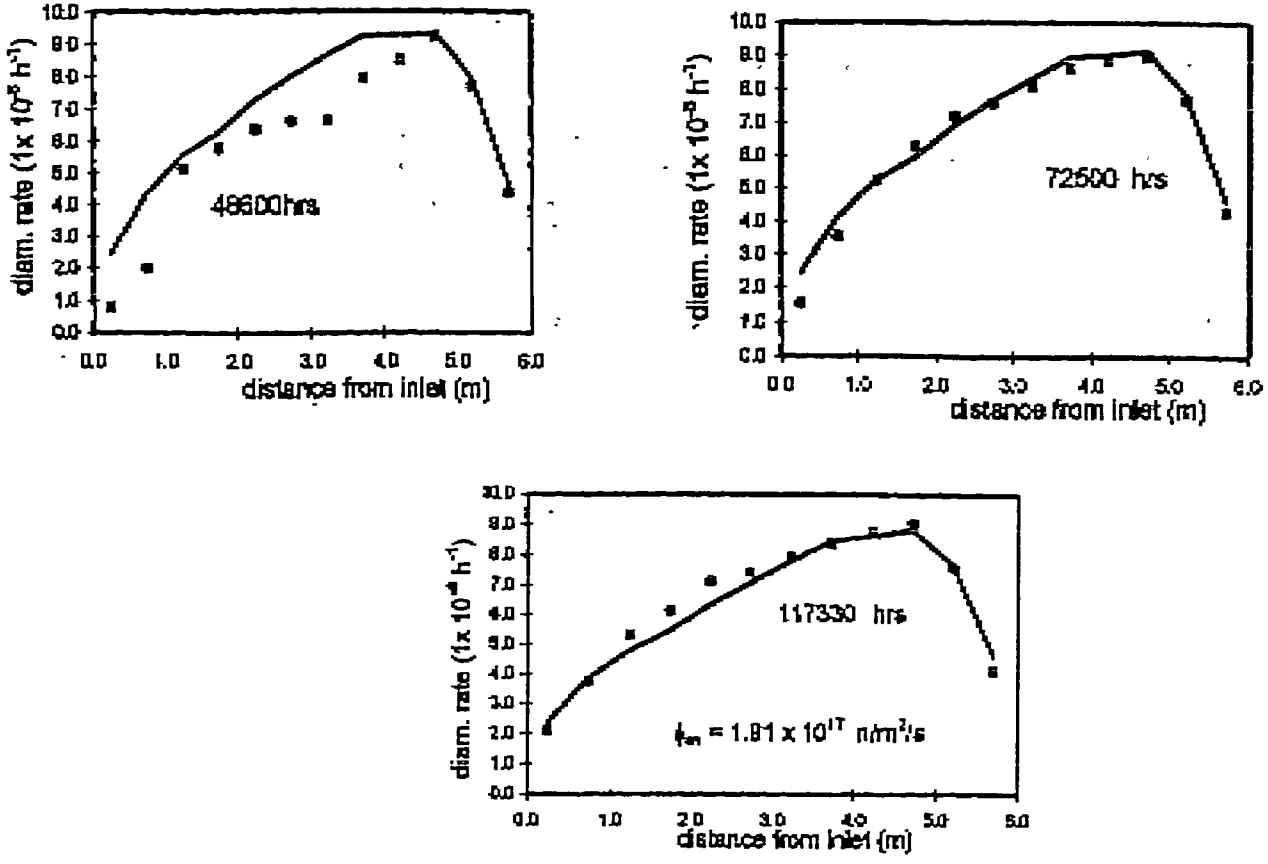

FIG. 10—*Comparison of the predicted diametral rate profile at various time intervals with measurements from a Pickering pressure tube with its back end in the outlet.*

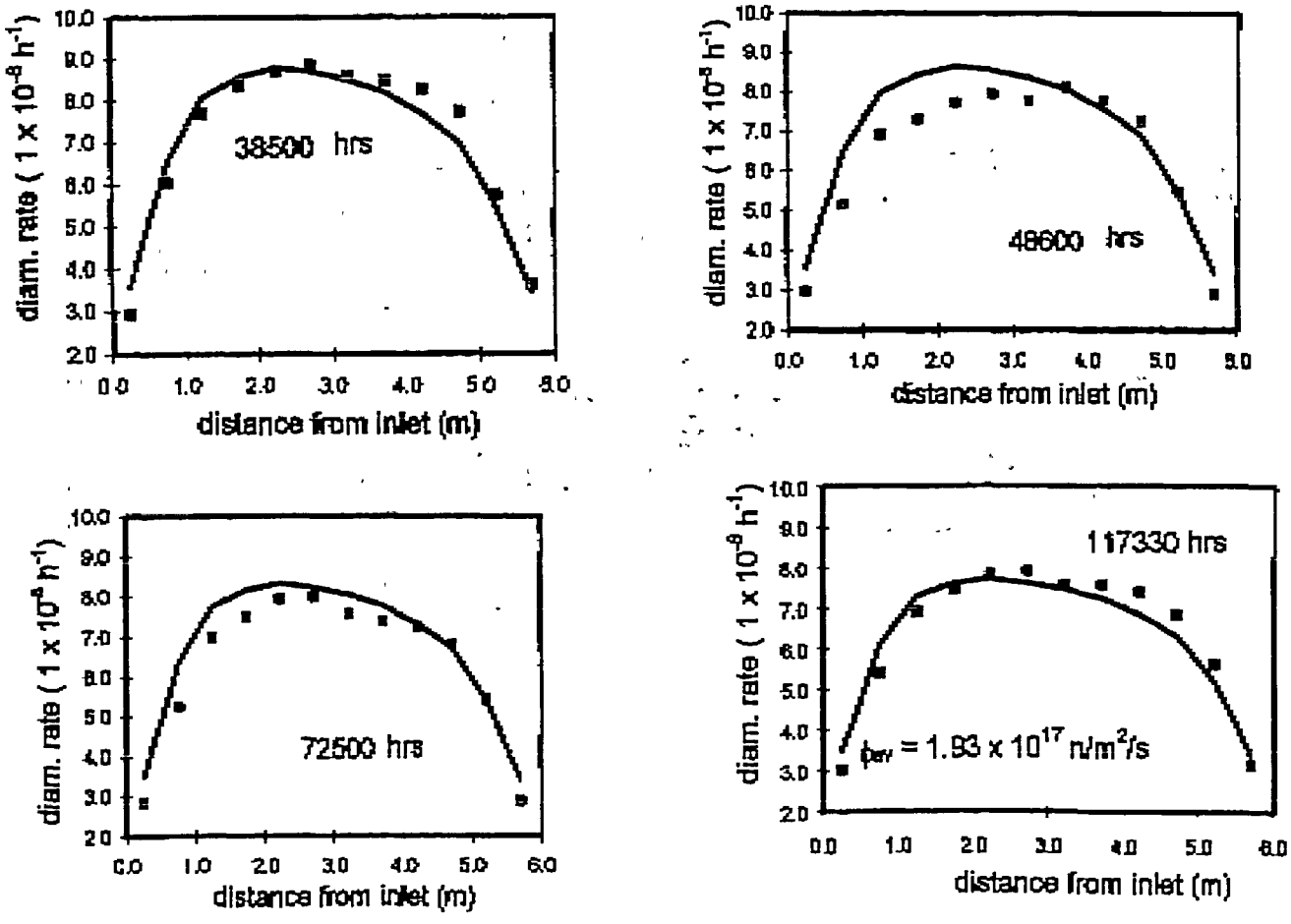

FIG. 11—*Comparison of the predicted diametral rate profile at various time intervals with measurements from a Pickering pressure tube with its back end in the inlet.*

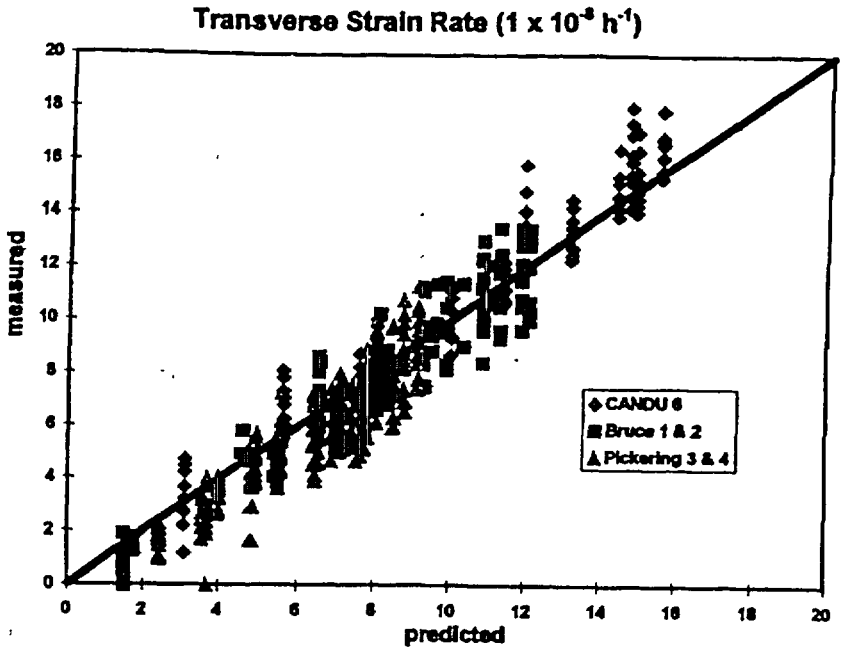

FIG. 12—*Predicted against measured diametral rate in Pickering, Bruce, and CANDU 6 units.*

of tubes from CANDU 6, Bruce, and Pickering units. It should be noted, however, that, for a number of tubes in channels with a low average flux, the prediction is consistently higher than the measurements. This is shown in Fig. 13. Figure 14 shows the measured versus the calculated diametral rate of the pressure tubes irradiated in the WR1 reactor. Finally, Fig. 2 summarizes the elongation of a number of Bruce unit 2 tubes as compared with the elongation predicted from Eq 1. It appears that, in most cases, the predicted deformation rate agrees well with the measurements.

The predictive capability of Eq 1 was also tested by calculating the creep and growth anisotropy factors from SELFPOLY by using the individual crystallographic texture of each tube that was available. Generally, the calculated diametral profile of the deformation rate along the tube was improved as compared to that calculated by employing the coefficients of the "average" tube. In the worst cases, a quantitative overall fit to the deformation rate could be obtained by modifying the amounts of creep and growth, i.e., the values of K_c and K_g in Eqs 1b and 1c by the order of $\pm 10\%$ of the values used for the "average" tube. Therefore, the present deformation equation can be used to predict the behavior of individual tubes to within about $\pm 10\%$ if the creep and growth anisotropy factors of the tube are determined by SELFPOLY and subsequently used in the equation.

3-D Finite Element Code H3DMAP

A finite element code (FEC) H3DMAP developed earlier [27] was used to simulate a complete fuel channel, namely, the pressure tube, calandria tube, part of the end-fitting of the channel, and the spacers that are placed along the tube. The deformation Eq 1 was incorporated into H3DMAP for predicting the detailed shape change after irradiation of a typical pressure tube. In addition to the diametral and length changes, the predictions from the FEC also yield

nd CANDU 6 units.

however, that, for a
sistently higher than
versus the calculated
', Fig. 2 summarizes
elongation predicted
agrees well with the

eep and growth an-
exture of each tube
ion rate along the
ients of the "av-
on rate could be
K_c and K_g in Eqs
e. Therefore, the
ıual tubes to within
are determined by

d to simulate a com-
ıe end-fitting of the
q 1 was incorporated
of a typical pressure
n the FEC also yield

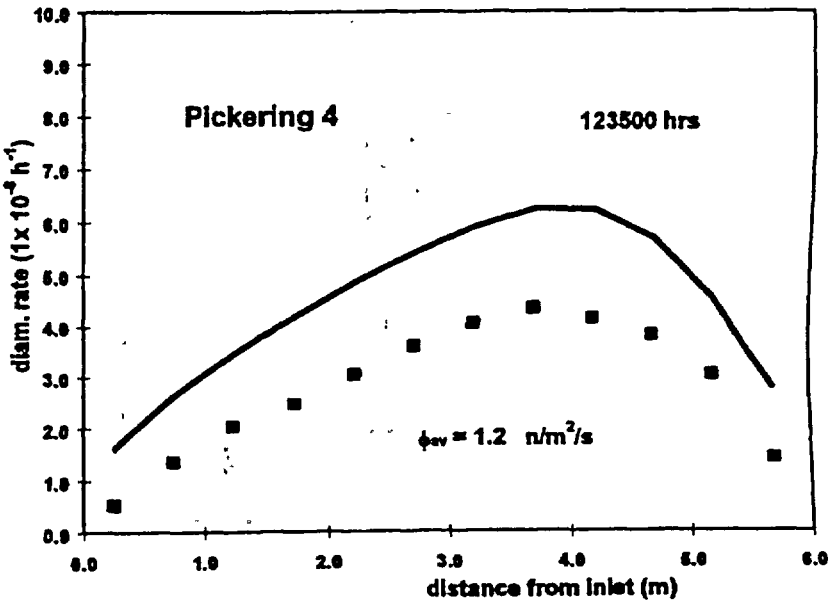

FIG. 13—*Prediction of diametral rate of a low flux channel in Pickering Unit 4. This is selected to show how a low-flux channel does not agree well with the prediction. Other tubes in high-flux channels have a good agreement.*

predictions about the sag of calandria tubes (i.e., deflection from the horizontal plane), information not directly available from the closed form expression (Eq 1).

A comparison between the calculated and the diametral profile measured in situ in a Pickering fuel channel after ten years of operation is shown in Fig. 15*a*. The calculation shows agreement

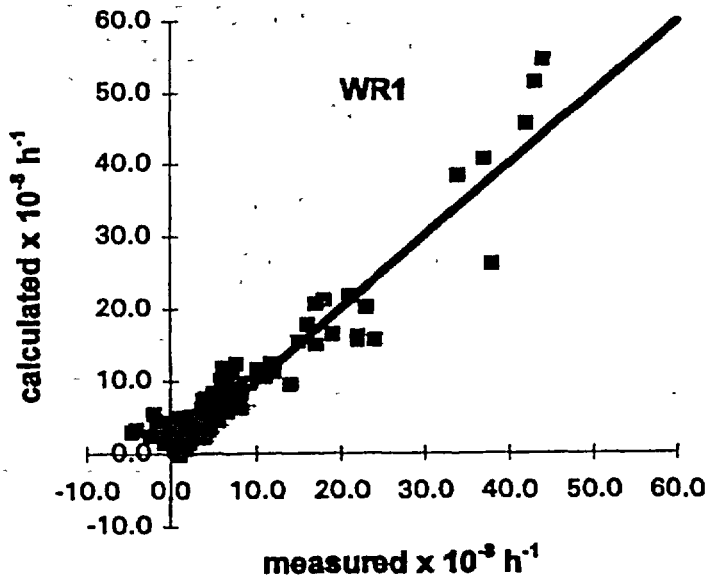

FIG. 14—*Measured versus calculated diametral rate of the WR1 pressure tubes.*

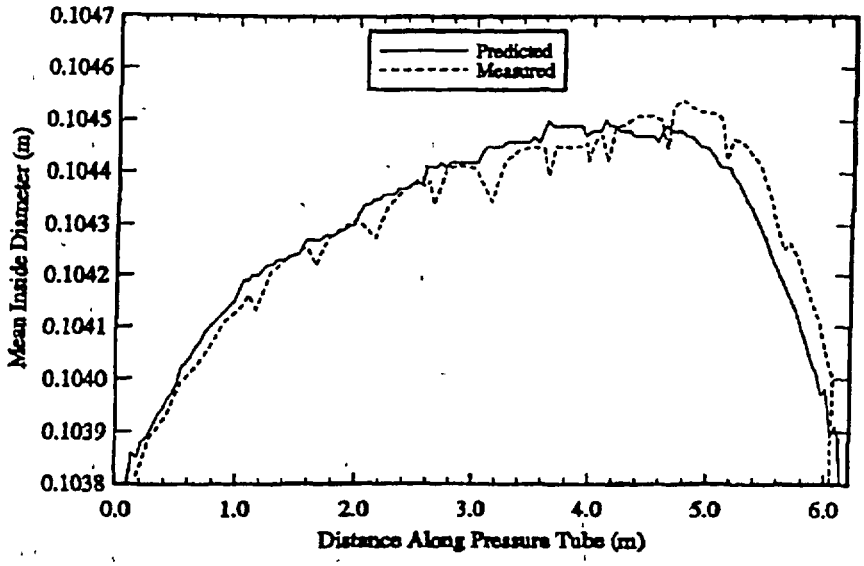

FIG. 15*a*—*Diametral profile of a Pickering pressure tube after ten years of operation. The calculated curve was determined from H3DMAP with Eq 1 as a materials routine.*

with both the average profile (Fig. 15*a*) and the ovality (difference between the diameter at the horizontal and vertical planes) at ~2.5 and 4.0-m positions, developed where the pressure tube is supported by the spacers separating it from the calandria tube (Fig. 15*b*). Note that the measurement shows residual ovality as installed along the whole length of the tube, whereas the calculation shows only the ovality developed during service. Also, from Fig. 15*b*, the section of the tube not supported by the spacers appears to develop a small negative ovality, probably as a response to the large positive values observed at the location of the spacers.

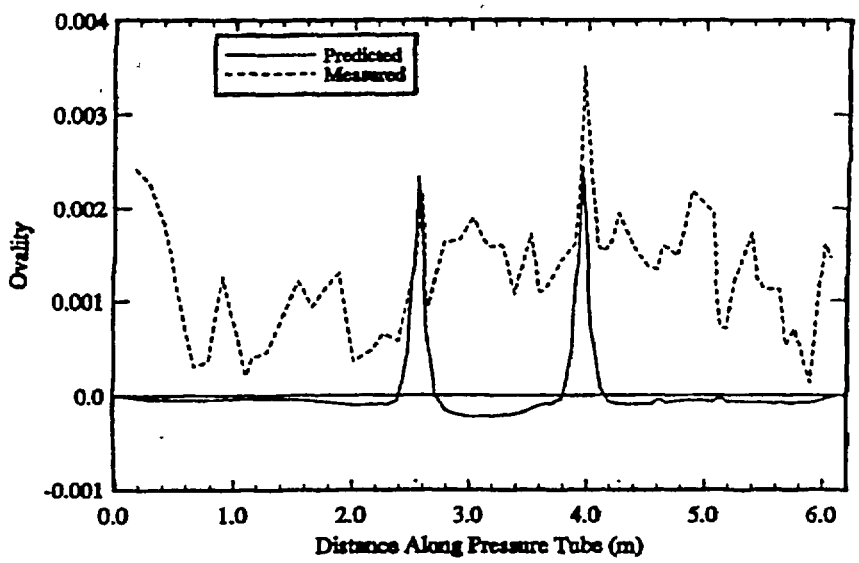

FIG. 15*b*—*Ovality profile for the pressure tube depicted in Fig. 15a.*

Discussion

Equation 1 is similar in form and was derived in a comparable manner to that described in Ref *4*. Deformation due to irradiation creep and growth and due to thermal creep is assumed to be the result of strain-producing steps due to climb and glide of dislocations primarily on prismatic systems [*15*] and to some degree on pyramidal systems. As in Ref *4*, in the present equation the creep and growth anisotropy factors were derived from a model that takes into account the crystallographic texture, the interactions between grains, and the stresses that develop as a result of these interactions. When grain interactions are considered, specimens with randomly oriented grains have the minimum average strain rates. In contrast, materials with anisotropic single crystal properties and with non-random texture are strengthened in one or two directions and are weakened in the other directions. The major difference between the anisotropy model used for the derivation of Ref *4* and Eq 1 is that in the former analysis all grains were subjected to the same amount of deformation, namely, that of the polycrystal. As a result of this assumption, there are stress discontinuities that develop from grain to grain. In the self-consistent model used here [*11–15*] for the derivation of the present equation, the weighted average of the sum of strains (or stresses) from all the crystals is equal to the overall strain (or imposed stress) of the polycrystal. In this fashion, there are no stress or strain discontinuities from grain to grain.

The approach developed here results in a different set of creep and growth anisotropy factors from that derived in Ref *4*. In contrast to the equation in Ref *4*, the temperature dependence of growth is strongly negative in the present model, whereas it was positive in Ref *4*. Furthermore, the relative amounts of creep and growth are different in the present equation compared to that proposed earlier. For instance, in the previous version of the deformation equation, axial growth accounted for about 89% of the total axial strain (Table 2 in Ref *28*), whereas growth contributes only 24% to the total axial rate in Eq 1. Also, both the negative contribution of growth and the positive contribution of creep to the total diametral strain rate are smaller with Eq 1 than with the earlier model, i.e., in Eq 1 transverse growth and creep are about 24 and 67%, respectively, of the values predicted by the equation in Ref *4*. These differences change the predicted effect of stress on the deformation of the pressure tubes. For example, Eq 1 predicts that a 1.9-kN (20%) higher compressive stress than the earlier model must be applied in order to eliminate the axial elongation completely in a Pickering tube after 117 000 h of operation than the value estimated from the previous equation, and the effect of a small increment of internal pressure on the diametral strain rate is 10 to 15% higher with Eq 1 than with the earlier model.

The present equation is derived on the basis of a single set of parameters based on experimentally determined textures and deformation data from a large number of Pickering 3 and 4 pressure tubes. In the earlier version, different sets of parameters were employed for different reactors. The present model is reasonably successful in predicting deformation rates in other reactors and in predicting the deformation behavior of individual tubes when the creep and growth anisotropy constants for the tube are employed instead of those for the "average" tube. Hence, the predictions for individual reactors could probably be improved by using a statistically significant sampling of textures of tubes from each reactor.

As mentioned above, it appears that the prediction of the diametral strain rates is consistently higher than the measurements in some cases, especially for channels with a low average flux or when the measurement was obtained after a short irradiation period. This may be attributed to an overestimate of the contribution of thermal creep, which was derived by assuming that the thermal creep rate varies linearly from the inlet to outlet between the values indicated in Fig. 5. However, the degree of suppression of the thermal creep rate in the presence of a high fast flux has not been established, and it is possible that thermal creep is reduced further with

a high fast neutron flux than at the edges of the core where the fast flux is as low as 1% of that at the center of the tube.

Unlike the earlier model [4], the effects of the variation in dislocation density and grain size along the length of the tubes on the creep and growth rates was based on independent experimental measurements and models and not on an empirical fit to the power reactor data. These effects are of the order of ±17 and ±8% for creep and growth, respectively, and their magnitude was sufficient to reproduce the difference between the diametral profiles of tubes with their back ends in the inlet or outlet flow of the channels.

The finite element formulation provides detailed information about various aspects of both the pressure tube and calandria tube deformation, such as the ovalization of the pressure tube at the spacers. Some of the results can be compared with in-reactor or post irradiation measurements, while others can be used to gain insight into aspects of deformation that are not routinely examined (e.g., horizontal deflection) or difficult to measure (e.g., stress distributions).

Conclusions

1. A database of changes in length and diameter of Zr-2.5Nb pressure tubes during service in power and test reactors was correlated to the operating conditions and microstructure of the tubes. This database extends to much higher fast neutron fluences than were previously available [4].
2. A self-consistent polycrystalline model proposed earlier has been employed to calculate the anisotropy of creep and growth from the preferred orientation of grains and the resulting grain interactions under a fast neutron flux.
3. A deformation equation describing anisotropic thermal creep and irradiation creep and growth under normal operating conditions in CANDU reactors has been derived using the data mentioned in Conclusion 1 and the polycrystalline model mentioned in Conclusion 2.

   a. The thermal creep strain is assumed to be the result of slip of ⟨a⟩ type dislocations gliding on prismatic planes and ⟨c+a⟩ type dislocations gliding on pyramidal planes. The dependence of the thermal creep rate on stress has two contributions, i.e., at low values of stress, a stress exponent of 1 dominates, and at higher values a stress exponent of 2 dominates.
   b. The irradiation creep strain is assumed to be the result of climb-assisted glide of ⟨a⟩ and ⟨c+a⟩ type dislocations operating on prismatic, basal, and pyramidal planes, and the irradiation creep rate is linearly dependent on stress.
   c. The growth rate was based on new growth data obtained from CANDU pressure tube material irradiated to high fluences in DIDO and OSIRIS. The polycrystalline growth anisotropy factors were calculated by means of the self-consistent model.

4. The effect of variations of dislocation density and grain size along the length of the tube were determined independently from the power reactor data.
5. The equation has been incorporated in a finite element code and was used for predicting the shape change of the tubes in more detail.

Acknowledgments

The authors would like to thank the CANDU Owners Group, Working Party 32, for financial support.

References

[1] Holt, R. A. and Ibrahim, E. F. in *Acta Metallurgica*, Vol. 27, 1979, p. 1319.
[2] Ibrahim, E. F. and Holt, R. A. in *Journal of Nuclear Materials*, Vol. 91, 1980, p. 311.
[3] Holt, R. A., Causey, A. R., and Fidleris, V. in *Proceedings of the British Nuclear Society*, London, 1983, p. 175.
[4] Causey, A. R., Fidleris, V., MacEwen, S. R., and Schulte, C. W. in *Influence of Radiation on Material Properties: Thirteenth International Symposium, ASTM STP 956*, American Society for Testing and Materials, West Conshohocken, PA, 1988, p. 54.
[5] Nichols, F. A. in *Journal of Nuclear Materials*, Vol. 30, 1969, p. 249.
[6] MacEwen, S. R. and Carpenter, G. J. C. in *Journal of Nuclear Materials*, Vol. 90, 1980, p. 108.
[7] Causey, A. R., Holt, R. A., and MacEwen, S. R. in *Zirconium in the Nuclear Industry (Sixth International Symposium) ASTM STP 824*, American Society for Testing and Materials, West Conshohocken, PA, 1985, p. 269.
[8] Holt, R. A. and Causey, A. R. in *Journal of Nuclear Materials*, Vol. 150, 1987, p. 306.
[9] Savino, E. J. and Laciana, C. E. in *Journal of Nuclear Materials*, Vol. 90, 1980, p. 89.
[10] Savino, E. J. and Harriague, S. in *Effect of Radiation on Materials: Twelfth International Symposium, ASTM STP 870*, American Society for Testing and Materials, West Conshohocken, PA, p. 667.
[11] Woo, C. H. in *Journal of Nuclear Materials*, Vol. 131, 1985, p. 105.
[12] Woo, C. H. in *Proceedings of the British Nuclear Society*, London, 1987, p. 65.
[13] Causey, A. R., Woo, C. H., and Holt, R. A. in *Journal of Nuclear Materials*, Vol. 159, 1988, p. 225.
[14] Tomé, C. N., So, C. B., and Woo, C. H. in *Philosophical Magazine*, Vol. 67, 1993, p. 917.
[15] Christodoulou, N., Causey, A. R., Woo, C. H., Tomé, C. N., Klassen, R. J., and Holt, R. A., *Effects of Radiation on Materials (Sixteenth Volume), ASTM STP 1175*, American Society for Testing and Materials, West Conshohocken, PA, 1994, p. 1111.
[16] Holt, R. A. in *Journal of Nuclear Materials*, Vol. 59, 1976, p. 234.
[17] Chow, P. C. K., Coleman, C. E., Holt, R. A., Sagat, S., and Urbanic, V., *Effects of Radiation on Materials (Sixteenth Volume), ASTM STP 1175*, American Society for Testing and Materials, West Conshohocken, PA, 1994, p. 1077.
[18] Causey, A. R., Elder, J. E., Holt, R. A., and Fleck, R. G., *Zirconium in the Nuclear Industry (Twelfth Volume), ASTM STP 1245*, American Society for Testing and Materials, West Conshohocken, PA, 1994, p. 202.
[19] Fleck, R. G., Elder, J. E., Causey, A. R., and Holt, R. A., *Zirconium in the Nuclear Industry (Twelfth Volume), ASTM STP 1245*, American Society for Testing and Materials, West Conshohocken, PA, 1994, p. 168.
[20] Griffiths, M., Holt, R. A., and Rogerson, A. in *Journal of Nuclear Materials*, in press.
[21] Hill, R., *The Mathematical Theory of Plasticity*, Oxford University Press, London, 1954.
[22] Root, J. H. and Holden, T. M., "Programs to Determine the CODF from Diffraction Intensity Pole Figures," March 1990, unpublished report ANDI-29, available from the Scientific Document Distribution Office, AECL, Chalk River, Ontario, K0J 1J0.
[23] Bunge, H.-J., *Texture Analysis in Materials Science, Mathematical Methods*, Butterworths & Co., London, 1982.
[24] Hutchinson, J. W. in *Proceedings of the Royal Society of London*, Vol. A 348, 1976, p. 101.
[25] Kreyns, P. H. and Burkart, M. W. in *Journal of Nuclear Materials*, Vol. 26, 1968, p. 87.
[26] Holt, R. A. in *Journal of Nuclear Materials*, Vol. 159, 1988, p. 310.
[27] Sauvé, R. G. and Badie, N., *Pressure Vessel and Piping*, Vol. 265, 1993, p. 267.
[28] Holt, R. A. and Fleck, R. G. in *Zirconium in the Nuclear Industry (Ninth Volume), ASTM STP 1132*, American Society for Testing and Materials, West Conshohocken, PA, 1991, p. 218.

DISCUSSION

A. T. Motta[1] *(written discussion)*—(1) Assuming there is a departure from linearity in the growth coefficient showing a dependence on fluence, what is the reason for assuming that such dependence is linear? Or non-linear? (2) What is the reason for a negative temperature dependence of growth?

N. Christodoulou et al. (authors' closure)—(1) A possibility for a non-linear fit to the growth data is the generation of <c>-component dislocation loops that can result in an increase in the growth rate during irradiation. However, from a physical model, the growth rate may saturate at large fluences. (2) This observation stems from experimental measurements (see Holt and Fleck, ASTM STP 1132, page 218, Fig. 8). A physical explanation for the fluence dependence of the growth rate was given by Holt and Fleck in ASTM STP 1023, page 705, Table 4.

S. Yagnik[2] *(written discussion)*—Would your model (DAD) also predict non-linear growth in CWSRA Zr-4 at higher temperatures of irradiation (~600 to 625 K)?

N. Christodoulou et al. (authors' closure)—Very likely, acceleration would occur in material with relatively low levels of cold work and fewer *c* than *a* dislocations initially. However, in a heavily cold-worked material, it is conceivable that the initial *c* dislocation density could be high enough that little acceleration or even a deceleration could occur.

A. T. Motta[1] *(written discussion)*—Does the fact that you have used DAD to explain your results mean that one does not need the production bias model to rationalize the irradiation growth data?

R. A. Holt et al. (authors' closure)—In the temperature range of interest, we think that DAD and not "production bias" is the dominant mechanism; however, the principle that the growth rate will be a maximum when the sink strength of two competing types of sinks are equal should also apply to production bias.

[1] Pennsylvania State University, University Park, PA.
[2] Electric Power Research Institute, Palo Alto, CA.

R. A. Holt,[1] *A. R. Causey,*[1] *M. Griffiths,*[1] *and E. T. C. Ho*[2]

High-Fluence Irradiation Growth of Cold-Worked Zr-2.5Nb

REFERENCE: Holt, R. A., Causey, A. R., Griffiths, M., and Ho, E. T. C., **"High-Fluence Irradiation Growth of Cold-Worked Zr-2.5Nb,"** *Zirconium in the Nuclear Industry: Twelfth International Symposium, ASTM STP 1354,* G P. Sabol and G. D. Moan, Eds., American Society for Testing and Materials, West Conshohocken, PA, 2000, pp. 86–104.

ABSTRACT: Irradiation growth specimens manufactured from cold-worked Zr-2.5Nb pressure tube material have been irradiated in Osiris at a fast flux of $\sim 1.8 \times 10^{18}$ n·m^{-2}·s^{-1}, $E > 1$ MeV, at nominal temperatures of 553 and 583 K, to growth strains of 1%. The pressure tubes have a pronounced crystallographic texture, with ~95% of the basal plane normals in the radial/transverse plane, predominantly in the transverse direction. Both longitudinal specimens, which generally exhibit positive growth strains, and transverse specimens, which generally exhibit negative strains with approximately 50% of the magnitude of the axial strains, show nonlinear growth, the rate increasing gradually with fluence up to 1.3×10^{26} n·m^{-2}, $E > 1$ MeV (580 K) and 1.7×10^{26} n·m^{-2}, $E > 1$ MeV (550 K).

The previously reported temperature dependence of the axial growth strains (decreasing with increasing temperature for fluences up to 4 to 5×10^{25} n·m^{-2}, $E > 1$ MeV) is maintained to the higher fluences now achieved, as is the effect of Fe (axial growth strains decreasing with increased Fe concentration in the range 380–1090 ppm by wt.). The effects of temperature and Fe in the transverse direction are approximately the reverse of those in the longitudinal direction.

Examination by transmission electron microscopy and X-ray diffraction of Zr-2.5Nb pressure tubes irradiated to 1×10^{26} n·m^{-2}, $E > 1$ MeV, at 520 to 570 K in power reactors, and fracture toughness specimens machined from pressure tubes and irradiated, unstressed, in Osiris to 1.5×10^{26} n·m^{-2}, $E > 1$ MeV, at 530 K, shows a multiplication of the c-component dislocations with increasing fast fluence. This contrasts with a rapid saturation of the density of a-type dislocations after about 0.1×10^{26} n·m^{-2}, $E > 1$ MeV.

The multiplication of the c-component dislocations occurs mainly by nucleation of vacancy loops on screw dislocations; this mostly occurs in crystals with their c-axes close to the radial direction because they tend to contain many c-component screw dislocations. Crystals with their c-axes close to the transverse direction contain fewer screw dislocations and exhibit less dislocation multiplication over the fluence range studied. Thus, the gradual evolution of the growth rate with fluence appears to be related to the gradual increase in the c-dislocation density with time as in the case of Zircaloy-2.

KEYWORDS: zirconium alloys, Zr-2.5Nb, pressure tubes, irradiation growth, temperature, neutron fluence, iron, nuclear materials, radiation effects

Zr-2.5Nb pressure tubes for CANDU reactors are manufactured by extrusion of hollow β-forged billets at a temperature of about 1090 to 1120 K, i.e., in the (α + β)-phase field. The tubes are then cold-drawn about 27% to give a final tube thickness of about 4.5 mm and inside diameter of about 104 mm. The grain structure resulting from extrusion consists of

[1] Division director and senior researchers, respectively, Fuel Channels Division, AECL Chalk River Laboratories, Chalk River, Ontario, Canada.
[2] Senior researcher, Ontario Hydro Technologies, Toronto, Ontario, Canada.

thin, platelet-like, hexagonal close-packed (hcp) α-zirconium grains (containing up to about 1 wt% Nb) interspersed with a network of metastable body-centered-cubic (bcc) β-zirconium (containing about 20 wt% Nb) corresponding with the composition at the monotectoid point of the Zr-Nb phase diagram. The metastable β-phase filaments subsequently decompose partially during the final stress-relief treatment for 24 h at 400°C to give a mixture of Nb-depleted hcp ω-phase embedded in the remaining Nb-enriched bcc β-phase.

The α-grains are mostly oriented with $\{11\bar{2}0\}$ prism planes perpendicular to the radial direction, $\{10\bar{1}0\}$ prism planes perpendicular to the longitudinal direction, and (0001) basal planes perpendicular to the transverse direction, although there is a range of basal pole orientations spreading from the transverse to the radial direction in the radial-transverse plane. Most of the α-grains with basal poles oriented towards the transverse direction are nearly parallel with the tube surface and have aspect ratios of about 1:5-10:20-40 in the radial, transverse, and longitudinal directions, respectively. Others that have basal poles oriented towards the radial direction are either kinked platelets or have different aspect ratios grains (1:1-2:5-10) so that they appear almost equiaxed when viewed along the axis of the tube.

The final cold-draw introduces a high density of dislocations. The dislocation structure of the α-grains consists of a mixture of a- and c-component dislocations with densities of about 4 and 1 × 10^{14} m^{-2}, respectively [*1*].

During operation of a CANDU reactor, the cold-worked Zr-2.5Nb pressure tubes are expected to operate to high fluences at temperatures of about 520 to 585 K and pressures of about 10 MPa in a fast neutron flux of about 4 × 10^{17} $n \cdot m^{-2} \cdot s^{-1}$ (all neutron fluxes and fluences in this paper are for $E > 1$ MeV). The tubes elongate and expand diametrally during service due to irradiation creep and growth. An irradiation program has been in progress to characterize the long-term dimensional changes of pressure tube materials. Previous results to a fluence of 4 × 10^{25} $n \cdot m^{-2}$ [*2*] showed that the longitudinal growth was a decreasing function of temperature and Fe concentration. Similar growth experiments on cold-worked Zircaloy-2 [*3*] revealed that the longitudinal growth is nonlinear to a fluence of ~10^{26} $n \cdot m^{-2}$, the growth curves having a small positive curvature, that can be related to an increase in the density of c-component dislocations. The possibility of a similar effect in Zr-2.5Nb was noted in Ref *4*.

This paper describes the temperature dependence, Fe dependence, and fluence dependence of growth of Zr-2.5Nb pressure tube material in the longitudinal and transverse directions at 553 to 583 K for fluences up to 2.3 × 10^{26} $n \cdot m^{-2}$.

Experimental

Irradiation Growth

The irradiations in the Osiris reactor were performed in two NaK-filled stainless steel inserts which have been described previously [*2*]. The temperatures were controlled with heaters surrounding the inserts, and the nominal operating temperatures were 553 and 583 K in inserts referred to as Trillium 2 and Trillium 3, respectively. The inserts comprise seven tiers in-core, each of which contains one creep capsule and six growth specimens. The temperature at each tier was monitored continually by a thermocouple located close to the creep capsule and to one of the growth specimens. The time-averaged temperatures for the growth specimens in each tier for each irradiation phase are given in Table 1. The time-averaged temperature for each tier over the whole irradiation varies from 538 to 568 K in Trillium 2 and from 560 to 585 K in Trillium 3. The peak fast neutron flux ($E > 1$ MeV) was determined from copper wire flux monitors to be about 2.0 ± 0.1 × 10^{18} $n \cdot m^{-2} \cdot s^{-1}$.

TABLE 1—*Average temperatures (K) in each tier for each irradiation phase in the Trillium 2 and Trillium 3 irradiation inserts.*

(a) Trillium 2

No. of cycles	Tier Phase	7	6	5	4	3	2	1
3	1	550	561	534	555	546	558	568
5	2	550	565	538	557	547	561	567
6	3	550	564	539	559	557	561	564
9	4	550	563	538	558	566	561	563
10	5	541	560	540	555	558	540	560
9	6	542	562	540	583	556	542	560
4	7	543	555	539	581	558	541	561
46	Average	546	562	539	555	557	551	562

(b) Trillium 3

No. of Cycles	Tier Phase	7	6	5	4	3	2	1
3	1	583	578	582	581	578	562	584
5	2	584	578	583	592	579	563	586
9	3	588	581	585	588	581	559	590
9	4	586	582	585	585	582	561	590
7	5	587	581	585	584	578	558	590
33	Average	586	581	584	585	580	560	589

Fast neutron fluences of 1.7×10^{26} and 1.3×10^{26} n·m^{-2} have been reached in Trillium 2 and Trillium 3, respectively.

The test specimens are small coupons 38.1 mm long by 6.4 mm wide by either 1.5 mm or 2.5 mm thick fabricated from Zr-2.5Nb pressure tube materials. The specimens were stress-relieved for 6 or 30 h at 673 K depending upon whether the tube had already received the standard 24 h at 673 K used in production (such that each specimen was heated for a total of 30 h at 673 K). The different thicknesses were used in an attempt to balance the nuclear heating and give a more uniform temperature distribution. The specimens were machined with their long (measured) dimension either in the longitudinal or transverse directions of the tubes. The test materials were from Zr-2.5Nb pressure tubes that represent a range of production history with an emphasis on variations in the iron concentration; the tubes are listed in Table 2.

Five specimens irradiated in Trillium 2 (553 K) were made from previously irradiated materials to get an early assessment of high-fluence effects. In one case (Material H), two specimens were manufactured from larger specimens previously irradiated to a fluence of $\sim 1 \times 10^{26}$ n·m^{-2}, in DIDO [5] at 553 K, corresponding to a fluence of 7.5×10^{25} n·m^{-2} in Osiris [2]. In the other case (Material I) the specimens were manufactured from a section of a pressure tube removed from service from Bruce Unit 1 after a fluence of 7.4×10^{25} n·m^2 [5] at an estimated temperature of 550 K. These specimens achieved total fluences of 2.0 and 2.3×10^{26} n·m^{-2}, respectively.

The specimens were measured in a hot cell at a temperature of about 298 K using a computer-controlled comparator with two linearly variable differential transformers. An unirradiated standard specimen was measured frequently during each measurement campaign, with the measurements on the irradiated specimens being repeated if a measurement on the

TABLE 2—*Resolved basal pole fractions, dislocation densities, and Fe concentrations for Zr-2.5Nb tube materials used in this study.*

Material	Tube Type	Resolved Basal Pole Fractions			Dislocation Density $m^{-2} \times 10^{14}$		Fe Concentration[a]
		f_R	f_T	f_L	a	c	
A	Darlington	0.34	0.63	0.04	2.2	0 5	660[b]
B	Pt. Lepreau	0.32	0.59	0.09	3.2	1.1	465
C	Pickering A	0.31	0.61	0.08	3.8	1.1	1000
D1	Pickering B	0.34	0.62	0.04	2.6	0.6	470
D2	Pickering B	0.31	0.65	0.04	2 6	0.7	380
E1	Bruce B	0.34	0.62	0.04	2.6	0.6	660[b]
E2	Pickering B	0.33	0.63	0.04	2.4	0 6	1090
F1	Pickering B	0.29	0.65	0.06	2.5	0.7	470
F2	Pickering B	0.37	0.58	0.05	2.5	0 6	680
H	Bruce B (619)	0.32	0.65	0.04	2.1	0.5	460
I	Bruce A (B2P12)	0.30	0 66	0.04	3.7	0.7	404[c]
	Standard CANDU pressure tubes	0.32	0.62	0.06	3.0 ± 0.5	0.6 ± 0.2	

[a] From chemical analysis from an adjacent area of the tube.
[b] In all cases except E1 this agreed reasonably well with the ingot analysis reported previously [2]. In the case of E2 ingot analysis on each side of the material from which the tube was manufactured were 1060 and 762 ppm.
[c] Value from ingot analysis.

standard deviated from the expected value. The error in the measured lengths is estimated (95% confidence level) as ±0.5 μm, corresponding to an error in strain of $\pm 1.3 \times 10^{-4}$.

Microstructure

Because the irradiation growth specimens are still under test in Osiris, the microstructural analyses reported here were performed on pressure tubing removed from service in CANDU reactors after fast neutron fluences up to 1.1×10^{26} n·m^{-2}. The results of these analyses are deemed relevant to specimens irradiated in Osiris because other work [6] has shown that there is little difference between the dislocation structures that evolve in Osiris compared with those that evolve in the power reactors.

X-ray diffraction (XRD) specimens that were about 100 mm^2 in area by 0.5 mm thick were prepared by cutting splices out of ex-service pressure tubing with normals corresponding to each of the three principal tube axes, i.e., perpendicular to the radial (R), longitudinal (L) and transverse (T) directions of the tubes. Each specimen was then chemically polished using a solution of 5% HF, 45% HNO_3 and 50% H_2O to remove at least 0.025 mm—the depth of damage from the low-speed diamond wheel used to cut the specimen. Dislocation densities and lattice parameters were determined from line-broadening analysis of X-ray diffraction peaks obtained using a Rigaku diffractometer with a 12-kW (rotating anode) generator with Ni-filtered, CuK_α radiation and, for high diffraction angles, a Siemens diffractometer and a 1-kW X-ray generator with Ni-filtered, CuK_α radiation. Measurements on the broadening of the $(30\bar{3}0)$ and prism-plane diffraction lines of the hcp α-phase gives information about a-component dislocation densities and measurements of the broadening of the (0004) basal-plane diffraction lines gives information about c-component dislocation densities [3,7].

Transmission electron microscopy (TEM) specimens were prepared by punching 3-mm-diameter disks out of 0.1-mm-thick slices whose surfaces were perpendicular to the longitudinal direction of the tube. Foils were then made by electropolishing with a solution of 10% perchloric acid in methanol at about −40°C with a current density of about 0.01 A mm^{-2} using a Materials Science Northwest twin-jet apparatus. TEM analysis was performed using a Phillips CM 30 (300-kV) electron microscope. Microchemical analyses were obtained by energy dispersive X-ray analysis (EDXA) using a Link ISIS analyzer system and super atmospheric thin window (SATW) detector. The spatial resolution for microchemical analysis was about 5 to 8 nm.

Results

Irradiation Growth

The growth strains are shown as a function of fluence for the transverse and longitudinal specimens of the three principal sets of test materials, A, B and C, in Figs. 1–3. The growth strains in the longitudinal direction for six materials (D, E, F) with varying Fe concentration are shown in Fig. 4. The growth strains for the preirradiated materials (H, I) are shown in Fig. 5. Note that the fluence scale for the previous irradiation in DIDO of Material H has been adjusted to equivalent fluence in Osiris [*2,3*], and that the growth strain origins for the specimens from the removed pressure tube (Material I) have been shifted to superimpose the results with those from Material H.

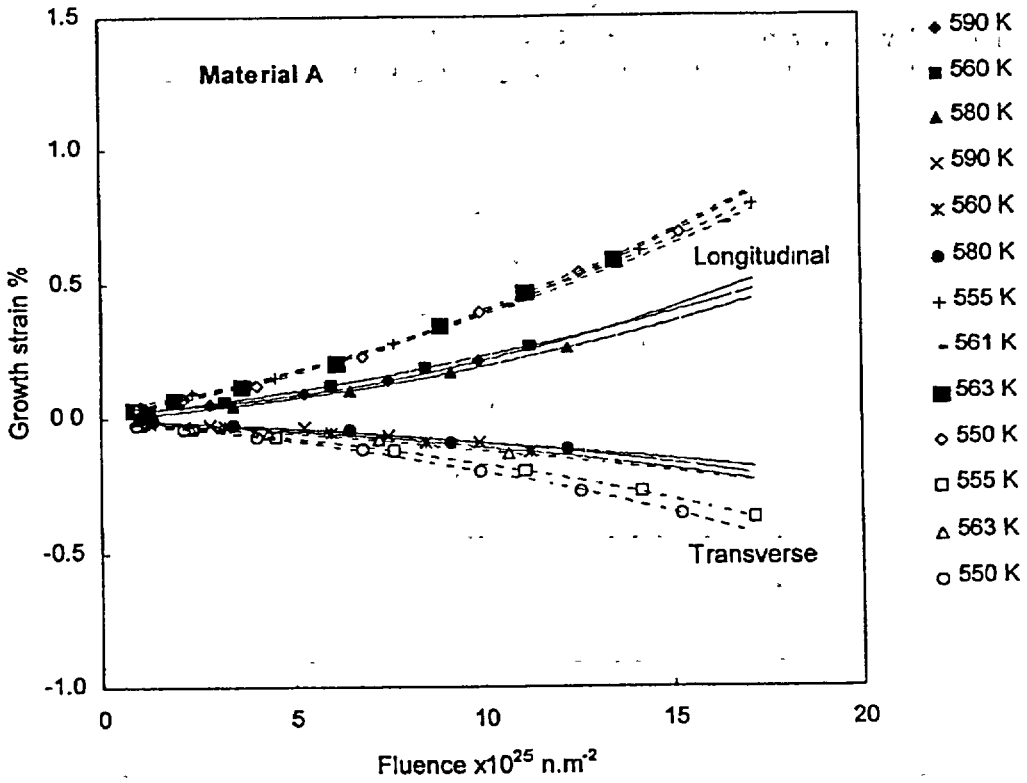

FIG. 1—*Irradiation growth behavior of longitudinal and transverse specimens of Material A irradiated in Trillium 2 and 3 in Osiris*

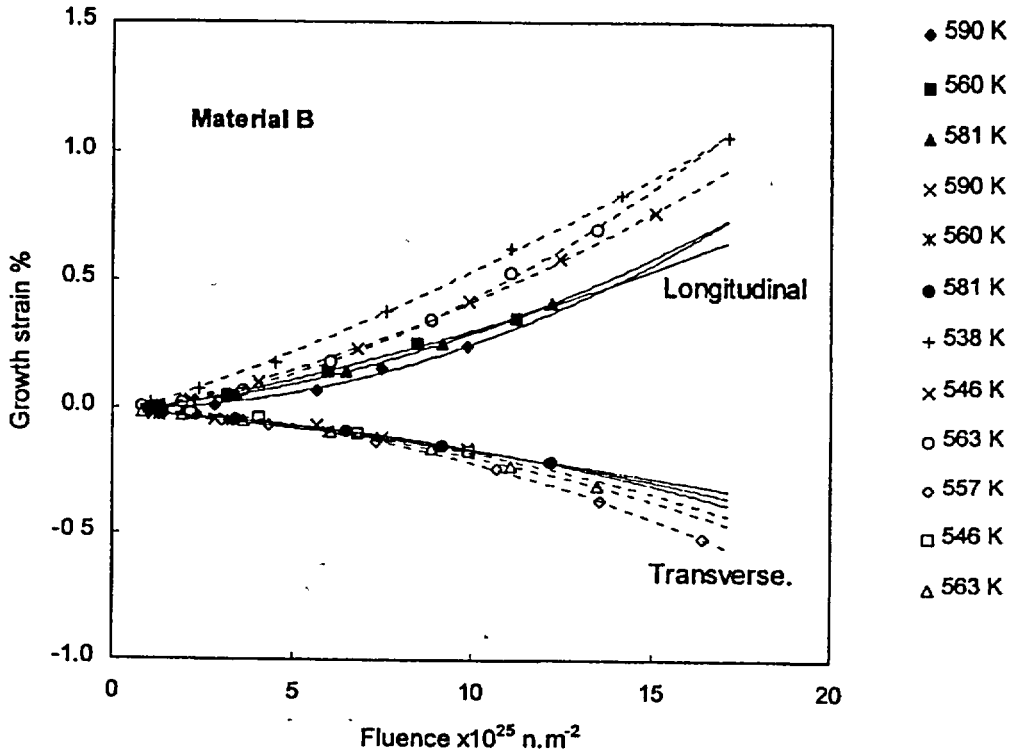

FIG. 2—*Irradiation growth behavior of longitudinal and transverse specimens of Material B irradiated in Trillium 2 and 3 in Osiris.*

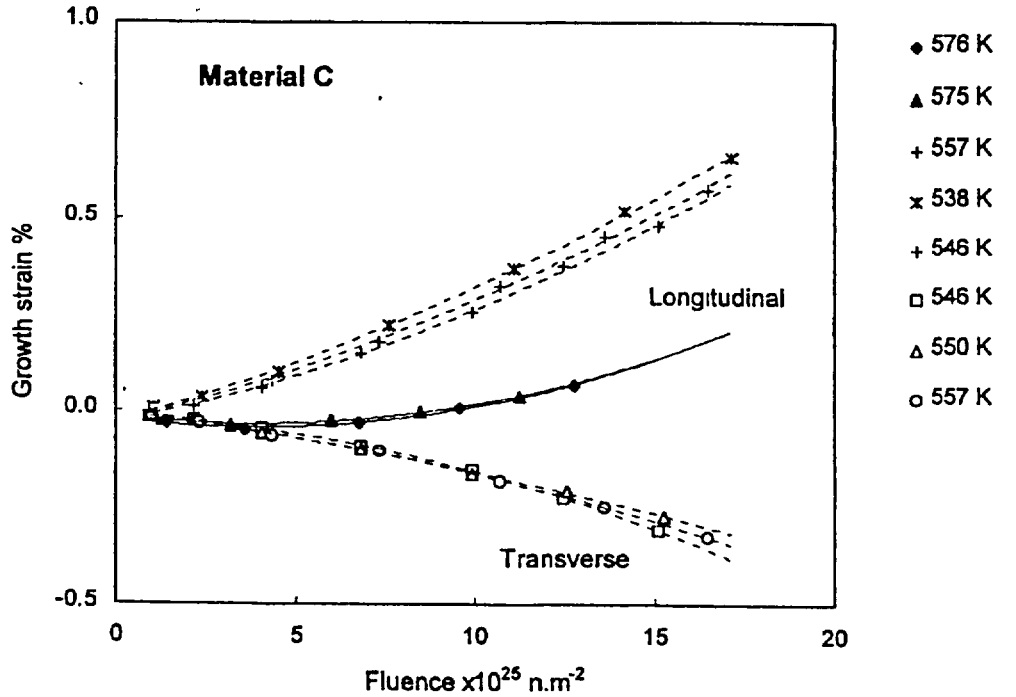

FIG. 3—*Irradiation growth behavior of longitudinal and transverse specimens of Material C irradiated in Trillium 2 and 3 in Osiris.*

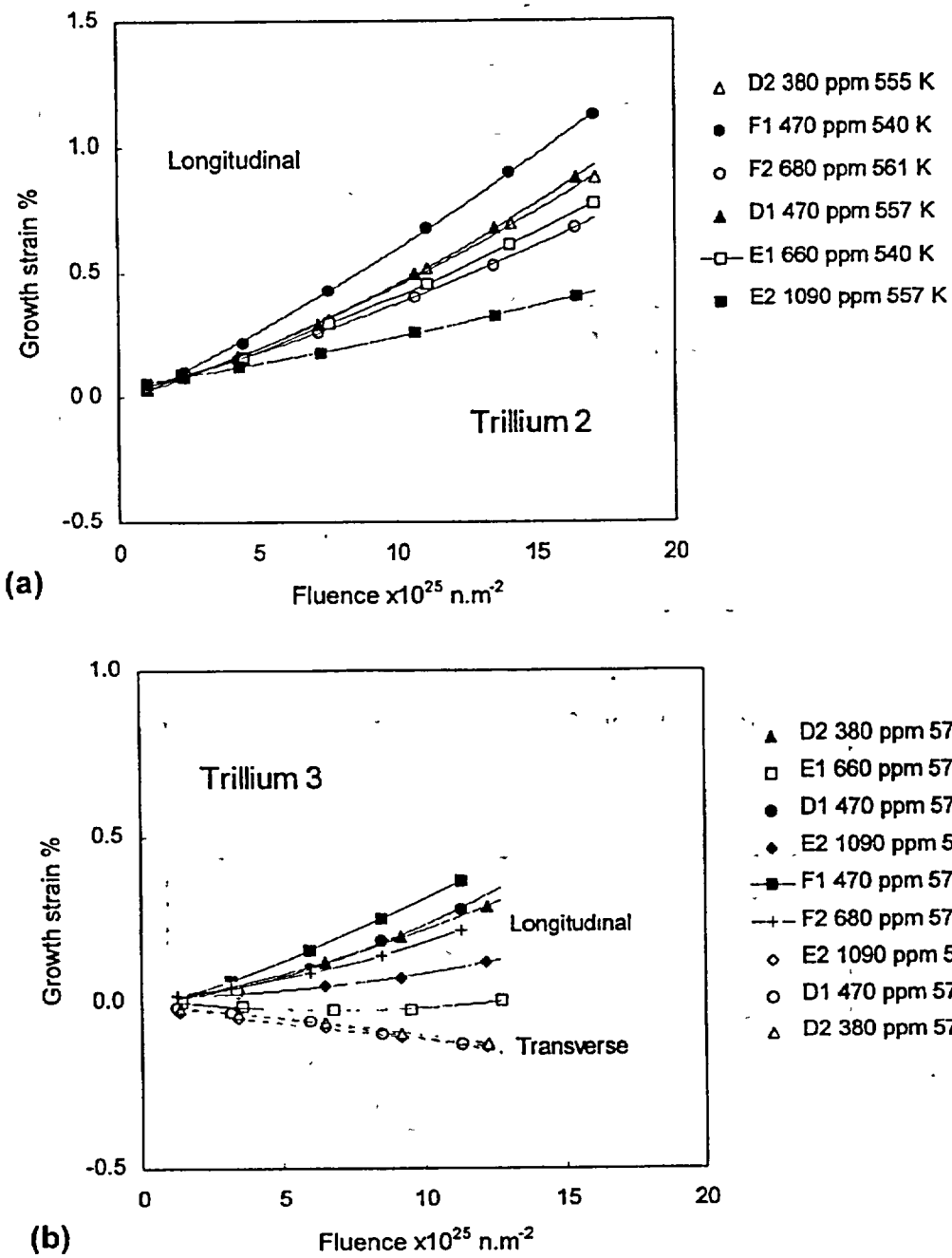

FIG. 4—*Irradiation growth behavior of longitudinal and transverse (dashed lines) specimens of Material D, E, and F irradiated in* (a) *Trillium 2 and* (b) *Trillium 3 in Osiris.*

The important trends seen in these data are:

- The ratio of transverse to longitudinal growth, the growth anisotropy, is of the order of −0.5, independent of fluence, above about 1×10^{25} n·m^{-2}.
- The growth rate is not constant; its magnitude increases with fluence, growth curves

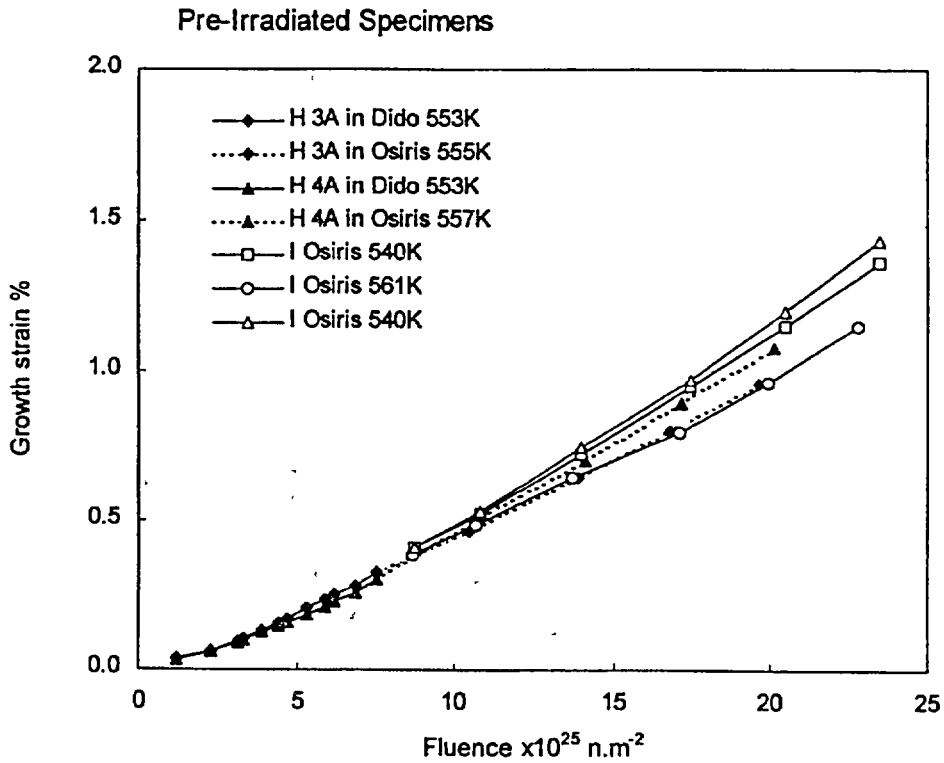

FIG. 5—*Irradiation growth behavior of longitudinal specimens of Material H preirradiated in DIDO and Material I preirradiated in Bruce unit 2 before irradiation in Trillium 2 in Osiris.*

for longitudinal specimens being concave upwards and those for transverse specimens being concave downwards.

- The preirradiated specimens showed some evidence of continued curvature to a fluence of 2.3×10^{26} n·m^{-2}, but there was no sign of any new or sudden transition in the long-term behavior.
- The magnitude of the growth strain (both longitudinal and transverse) decreases with increasing temperature and specimen-to-specimen variability (Materials B and C, for example) corresponds partly to temperature variations within each insert.
- The magnitudes of the growth strains generally decrease with increasing Fe concentration.

Microstructure

Irradiation resulted in the formation of a high density of a-type dislocation loops, i.e., dislocation loops having Burgers vectors of 1/3 $\langle 11\bar{2}0 \rangle$, Fig. 6. In general, the a-type dislocation density increases rapidly at low fluences ($<1 \times 10^{25}$ n·m^{-2}), and there is little further change in the a-type dislocation structure detectable by either TEM or XRD analysis. The c-component dislocation structure, however, evolves at a slower rate, over longer periods of the irradiation and occurs mostly by climb of existing network dislocations with little apparent change in the dislocation structure, Fig. 7. The development of the a- and c-type dislocation structure for grains corresponding with the peak texture is illustrated by the plots

FIG. 6—*Micrographs showing a-type dislocation structure in Zr-2.5Nb pressure tubing:* (a) *before irradiation;* (b) *after irradiation to a fluence of* 1.1×10^{26} $n \cdot m^{-2}$ *at 543 K.*

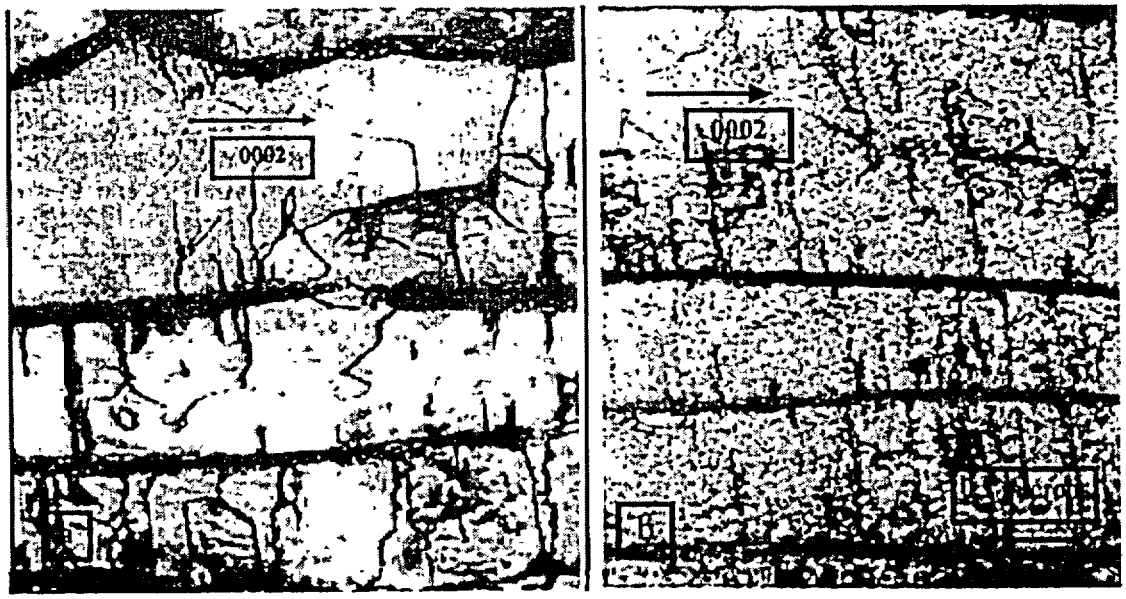

FIG. 7—*Micrograph showing c-component dislocation structure in Zr-2.5Nb pressure tubing for grains with their c-axes in the transverse direction:* (a) *before irradiation;* (b) *after irradiation to a fluence of* 1.1×10^{26} $n \cdot m^{-2}$ *at 543 K. There is little apparent change in the dislocation structure with irradiation.*

of prism- and basal-plane line-broadening, respectively, as a function of fluence and for two temperature ranges in Fig. 8.

The plots show that the a-component dislocation structure evolves very rapidly in the early stages of irradiation and reaches a steady-state (saturated) condition by a fluence of about 1×10^{25} n·m^{-2}. The c-type dislocation structure evolves over a longer period and, apart from an initial line-sharpening that is attributed to splitting of the network dislocations [*7,9*], the c-component dislocation density for grains oriented with their basal poles in the transverse direction changes very little up to high fluences. Although the a-component dislocation density exhibits a marked temperature dependence, there is little evidence for a temperature effect on the c-component dislocations in the grains measured here.

The change in c-component dislocation structure is most apparent in TEM when examining those α-grains having their c-axes oriented towards the radial direction, Fig. 9. There is a small but discernible corresponding increase in basal line-broadening with increasing fluence from the onset of irradiation, Fig. 10.

The increased line-broadening in the radial c-axis grains is associated with climb of existing c-component dislocations of screw character [*8,9*]. The tendency for increased line-broadening for grains with their c-axis oriented towards the radial direction appears to be a direct consequence of the preferred nucleation of c-component dislocation loops on existing screw dislocations—screw dislocations being more prevalent in these grains. The formation of basal plane dislocation loops in grains with their c-axis oriented towards the radial direction will be more energetically favorable in a pressurized tube provided these c-component defects are vacancy in nature, which is normally the case [*1,8*].

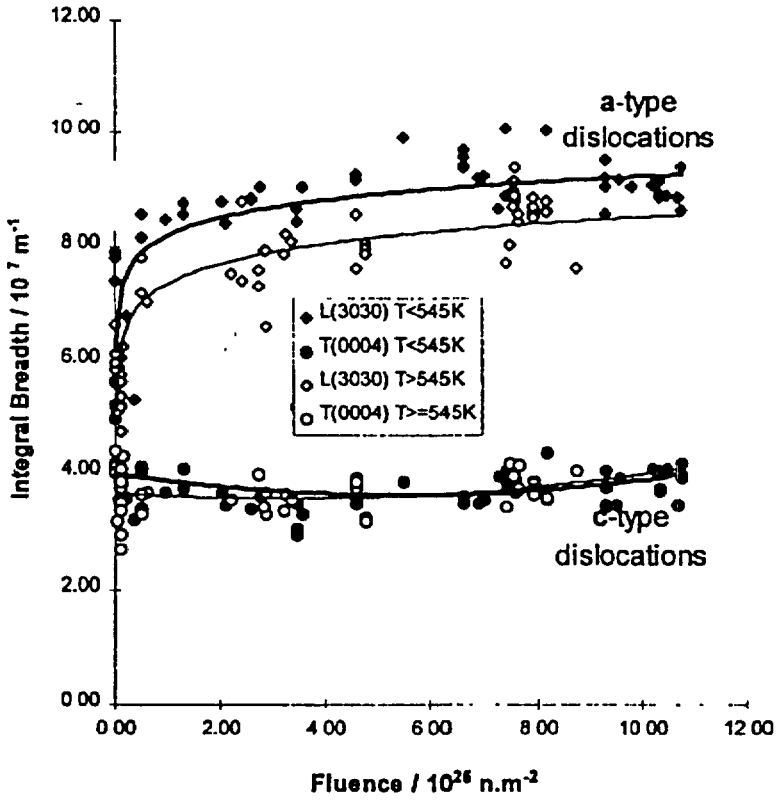

FIG. 8—*Variation in a-type and c-type dislocation density (measured as an integral breadth) for Zr-2.5Nb pressure tubing as a function of fluence in CANDU reactors.*

FIG 9—*Micrograph showing c-component dislocation structure in Zr-2.5Nb pressure tubing for grains with their c-axes in the radial direction:* (a) *before irradiation:* (b) *after irradiation to a fluence of 1.1 × 10²⁶ n · m⁻² at 543 K. Basal plane dislocation loops (arrowed) nucleate and grow on existing screw dislocations.*

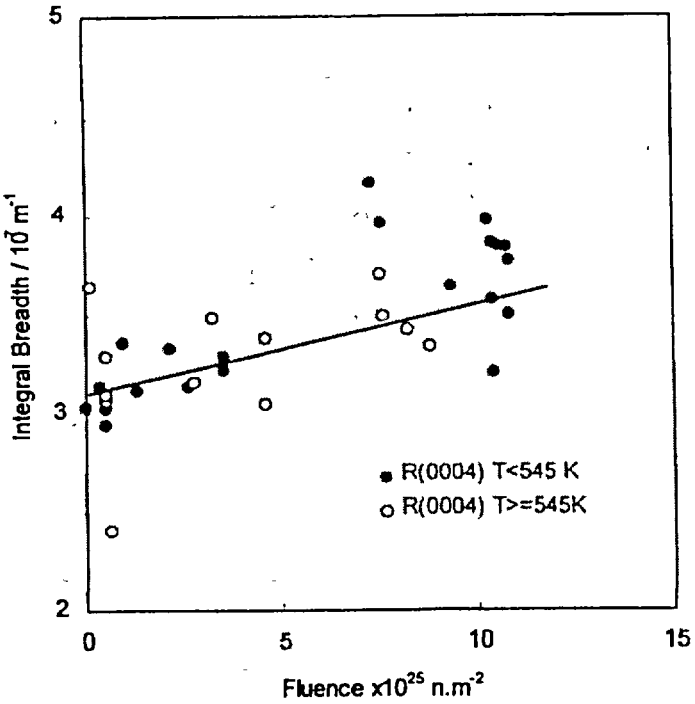

FIG. 10—*Comparison of basal line-broadening as a function of fluence for Zr-2.5Nb pressure tubes irradiated in CANDU reactors at 520 to 570 K.*

Discussion

Fluence Dependence of Growth

By inspection it is clear that all the longitudinal growth curves for the nonpreirradiated specimens exhibit some upward curvature while all the transverse growth curves exhibit downward curvature. The curvature was evaluated by fitting quadratics ($\varepsilon = a + b\Phi + c\Phi^2$, where Φ is the fast fluence, and ε the growth strain) to the data for each specimen. The quadratics give good fits to the data as shown in Figs. 1 through 4. Averaged over all the longitudinal and transverse growth curves, the quadratic term, c, is positive and negative, respectively, with a high degree of significance ($1.14 \pm 0.19 \times 10^{-55}$ m$^4 \cdot$n^{-2} and $-0.63 \pm 0.21 \times 10^{-55}$ m$^4 \cdot$n^{-2}).

It is well established [*9,10*] that the growth rate of zirconium alloys is strongly influenced by the density of c-component dislocations. The gradual increase in the absolute growth rate with time, in Zircaloy-2, was attributed to the gradual increase in the c-component dislocation density with fast fluence [*8*]. A similar gradual increase in the c-component dislocation density in the Zr-2.5Nb pressure tube material irradiated in power reactors (Figs. 8 and 10) probably explains the curvature in the growth curves. Whether the growth rate will saturate at a constant level beyond fluences of 1.7×10^{26} n$\cdot$m^{-2}, as eventually expected based on a simple model for Zircaloy-2 [*3*], is not yet clear.

Anisotropy of Growth

The anisotropy of growth in Zr-2.5Nb does not necessarily follow a simple relationship relating to the crystallographic texture, resulting from expansion in the a directions and shrinkage along the c direction (e.g., variations of $\varepsilon_d \propto 1 - 3F_d$ that allow for intergranular constraint [*12*], where ε_d is the growth strain in the "d" direction and F_d is the resolved fraction of prism plane normals in that direction). This lack of adherence to the simple texture relationship can be attributed to the strong role of the grain boundaries as sinks for the radiation-induced point defects, whereby the grain boundary orientations also influence the observed anisotropy [*13*]. Typically, standard pressure tubes exhibit an anisotropy ratio (transverse to axial growth) of about -0.5 in the current work, significantly different from that expected from texture alone, see Table 2.

Because the grain boundaries are an important sink for point defects, a change in the density of sinks within the grains (i.e., the c-component dislocation density) would be expected to change the growth anisotropy. This appears to be the case here because the linear term b of the quadratic (which represents the initial growth rate) exhibits a slightly different anisotropy than the quadratic term (-0.42 vs. -0.54). This difference illustrates a change in the anisotropy with fluence in the direction of that predicted from texture alone. The irradiation growth tensor of individual grains becomes dominated by the dislocation structure and approaches behavior in which the role of grain boundaries is negligible (shrinkage along the c axis balanced by expansion in the basal plane) [*14*].

Dependence of Growth of Temperature and Fe Concentration

To assess the effects of temperature and Fe concentration on growth, the magnitudes of the growth strains and rates at a fast fluence of 1.0×10^{26} n$\cdot$m^{-2} were interpolated using the quadratic equation for each specimen. These are plotted as a function of temperature in Figs. 11 and 12*a* and *b*. The magnitudes of the growth strains and growth rates decrease with temperature for both test directions whether the data are considered collectively or subdivided into groups according to Fe concentration: high (1000 to 1090 ppm), medium

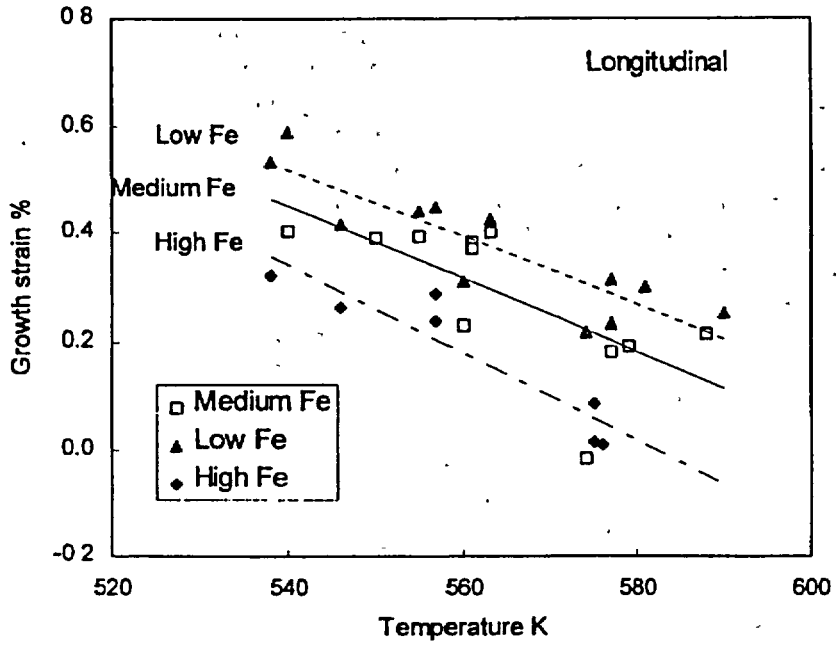

(a)

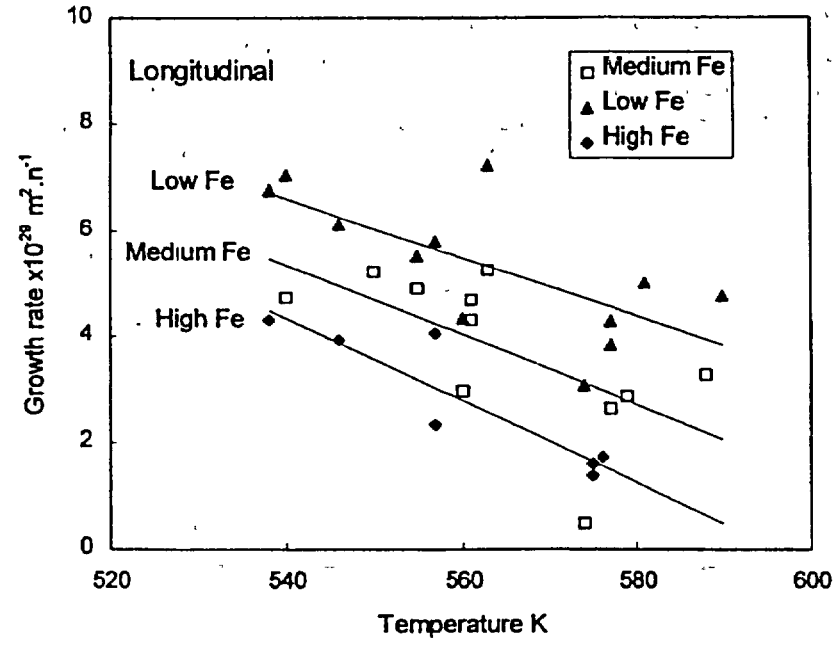

(b)

FIG. 11—*Effect of Fe concentration and temperature on* (a) *the growth strains, and* (b) *the growth rates of longitudinal specimens irradiated in Trillium 2 and 3 in Osiris.*

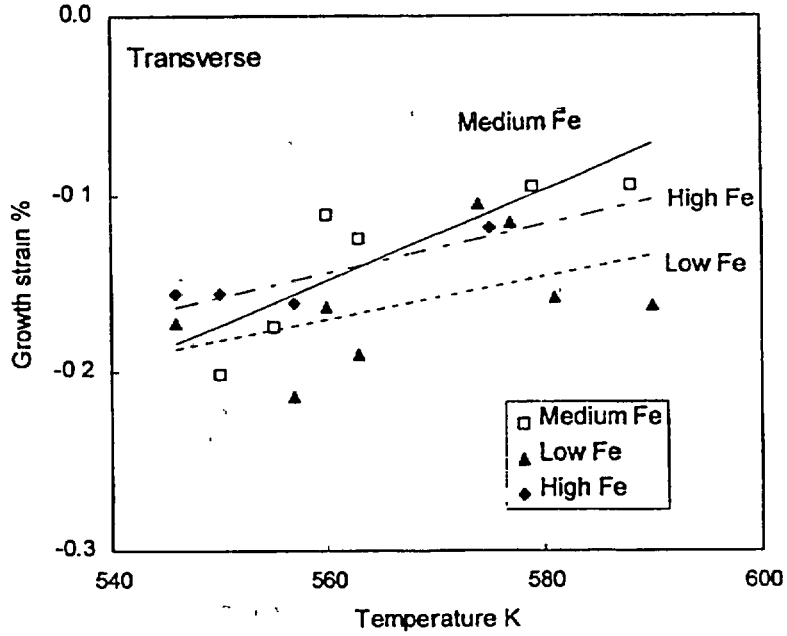

(a)

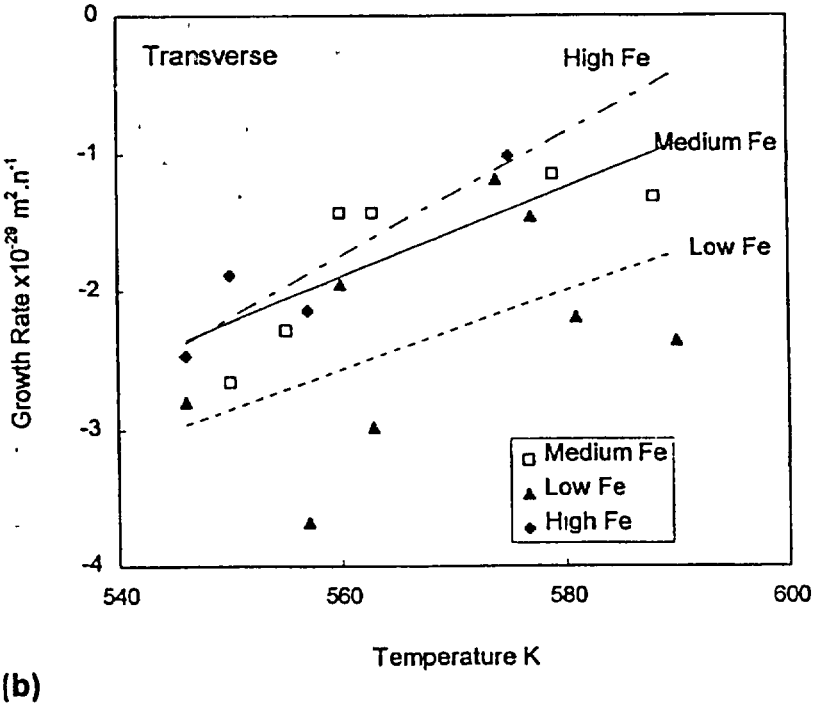

(b)

FIG. 12—*Effect of Fe concentration and temperature on* (a) *the growth strains, and* (b) *the growth rates of transverse specimens irradiated in Trillium 2 and 3 in Osiris.*

(660 to 680 ppm), and low (380 to 470 ppm). The magnitude of the negative temperature coefficient for the transverse direction is approximately half that for the longitudinal direction, indicating that the anisotropy of growth is relatively insensitive to temperature.

The effect of increased Fe concentration in decreasing the magnitude of growth shows up clearly in the longitudinal direction, Fig. 11, where there is a significant difference between the three levels of Fe at the 95% confidence level. It is less clear in the transverse direction, Fig. 12, where the trends appear to be the same, but the differences are not significant at the 95% confidence level.

The linear and quadratic coefficients of the quadratic equations fitted to the longitudinal growth curves are plotted against temperature in Fig. 13. Here it is clear that the temperature dependence is contained mainly in the initial growth rate (b), while the curvature (c) is relatively insensitive to temperature. Note that the initial growth rate (b) can be negative with high Fe concentration at high temperature. The dependence of these two parameters on Fe concentration appears to be similar, although somewhat masked by experimental variation.

These results are consistent with the temperature dependence of the microstructural changes. The temperature dependence of growth derives almost entirely from factors that affect the growth rate in the early stages, e.g., the buildup of the a dislocation density (which is clearly temperature sensitive, and decreases with increasing temperature). The curvature, which is insensitive to temperature is attributed to the build up of the c component dislocation density (also insensitive to temperature).

The effect of Fe could be attributed to several characteristics of Fe in α-Zr: the enhancement of vacancy diffusion [*15*], the modification of the anisotropy of vacancy diffusion [*16*], or the enhanced nucleation of irradiation-induced dislocation loops, especially on the basal planes [*11*]. In the latter case, the rate of increase of growth with fluence should depend on the Fe concentration and should be seen in the c parameter of the equation, but this is clearly not the case. At the temperatures used here, the enhancement of vacancy diffusion should not be a significant factor, because the growth rate is linear in fast flux [*13*] and, therefore, controlled by sink-density rather than diffusion. Therefore, the effect of Fe on growth may stem from its effect on the anisotropy of vacancy migration. This would be expected to modify the early rate and the curvature equally, at least once the Fe was fully redistributed (i.e., after 2 to 3 $\times$ 10^{25} n·m^{-2} [*1*], approximately the fluence of the second data point in the current tests).

Conclusions

1. Irradiation growth specimens produced from cold-worked Zr-2.5Nb pressure tube material have been irradiated in Osiris at a fast flux of ~1.8 $\times$ 10^{18} n·m^{-2}·s^{-1}, $E > 1$ MeV, at nominal temperatures of 553 and 583 K, to growth strains of 1%.

2. Longitudinal specimens (which generally exhibit positive growth strains) and transverse specimens (which generally exhibit negative strains with approximately 50% of the magnitude of the longitudinal strains) show nonlinear growth, the rate increasing gradually with fluence up to 1.3 $\times$ 10^{26} n·m^{-2}, $E > 1$ MeV (580 K) and 1.7 $\times$ 10^{26} n·m^{-2}, $E > 1$ MeV (550 K). Preirradiated specimens showed some evidence of continued curvature to a fluence of 2.3 $\times$ 10^{26} n·m^{-2}, but there is no sign of any further transition in the long-term behavior.

3. The previously reported temperature dependence of the longitudinal growth strains (decreasing with increasing temperature for fluences up to 4 $\times$ 10^{25} n·m^{-2}, $E > 1$ MeV) is maintained to the higher fluences now achieved, as is the effect of Fe (axial growth strains decreasing with increased Fe concentration in the range). The effects of temperature and Fe in the transverse direction are approximately the reverse of those in the longitudinal direction.

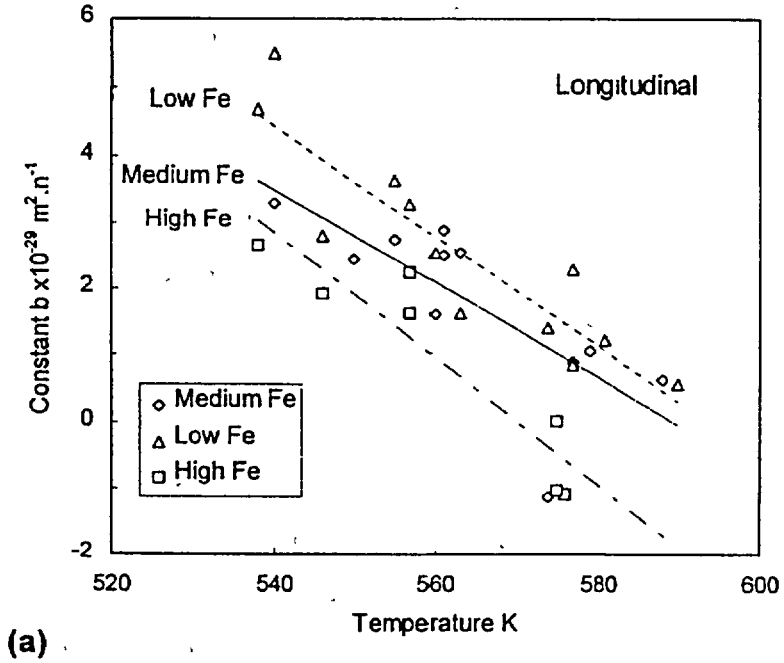

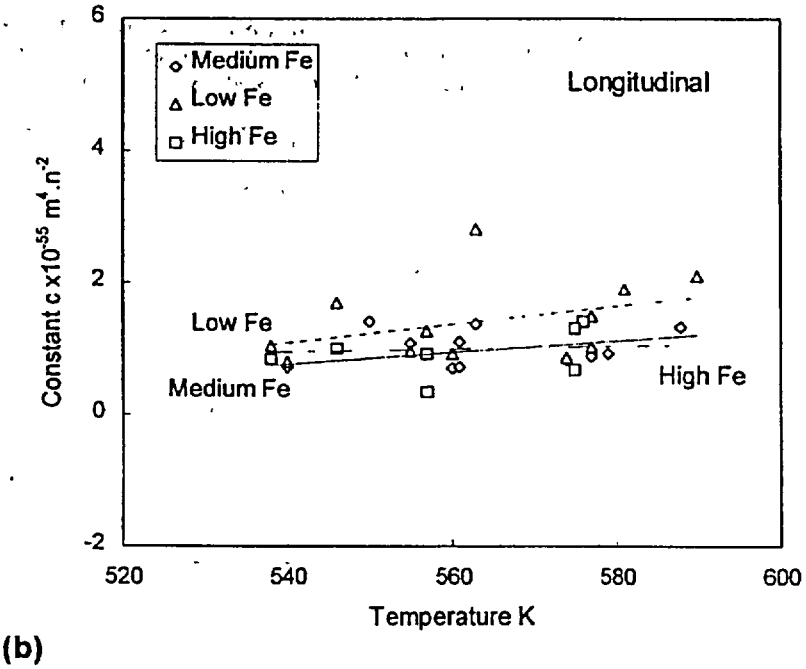

FIG. 13—*Effect of Fe concentration and temperature on the parameters* (a) *b, and* (b) *c of longitudinal specimens irradiated in Trillium 2 and 3 in Osiris.*

4. Examination, by transmission electron microscopy and X-ray diffraction, of Zr-2.5Nb pressure tubes irradiated to 1×10^{26} n·m^{-2}, $E > 1$ MeV, at 520 to 570 K in power reactors, shows that the curvature in the growth curves can be attributed to multiplication of the c-component dislocations with increasing fast fluence while the a-type dislocation density remains constant after about 0.1×10^{26} n·m^{-2}, $E > 1$ MeV.

Acknowledgments

We acknowledge M. A. Miller, A. K. MacCormack, F. J. Butcher, and S. A. Donohue for preparing and measuring the test specimens; J. F. Mecke and J. E. Winegar for the X-ray diffraction data; A. Alberman, F. Koskas, Y. Bouilloux, M. Roche, and M. Farney for irradiating the specimens in Osiris; and the CANDU Owners Group (COG) for funding the work.

References

[1] Griffiths, M., Mecke, J. F., and Winegar, J. E., "Evolution of Microstructure in Zirconium Alloys during Irradiation," *Zirconium in the Nuclear Industry: Eleventh Intrnational Symposium, ASTM STP 1295,* E. R. Bradley and G. P. Sabol, Eds., American Society for Testing and Materials, 1996, pp. 580–602.

[2] Fleck, R. G., Elder, J. E., Causey, A. R., and Holt, R. A., "Variability of Irradiation Growth in Zr-2.5Nb Pressure Tubes," *Zirconium in the Nuclear Industry: Tenth International Symposium, ASTM STP 1245,* A. M. Garde and E. R. Bradley, Eds., American Society for Testing and Materials, 1994, pp. 168–182.

[3] Holt, R. A., Causey, A. R., Christodoulou, N., Griffiths, M., Ho, E. T. C., and Woo, C. H., "Non-Linear Irradiation Growth of Cold-Worked Zircaloy-2," *Zirconium in the Nuclear Industry: Eleventh International Symposium ASTM STP 1295,* E. R. Bradley and G. P. Sabol, Eds., American Society for Testing and Materials, 1996, pp. 623–637.

[4] Christodoulou, N., Causey, A. R., Holt, R. A., Tome, C. N., Badie, N., Klassen, R. J., Sauve, R., and Woo, C. H., "Modeling In-Reactor Deformation of Zr-2.5Nb Pressure Tubes in CANDU Power Reactors," *Zirconium in the Nuclear Industry: Eleventh International Symposium, ASTM STP 1295,* E. R. Bradley and G. P. Sabol, Eds., American Society for Testing and Materials, 1996, pp. 518–537.

[5] Holt, R. A. and Fleck, R. G., "The Contribution of Irradiation Growth to Pressure Tube Deformation," *Zirconium in the Nuclear Industry: Ninth International Symposium, ASTM STP 1132,* C. M. Eucken and A. M. Garde, Eds., American Society for Testing and Materials, 1991, pp. 218–229.

[6] Davies, P. H., Hosbons, R. R., Griffiths, M., and Chow, C. K., "Correlation between Irradiated and Unirradiated Fracture Toughness of Zr-2.5Nb Pressure Tubes," *Zirconium in the Nuclear Industry: Tenth International Symposium, ASTM STP 1245,* A. M. Garde and E. R. Bradley, Eds., American Society for Testing and Materials, 1994, pp. 135–167.

[7] Griffiths, M., Winegar, J. E., Mecke, J. F., and Holt, R. A., "Determination of Dislocation Densities in HCP Metals Using X-Ray Diffraction and Transmission Electron Microscopy," *Advances in X-ray Analysis,* Vol. 35, 1992, p. 593.

[8] Griffiths, M., Holt, R. A., and Rogerson, A., "Microstructural Aspects of Accelerated Deformation of Zircaloy Nuclear Reactor Components During Service," *Journal of Nuclear Materials,* Vol. 225, 1995, p. 245.

[9] Griffiths, M., Styles, R. C., Woo, C. H., Phillipp, F., and Frank, W., "Study of Point Defect Mobilities in Zirconium during Electron Irradiation in a HVEM," *Journal of Nuclear Materials,* Vol. 208, 1994, p. 324.

[10] Holt, R. A. and Gilbert, R. W., "⟨c⟩ Component Dislocations in Annealed Zircaloy Irradiated at about 570 K," *Journal of Nuclear Materials,* Vol. 137, 1986, p. 185.

[11] Griffiths, M., Gilbert, R. W., and Fidleris, V., "Accelerated Irradiation Growth of Zirconium Alloys," *Zirconium in the Nuclear Industry: Eighth International Symposium, ASTM STP 1023,* American Society for Testing and Materials, 1989, p. 658.

[*12*] Causey, A. R., Woo, C. H., and Holt, R. A , "The Effect of Intergranular Stresses on the Texture Dependence of Irradiation Growth in Zirconium Alloys," *Journal of Nuclear Materials,* Vol. 159, 1988, p. 225.

[*13*] Holt, R. A., "Mechanisms of Irradiation Growth of Alpha-Zirconium Alloys," *Journal of Nuclear Materials,* Vol. 159, 1988, p. 310.

[*14*] Tempest, P. A., "Preferred Orientation and Its Effect on Bulk Physical Properties of Hexagonal Polycrystalline Materials," *Journal of Nuclear Materials,* Vol. 92, 1980, p. 191.

[*15*] King, A. D., Hood, G. M., and Holt, R. A., "Fe-Enhancement of Self-Diffusion in α-Zr," *Journal of Nuclear Materials,* Vol. 185, 1991, p. 174.

[*16*] Hood, G. M., Zou, H., Gupta, D., and Schultz, R. J., "α-Zr Self-Diffusion Anisotropy," Atomic Energy of Canada Ltd. Report AECL-11186, 1994.

DISCUSSION

B. Cox[1] (*written discussion*)—Was there any difference in the Fe distribution in the low and high Fe material? Did it all start dissolved in the β-Zr or did the high Fe material exceed the solubility in this phase?

R. A. Holt et al. (*authors' closure*)—There was no difference in the Fe distribution between the low and high Fe materials. Before irradiation the Fe was concentrated in the β-phase and no other Fe-rich particles were observed. After irradiation the Fe was more or less uniformly dispersed.

A. T. Motta[2] (*written discussion*)—Your hypothesis is that ⟨a⟩ loop density is lower at higher temperature leading to a lower growth strain. Can you comment on how this lower density of ⟨a⟩ loops comes about? The amount of Fe in both the high and low Fe samples is much beyond the solubility limit. Can you comment on the microstructural basis for the reduction in growth strain with increasing Fe content?

R. A. Holt et al. (*authors' closure*)— Presumably the lower dislocation density at the higher temperatures coincides with an increase in the degree of thermal annealing during irradiation. After irradiation to $1 - 3 \times 10^{25}$ n·m^{-2} ($E > 1$ MeV) the Fe is more or less uniformly dispersed. It is not clear whether it is in solution in the α-phase or in some submicroscopic particulate form. In the former case the effect of Fe could be related to its effect on vacancy properties, particularly the anisotropy of vacancy migration. In the latter case the particles could act as recombination sites, reducing the availability of point defects to other sinks.

[1] University of Toronto, Toronto, Ont., Canada.
[2] Penn State University, University Park, PA.

A. R. Causey,[1] *R. A. Holt,*[2] *N. Christodoulou,*[1] *and E. T. C. Ho*[3]

Irradiation-Enhanced Deformation of Zr-2.5Nb Tubes at High Neutron Fluences

REFERENCE: Causey, A. R., Holt, R. A., Christodoulou, N., and Ho, E. T. C., **"Irradiation-Enhanced Deformation of Zr-2.5Nb Tubes at High Neutron Fluences,"** *Zirconium in the Nuclear Industry, Twelfth International Symposium, ASTM STP 1354*, G. P. Sabol and G. D. Moan, Eds., American Society for Testing and Materials, West Conshohocken, PA, 2000, pp. 74–85

ABSTRACT: The effects of neutron flux and temperature on irradiation creep of 10-mm-diameter Zr-2.5Nb tubes are being assessed in end-of-life experiments in the Osiris reactor in France. The tubes have crystallographic texture, grain shape, and dislocation densities that are similar to those of full-size CANDU reactor pressure tubes. The experiments are performed at nominal operating temperatures of 553 and 583 K in fast neutron fluxes up to 2.0×10^{18} $n \cdot m^{-2} \cdot s^{-1}$ ($E_n > 1$ MeV). Transverse and axial strains are reported as functions of fluence for specimens internally pressurized to hoop stresses from 0 to 160 MPa and irradiated to fluences up to 1.5×10^{26} and 1.3×10^{26} $n \cdot m^{-2}$ at 553 and 583 K, respectively. The measured transverse and axial strain rates in these high-fluence experiments are shown to be in good agreement with a creep model relating crystallographic texture to the in-reactor deformation of CANDU pressure tubes. The anisotropy of irradiation creep does not change with fluence, but the temperature dependencies of creep and growth are changing; the activation temperature for creep is increasing, while the magnitude of the activation temperature for irradiation growth (a negative value) is becoming less negative with fluence.

KEYWORDS: zirconium alloys, nuclear industry, creep (materials), texture (materials), tubes, nuclear materials, radiation effects

Cold-worked Zr-2.5Nb pressure tubes in CANDU reactors undergo an increase in diameter and length and horizontal deflection due to thermal creep, irradiation-induced creep, and irradiation growth. The creep strains have been previously shown to be significantly affected by the extrusion and cold-working processes used to fabricate the tubes [*1–4*]. The microstructural features that control the creep behavior are primarily the crystallographic texture, grain shape, and dislocation density. The effects of neutron flux and temperature on irradiation creep of Zr-2.5Nb tubes are being assessed in end-of-life experiments carried out in the Osiris reactor in France. The experimental results obtained from these tests are the only means of assessing the anisotropy of in-reactor creep and its variation with fluence to the projected end-of-life. The creep anisotropy derived from these tests will provide the data that are used in the model to correctly take account of axial and diametral creep strains in the measured deformations of pressure tubes during service in power reactors. It should also be noted that, since the creep equation for pressure tube sag is obtained directly from the

[1] Senior researcher and [2]division director, AECL, Chalk River Laboratories, Chalk River, Ontario K0J 1J0, Canada.
[3] Senior researcher, Ontario Hydro, Kipling Laboratories, Toronto, Ontario, Canada.

creep model (and not from measurements), the correct anisotropy model is vital to the predictions of pressure tube/calandria tube contact. Therefore, the results presented here are used for the quantification of the effects of stress, fluence, and temperature on the irradiation creep component of the deformation of Zr-2.5Nb pressure tubes in CANDU reactors. This report is an update of the end-of-life biaxial creep tests on small Zr-2.5Nb tubes first reported in 1994 [5] with total fast neuron fluences now approached 15×10^{25} n·m^{-2} ($E > 1$ MeV), i.e., three to four times those in the first report.

Experimental

Test Materials and Specimens

The specimens are internally pressurized capsules fabricated from small Zr-2.5Nb tubing made by the same process as the power reactor pressure tubes. The fabrication procedures and resulting microstructures in the specimens are described in detail in Ref *5*. The crystallographic textures and dislocation densities, determined by X-ray diffraction, are summarized in Table 1. The measured resolved fractions of basal plane normals in the three principal directions and a and c component-type dislocation densities, estimated from broadening of the prism and basal X-ray diffraction peaks, are within the range typical of standard CANDU reactor pressure tubes.

The creep capsules have a gage length of 46.4 mm, outside diameter of 10.0 mm, and a wall thickness of 0.45 mm. End-caps, machined from Zr-2.5Nb rods, were electron-beam welded to the tubes, and the specimens were heated for a total of 48 h at 673 K to relieve residual stresses near the welds. The capsules were pressurized using high-purity helium gas and sealed by tungsten inert gas welding. The operating hoop stresses for each tube were calculated from the internal pressure at room temperature assuming that the helium behaves as an ideal gas. The capsules were pressurized to give hoop stresses at the nominal test temperatures in the range 0 to 170 MPa (Table 2).

Test Procedure

The specimens were measured underwater in the reactor pool at a nominal temperature of 313 K. Six diameter readings were made at positions along the capsules with a computer-controlled comparator using linear variable differential transformers. The diameter values were taken from an average of the middle three of six readings, each being an average of 200 measurements made around the perimeter. The length was measured from end-cap to end-cap of the specimens with the comparator and the reading obtained by averaging 200 measurements made around the perimeter. A standard specimen was measured before and after each of three repeat measurements on the irradiated specimen and the readings nor-

TABLE 1—*Dislocation densities and resolved basal pole fractions for Zr-2.5Nb tube materials.*

Material	Dislocation Density, $m^{-2} \times 10^{14}$		Resolved Basal Pole Fractions		
	⟨a⟩	⟨c⟩	f_R	f_T	f_L
Small Tube M2	4.0	0.5	0.33	0 61	0 06
CANDU pressure tubes	3.0 ± 0.5	0 6 ± 0.2	0.32	0 62	0.06

TABLE 2—*Reactor specimens loaded for the Trillium 2 and Trillium 3 irradiation phases listing specimen identity, hoop stress (MPa) at average test temperature, and time-averaged temperature (K) during each phase.*

Capsule	Stress, MPa	Temperature K				
		Phase 1	Phase 2	Phase 3	Phase 4	Phase 5
			TRILLIUM 2			
M03	0	540	540	541	541	538
M13	39	564	562	563	564	558
M14	78	553	563	553	552	555
M17	156	559	558	555	553	551
M18	118	561	564	559	557	554
			TRILLIUM 3			
M04	0	584	585	593	594	597
M01	40	584	578	584	584	585
M16	81	589	586	597	596	596
M15	119	585	583	585	585	584
M02	160	579	578	588	585	581

malized to 313 K to account for variations in the bay temperatures. The error in the measured diameters and lengths was estimated (95% confidence level) as ± 2 and ± 5 μm, respectively. In terms of strains, the errors are $\pm 2 \times 10^{-4}$ in diameter and $\pm 1 \times 10^{-4}$ in length.

The irradiations are performed in NaK-filled stainless steel inserts, which are described in more detail in Ref 6. The temperatures were controlled with heaters surrounding the insert, and the nominal operating temperatures were 553 K in Trillium 2 and 583 K in Trillium 3. The peak fast neutron flux ($E > 1$ MeV) was determined from copper wire flux monitors to be about $2.0 \pm 0.1 \times 10^{18}$ n·m^{-2}·s^{-1}. Fast neutron fluences approaching 15×10^{25} and 13×10^{25} n·m^{-2} were reached in Trillium 2 and Trillium 3, respectively.

The specimen stresses and loadings for each of the irradiation phases in Trillium 2 and Trillium 3 are given in Table 2. Each insert contained five specimens, each fabricated from Tube M2. The temperatures were measured and controlled with thermocouples in contact with the creep specimens. The time average temperatures of each specimen during each irradiation phase are listed in Table 2.

Results

The measured transverse and axial strains are plotted as functions of neutron fluence for the Trillium 2 and Trillium 3 in Figs. 1 and 2. The temperatures in the Trillium 2 and Trillium 3 experiments varied somewhat during the first two irradiation phases and became fairly steady for the last three phases. In this analysis we are considering only the data from the last three phases. The linear strain rates per unit fluence over the last three phases in the Trillium 2 and Trillium 3 experiments are plotted against hoop stress in Fig. 3. The range of fluence is similar, 5 to 15×10^{25} n·m^{-2} for Trillium 2 and 3 to 13×10^{25} n/m^{-2} for Trillium 3. The slopes of the strain rate versus stress plots give the creep compliances for listed in Table 3.

Analysis and Discussion

The complex interaction between the effects of temperature and fast neutron flux on the deformation of zirconium alloys has led to the development of analyses that assume that

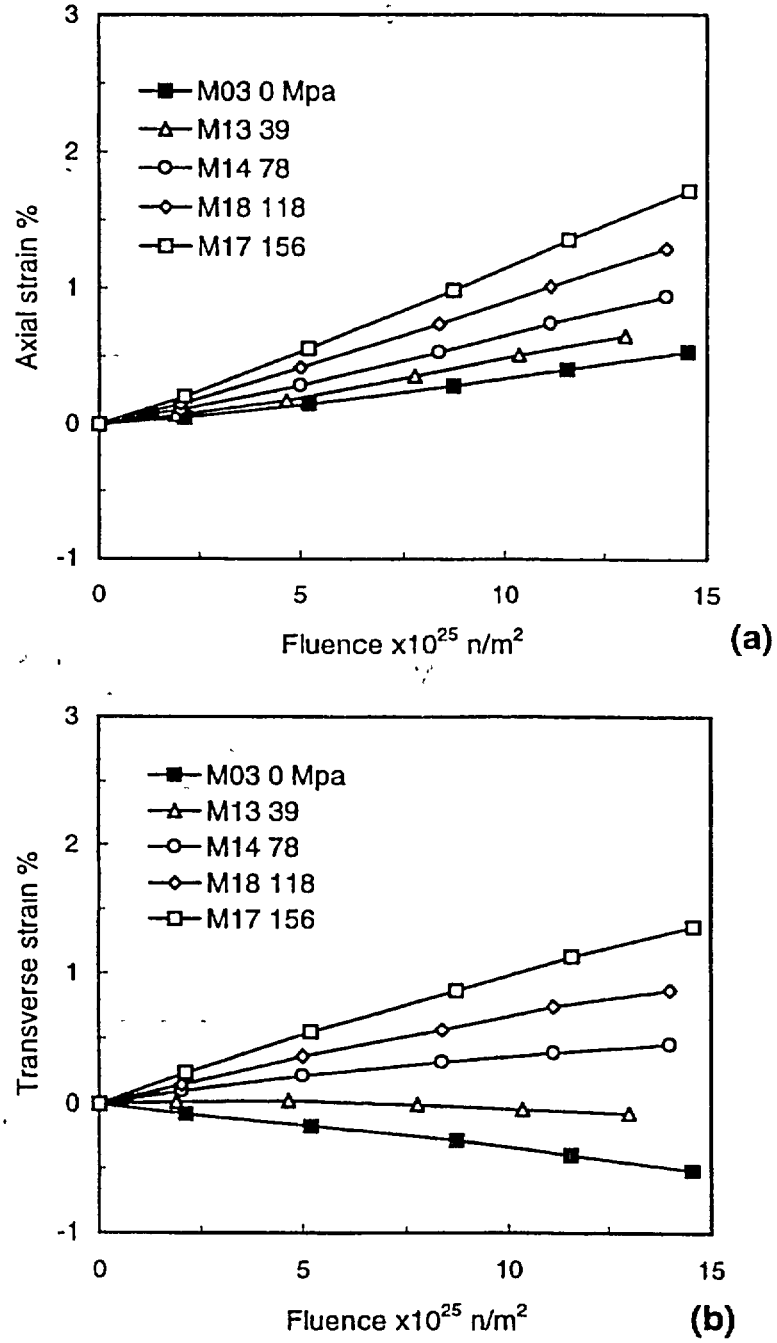

FIG. 1—*Creep strain as a function of neutron fluence for specimens from Small Tube M2 irradiated in Trillium 2 at a nominal temperature of 553 K:* (a) *axial strain,* (b) *transverse strain.*

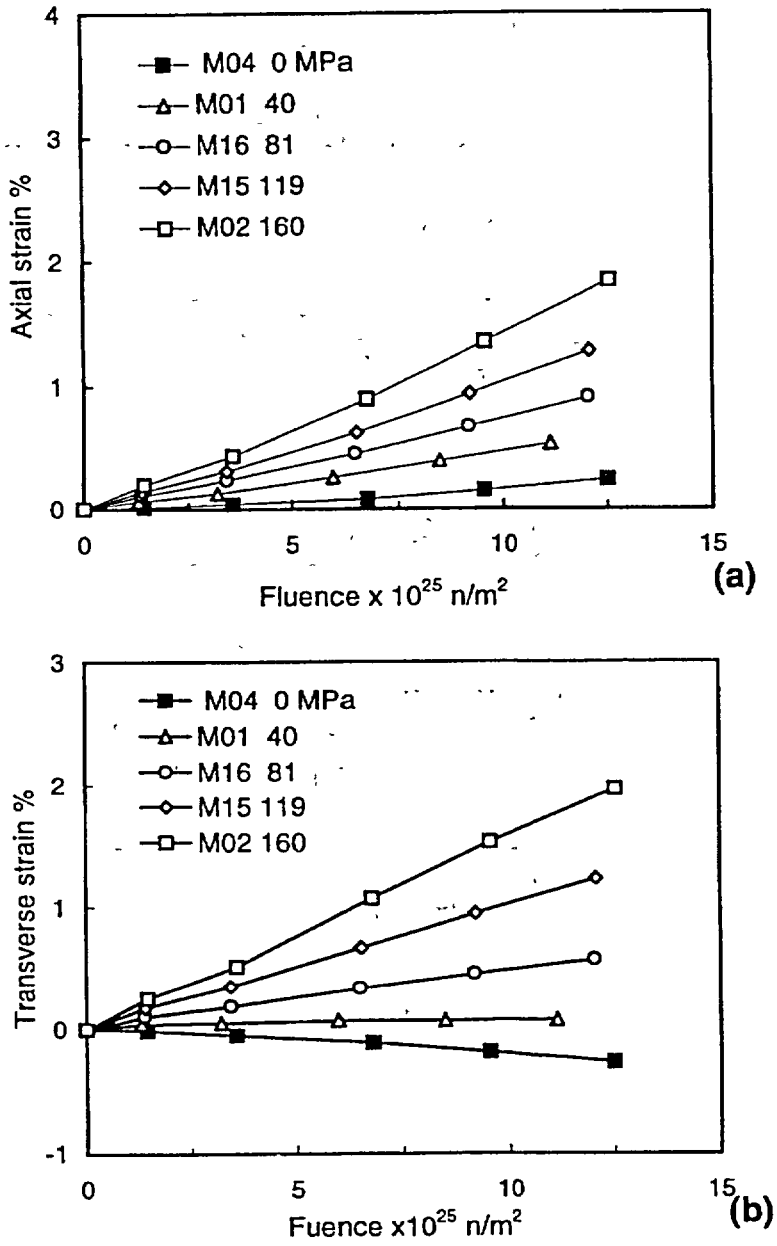

FIG 2—*Creep strain as a function of neutron fluence for specimens from Small Tube M2 irradiated in Trillium 3 at a nominal temperature of 583 K:* (a) *axial strain,* (b) *transverse strain.*

long-term steady state deformation consists of separable, additive components from thermal creep, irradiation creep, and irradiation growth [*1–4*]. The irradiation-induced components are anisotropic and contribute to length as well as diameter changes, while the thermal creep is generally isotropic and does not contribute to length changes. The equation recently developed to describe the deformation of Zr-2.5Nb pressure tubes [*4,7*] has been modified for the analysis of the results presented here as follows:

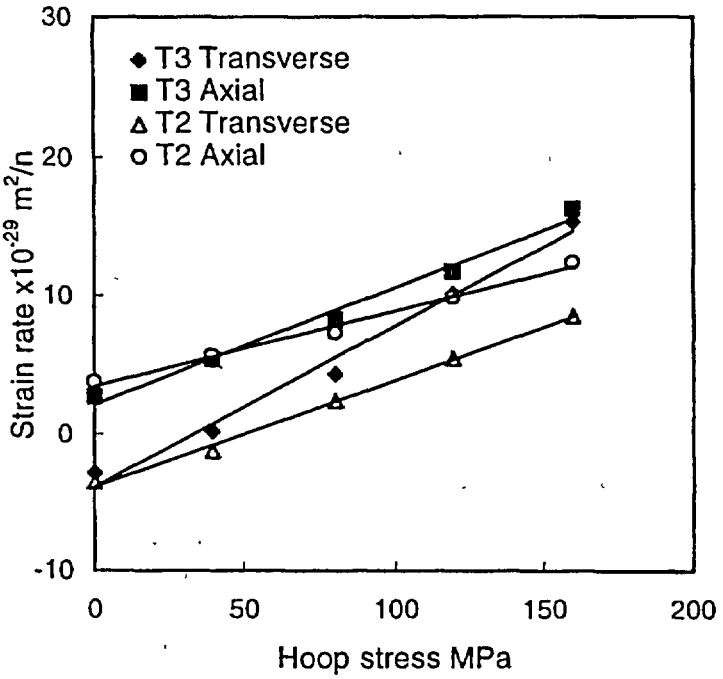

FIG. 3—*Strain rate as a function of hoop stress (axial stress = hoop stress/2) for specimens from Small Tube M2 irradiated in Trillium 2 and Trillium 3*

$$\dot{\varepsilon}_{il} = \dot{\varepsilon}_d^{\text{thermal creep}} + \dot{\varepsilon}_d^{\text{irradiation creep}} + \dot{\varepsilon}_d^{\text{growth}} \tag{1}$$

where

$$\dot{\varepsilon}_d^{\text{thermal creep}} = K_{th}\, C_{th}^{\,d}\, \sigma_{th}^{\,2} \exp\left(-Q_{th}/T\right) \tag{1a}$$

$$\dot{\varepsilon}_d^{\text{irradiation creep}} = K_{\varepsilon}\, C_{\varepsilon}^{\,d}\, \sigma_{\varepsilon}\phi \exp\left(-Q_{\varepsilon}/T\right) \tag{1b}$$

$$\dot{\varepsilon}_d^{\text{growth}} = K_{g}\, G^{d}\, \phi \exp\left(-Q_{g}/T\right) \tag{1c}$$

In the present case the in-reactor thermal creep component contributes at temperatures above 570 K, and the thermal stress exponent is 2. The last two terms describe flux-dependent creep and irradiation growth, respectively. The parameters in Eq 1 are defined as follows:

TABLE 3—*Creep rates and average temperatures derived from Trillium 2 and Trillium 3 data in Fig. 4 over last three irradiation phases.*

Insert	Average Temperature over last 3 Phases, K	$\dot{\varepsilon}_a$, $m^2 \cdot n^{-1} \cdot MPa^{-1}$	$\dot{\varepsilon}_r$, $m^2 \cdot n^{-1} \cdot MPa^{-1}$	$\dot{\varepsilon}_a/\dot{\varepsilon}_r$
Trillium 2	555	0.55×10^{-30}	0.78×10^{-30}	0.705
Trillium 3	588	0.84×10^{-30}	1.16×10^{-30}	0.724
Average				0.715

$\dot{\varepsilon}_d$ = strain rate in a direction d (i.e., radial, transverse, axial), h^{-1},
K_{th} = constant for high-temperature in-reactor thermal creep,
C_{th}^d = anisotropy factor due to texture for in-reactor thermal creep in a given direction d,
C_c^d = anisotropy factor due to texture for irradiation creep in a given direction d,
G_g^d = anisotropy factor due to texture for irradiation growth in a given direction d,
K_c = material constant for irradiation creep,
K_g = material constant for irradiation growth given below,
Q_{th}, Q_c, Q_g = activation temperatures, K,
σ_{th} = effective stresses for thermal creep and a stress exponent of 2, MPa,
σ_c = effective stress for irradiation creep, MPa,
T = temperature in K, and
ϕ = fast flux, $n \cdot m^{-2} \cdot s^{-1}$ ($E > 1$ MeV).

The effective stresses σ_{th} and σ_c are related to the radial, axial, and transverse stress σ_r, σ_a, and σ_t, respectively, by the Hill's anisotropy constants F, G, and H [8], by:

$$\sigma_i = [F_i(\sigma_a - \sigma_t)^2 + G_i(\sigma_t - \sigma_r)^2 + H_i(\sigma_r - \sigma_a)^2]^{1/2} \tag{2}$$

The subscript i stands for th ($n = 2$) in the case of thermal creep and c ($n = 1$) in the case or irradiation creep. Also it is assumed that

$$H = 1.5 - F - G \tag{3}$$

Using the terminology employed in Eq 2, the anisotropy factors due to texture for in-reactor thermal or irradiation creep are given by:

$$\begin{aligned} C_i^r &= [H_i(\sigma_r - \sigma_a) - G_i(\sigma_t - \sigma_r)] \\ C_i^t &= [G_i(\sigma_t - \sigma_r) - F_i(\sigma_a - \sigma_t)] \\ C_i^a &= [F_i(\sigma_a - \sigma_t) - H_i(\sigma_r - \sigma_a)]. \end{aligned} \tag{4}$$

A measure of the creep anisotropy is obtained from the ratio, R, of the axial to transverse creep rates in a closed-end pressurized capsule, which in Hill's notation is proportional to $(H - F)/(2(G + F/2))$. A self-consistent computer code [9,10] was used to calculate F, G, and H constants consistent with the observed R value from the crystallographic texture and an assumed single crystal creep model. The creep model has been taken to be the glide and the climb of the ⟨a⟩ and ⟨c⟩ type dislocations [11]. The code uses the crystallographic texture of the test material in the form of a crystallite orientation distribution function (CODF). The (0002), $(10\bar{1}0)$, $(11\bar{2}0)$, $(11\bar{2}2)$, and $(10\bar{1}1)$ pole figures were determined by X-ray diffraction and used to generate the CODF by three Euler angles as a function of the volume fraction [4]. Experimental data from internally pressurized capsules, stress relaxation specimens, and data from the Pickering NGS were used previously [4,7] to derive the set of eigenvalues, k_1, k_2, and k_3, of the single crystal creep tensor, which described pyramidal, prismatic, and basal climb-assisted guide of dislocations in Zr-2.5Nb pressure tube materials during in-reactor deformation. The set of eigenvalues k_1, k_2, and k_3 derived in Ref 7 were 0.2, 3.8,

TABLE 4—*Creep anisotropy factors for thermal creep and irradiation creep derived from Trillium 2 and Trillium 3 data in Fig. 4, compared with those for CANDU pressure tubes* [4].

Material	Thermal Creep			Irradiation Creep			Ratio
	F_{th}	G_{th}	H_{th}	F	G	H	$= \frac{(H - F)}{2(G + F/2)}$
Small Tube M2	0.33	0.82	0.35	0.378	0.198	0.924	0.705
CANDU tubes	0.38	0.75	0.37	0.350	0.190	0.960	0 840

and 2.0×10^{-9} h^{-1} MPa^{-1}, respectively. The values of F, G, and H calculated for pressure tube material are given in Table 4. The value of R for pressure tube material with these eigenvalues is 0.84.

The R values for the Trillium 2 and Trillium 3 inserts at the average test temperatures of 555 and 588 K in the axial and transverse direction, determined from the last three strain measurements in Figs. 1 and 2, are given in Table 3. It is evident from Table 3 that the creep compliances increase with temperature, whereas the ratio R remains constant at about 0.715. This is in excellent agreement with the ratio predicted using the texture of Tube M2 and the pressure tube eigenvalues; the calculated anisotropy constants, listed in Table 4, give an R value of 0.705. The predicted value of R for Tube M5 is 0.524. The values of F, G, and H for the small tubes are given in Table 4. A non-linear self-consistent code based on a model, described in Ref *12*, was used to calculate Hill's anisotropy constants for thermal creep, F_{th}, G_{th}, and H_{th}. The single crystal creep law assumed to describe the behavior of the material during thermal creep is proportional to the stress to the second power [2]. The single crystal creep parameters needed for the derivation are the values of critical resolved shear stresses (CRSS) for dislocation glide on prismatic, basal, and pyramidal planes and the values used here are 100, 120, and 240 MPa, respectively. The calculated values of F_{th}, G_{th}, and H_{th} for the small tubes are given in Table 4.

The values of the growth anisotropy constants, G^t and G^a, are determined from the experimental ratios of the axial to transverse growth rates of the two specimens with zero hoop stress, M03 and M04, in Trillium 2 and Trillium 3, respectively, and are given in Table 5. The single crystal growth tensor used to calculate G^t and G^a was derived empirically so that the calculated growth rate of the polycrystal agrees with the data. The thermal creep term in Eq 1 reflects the high-temperature dependence of creep rate exhibited by the Zr-2.5Nb pressure tubes determined previously [*4*], and the value of Q_{th} of 25 000 K was used here. The temperature dependence of irradiation creep was derived from the data listed in Table 3 and that for growth was derived from the data for the growth specimens listed in Table 5.

TABLE 5—*Growth rates, growth anisotropy, and average temperatures for Specimens M03 and M04 in Trillium 2 and Trillium 3 over the last three irradiation phases.*

Insert/Specimen	Average Temperature over last 3 Phases, K	$\dot{\varepsilon}_a$, $m^2 \cdot n^{-1}$	$\dot{\varepsilon}_t$, $m^2 \cdot n^{-1}$	$\dot{\varepsilon}_a/\dot{\varepsilon}_t$
Trillium 2/M03	541	4.2×10^{-29}	$-4\,0 \times 10^{-29}$	−0.95
Trillium 3/M04	594	$2\,6 \times 10^{-29}$	$-2\,7 \times 10^{-29}$	−1.04
Average measured ratio for Tube M2				−1.00

The activation temperature constants Q_c and Q_g were found to be equal to 4100 and −2700 K, respectively. The activation temperature for creep is higher than that previously reported for pressure tubes [*4*] and higher than the value of 2200 K given in the first paper on these experiments [*5*]. The activation temperature for the growth component is strongly negative and slightly less than that for pressure tubes [*4*]. The magnitude of Q_g found here is less than that previously reported for pressure tube materials [*6*] derived over a fluence range less than 8×10^{25} n·m^{-2}. It should also be pointed out that Q_g is an apparent activation temperature that reflects the temperature dependence of several microstructural features that compete as sinks for the vacancies and self-interstitials produced by the fast neutron flux. Holt and Fleck [*13*] suggested that in a region where the bias, which controls the segregation of interstitials and vacancies to different sites, is generated by a combination of the strain interaction (SI) and diffusional anisotropy difference (DAD), changing the temperature may change the balance in the net point defect fluxes to the sinks because of the different temperature dependencies of the SI and DAD.

After determining the creep and growth anisotropy constants and the activation temperatures, the thermal creep, irradiation creep, and irradiation growth constants K_{th}, K_c, and K_g were determined by fitting the diametral and axial strain rate data from the Trillium 2 and Trillium 3 experiments. The values of the constants found are $K_{th} = 2.0 \times 10^6$, $K_c = 1.1 \times 10^{-23}$, and $K_g = 9.8 \times 10^{-28}$. Equation 1 describes the data very well as shown in Fig. 4.

Conclusions

1. Axial and transverse strain versus fluence plots for the small tube specimens in Trillium 2 and Trillium 3 are approximately linear over the fluence range from 3 to 15 ×

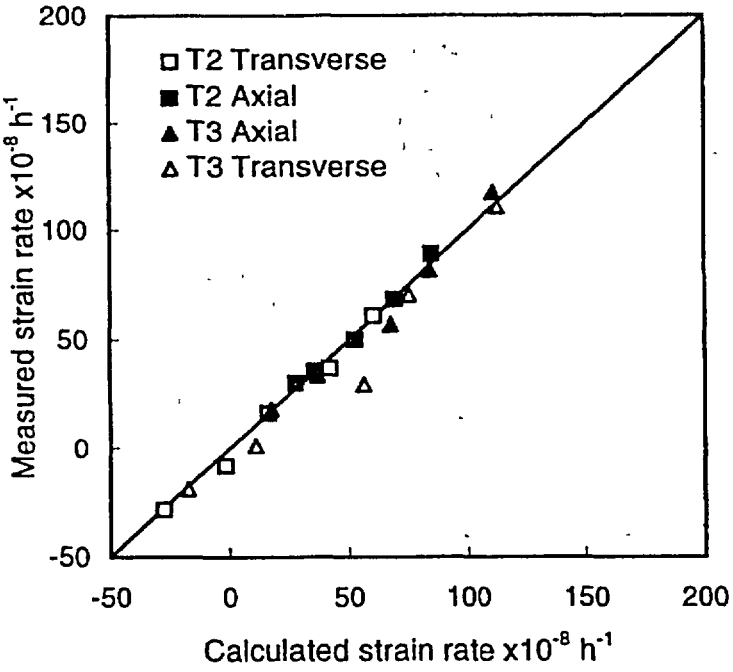

FIG. 4—*Comparison of strain rates calculated by Eq 1 with measured rates for specimens from Small Tube M2 irradiated in Trillium 2 and Trillium 3.*

10^{25} n·m^{-2} and a temperature range between 538 and 594 K. The anisotropy ratio R of axial to transverse strain rates derived from the strain-fluence plots is about 0.71.

2. The temperature dependence of irradiation creep of the small tube, as characterized by the activation temperature Q_c, is equal to 4069 K, a value somewhat higher than that reported previously for the low fluence range and for pressure tube material where Q_c was about 2200 K.

3. The irradiation growth of small tubes, as characterized by a negative activation temperature of Q_g, is equal to −2680 K, and it appears to be lower than that reported previously for pressure tube material.

4. Predictions of the axial to transverse creep anisotropy using the self-consistent model for the effect of texture, derived from pressure tube creep data, are consistent with the ratio R observed here for small tubes.

Acknowledgments

We acknowledge F. J. Butcher and S. A. Donohue for preparing the test specimens; J. E. Winegar for the X-ray diffraction data; A. Alberman, F. Koskas, Y. Bouilloux, M. Roche, and M. Farney for irradiating the specimens in Osiris and measuring the creep strains; and the CANDU Owners Group (COG) for funding the work.

References

[1] Fidleris, V., "The Irradiation Creep and Growth Phenomena," *Journal of Nuclear Materials*, Vol. 159, 1988, p. 22.

[2] Holt, R. A., Causey A. R , and Fidleris, V., "Dimensional Stability and Mechanical Behaviour of Irradiated Metals and Alloys," *Proceedings*, British Nuclear Society, London, 1983, p. 175.

[3] Causey, A. R., Holt, R. A., and MacEwen, S. R., "In-Reactor Creep of Zr-2.5Nb," *Zirconium in the Nuclear Industry, 6th International Symposium, ASTM STP 824*, D. G. Franklin and R. B. Adamson, Eds., American Society for Testing and Materials, Philadelphia, 1984, pp. 269–288.

[4] Christodoulou, N., Causey, A. R., Holt, R. A , Tomé, C. N., Badie, N., Klassen, R. J., Sauvé, R., and Woo, C. H., "Modelling In-Reactor Deformation of Zr-2.5Nb Pressure Tubes in CANDU Power Reactors," *Zirconium in the Nuclear Industry; 6th International Symposium, ASTM STP 1295*, E. R. Bradley and G. P. Sabol, Eds., American Society for Testing and Materials, Philadelphia, 1996, pp. 518–537.

[5] Causey, A. R., Elder, J. E., Holt, R. A., and Fleck, R. G., "On the Anisotropy of In-Reactor Creep of Zr-2.5Nb Tubes," *Zirconium in the Nuclear Industry, 6th International Symposium, ASTM STP 1245*, A. M. Garde and E. R. Bradley, Eds., American Society for Testing and Materials, Philadelphia, 1994, pp. 202–220.

[6] Fleck, R. G., Elder, J. E., Causey, A. R., and Holt, R. A , "Variability of Irradiation Growth in Zr-2.5Nb Pressure Tubes," *Zirconium in the Nuclear Industry, 6th International Symposium, ASTM STP 1245*, A. M. Garde and E. R. Bradley, Eds., American Society for Testing and Materials, Philadelphia, 1994, pp. 168–182.

[7] Christodoulou, N , Causey, A. R., Woo, C. H., Tomé, C. N., Klassen, R. J., and Holt, R. A., "Modelling the Effect of Texture and Dislocation Density on Irradiation Creep of Zirconium Alloys," *Effects of Radiation on Materials, 16th International Symposium, ASTM STP 1175*, A. S. Kumar, D. S. Gelles, R. K. Nanstad, and E. A. Little, Eds , American Society for Testing and Materials, Philadelphia, 1993, pp. 1111–1128.

[8] Hill, R., *The Mathematical Theory of Plasticity*, Oxford University Press, London, 1954.

[9] Woo, C. H , "Paper II. Effects of Intergranular Interaction on the Anisotropy of Irradiation Creep and Growth in Zirconium," *Proceedings*, British Nuclear Society, London, 1987, p. 65.

[10] Tomé, C. N., So, C. B., and Woo, C. H., "Self-Consistent Calculations of Steady-State Creep and Growth in Textured Zirconium," *Philosophical Magazine*, Vol. 67, 1993, p. 917.

[11] Woo, C. H., "Polycrystalline Effects on Irradiation Creep and Growth in Textured Zirconium," *Journal Nuclear Materials*, Vol. 131, 1985, pp. 105–117.

[12] Hutchinson, J. W., "Bounds and Self-consistent Estimates for Creep of Polycrystalline Materials," *Proceedings of the Royal Society of London*, Vol. A348, 1976, p. 101.

[13] Holt, R. A. and Fleck, R. G., "The Effect of Temperature on the Irradiation Growth of Cold-Worked Zr-2.5Nb," *Zirconium in the Nuclear Industry, 8th International Symposium, ASTM STP 1023*, L. F. P. Van Swam and C. M. Eucken, Eds., American Society for Testing and Materials, Philadelphia, 1989, pp. 705–721.

DISCUSSION

P. Bouffioux[1] (*written discussion*)—Did you perform similar creep tests on as-received unirradiated materials, and have you compared the results with those obtained under irradiation?

A. R. Causey (*authors' closure*)—We have not performed any out-reactor creep tests on the materials used in the tests reported in this paper.

K. L. Murty[2] (*written discussion*)—1. How do you define creep compliance? 2. In your thermal creep equation the stress dependence of σ^2 implies grain boundaries as the rate-controlling deformation mechanism, in which case one expects the activation energy for creep to be that for grain boundary diffusion. However, your activation energy value is close to that for self-diffusion. How do you explain the observed discrepancy?

A. R. Causey (*authors' closure*)—1. The slope of the strain rate versus stress curve (see Fig. 3 in the paper). 2. The observed activation temperature is an empirical parameter that may reflect the activation of more than one mechanism, namely, creep due to dislocation glide and/or diffusion-controlled creep. Due to the small component of creep attributed to this term, the authors have not attempted to interpret the vlaue of the Q on mechanistic arguments.

[1] EDF, Moret sur Loing, France.
[2] North Carolina State University, Raleigh, NC.

A. CZUSKY.

R. R. Hosbons,[1] P. H. Davies,[2] M. Griffiths,[2] S. Sagat,[2] and C. E. Coleman[1]

Effect of Long-Term Irradiation on the Fracture Properties of Zr-2.5Nb Pressure Tubes

REFERENCE: Hosbons, R. R., Davies, P. H, Griffiths, M., Sagat, S, and Coleman, C. E., **"Effect of Long-Term Irradiation on the Fracture Properties of Zr-2.5Nb Pressure Tubes,"** *Zirconium in the Nuclear Industry· Twelfth International Symposium, ASTM STP 1354,* G. P. Sabol and G. D. Moan, Eds., American Society for Testing and Materials, West Conshohocken, PA, 2000, pp. 122–138.

ABSTRACT: Results from fracture toughness and tensile and delayed hydride cracking (DHC) tests on Zr-2.5Nb pressure tubes removed from CANDU power reactors in the 1970s and 80s for surveillance showed considerable scatter. At that time, the cause of the scatter was unknown and prediction of fracture toughness to the end of the design life of a CANDU reactor using the surveillance data was difficult. To eliminate the heat-to-heat variability and to determine end-of-life mechanical properties, a program was undertaken to irradiate, in a high-flux reactor, fracture toughness, DHC, and transverse tensile specimens from a single "typical" pressure tube. Two inserts were placed in the OSIRIS reactor at CEA, Saclay, in 1988 Each insert held 16 of each type of specimen. The first insert, ERABLE 1, was designed so that half the specimens could be replaced at intervals and the properties could be measured as a function of fluence. All the specimens would be removed after a total fluence of 15×10^{25} n·m^{-2}, $E > 1$ MeV. The second insert, ERABLE 2, was designed to run without interruption to a fluence of 30×10^{25} n·m^{-2}, the fluence corresponding to 30 years' operation of a CANDU reactor at 90% capacity factor. The irradiation temperature was chosen to be 250°C, the inlet temperature of early CANDU reactors. The irradiation of ERABLE 1 has been completed and sets of specimens have been removed and tested with maximum fluences of approximately 0.7, 1.7, 2.8, 12, and 17×10^{25} n·m^{-2}, $E > 1$ MeV. X-ray and TEM examinations have been performed on the material from fractured specimens to characterize the irradiation damage. Results showed that there is, initially, a large change in the mechanical properties before a fluence of 0.6×10^{25} n·m^{-2}, $E > 1$ MeV (corresponding to an initial rapid increase in a-type dislocation density), followed by a gradual change. As expected, the fracture toughness decreased with fluence, whereas the yield strength, UTS, and DHC crack velocities all increased. Z-ray analysis showed that, although the a-type dislocation density remained constant after the initial increase, the number of c-component dislocations showed a steady increase, agreeing with the behavior seen in the mechanical specimens. Because the flux in OSIRIS is different from that in a CANDU reactor, specimens were also irradiated in NRU, a heavy water moderated test reactor with approximately the same flux as a CANDU reactor, to fluences of 0.3, 0.6, and 1.0×10^{25} n·m^{-2}, $E > 1$ MeV for comparison. These initial results show that, once past the initial transient, one can have confidence that there will be little further degradation with fluence, with the results from the NRU specimens being similar to those from OSIRIS.

KEYWORDS: irradiation, fracture, pressure tubes

[1] Managers, AECL, Chalk River Laboratories, Chalk River, Ontario K0J1J0, Canada.
[2] Senior researchers, AECL, Chalk River Laboratories, Chalk River, Ontario K0J 1J0, Canada.

During operation of a CANDU reactor, the cold-worked Zr-2.5Nb pressure tubes have to withstand severe conditions: heavy water flows through the tubes at temperatures between about 250 and 310°C, at pressures of about 10 MPa, and the maximum flux of fast neutrons from the fuel is about 4×10^{17} n·m^{-2}·s^{-1}. With time the tubes deform and the fracture properties degrade. We need to know whether these factors will limit the life of the tubes. This paper describes the results from tests on fracture properties carried out halfway through a long-term irradiation that will achieve the fast neutron fluence expected at the end of the design life of the pressure tubes, about 30×10^{25} n·m^{-2} for the current reactor design (all neutron fluences in this paper are for $E > 1$ MeV).

One criterion for limiting the lifetime of a pressure tube would be an inability to defend "leak-before-break" (LBB). LBB is achieved if a crack initiates, penetrates the tube wall, and the leakage of heavy water is detected before the crack grows to the critical crack length (CCL) and becomes unstable. The most likely crack propagation mechanism is delayed hydride cracking (DHC), which determines the rate of crack growth. CCL is governed by the fracture toughness.

Previous measurements of these fracture properties on sample removed from pressure tubes that had been in service showed an initial transient degradation [*1*]. The results were very scattered because the samples were taken from different tubes, and the scatter masked any long-term degradation of the properties. Thus, to observe whether there was a long-term degradation it was decided to accelerate the irradiation, and to a single material. A tube representative of the low end of the fracture properties was chosen, and two irradiation sites in the OSIRIS reactor at CEA (Commissariat à l'Energie Atomique), Saclay, were used. This reactor provided fast neutron fluxes an order of magnitude greater than those in the center of a CANDU power reactor. In one insert, ERABLE 1, specimens could be removed at intervals to characterize the initial transient degradation and provide guidance to the subsequent property changes. In the second insert, ERABLE 2, the irradiation will continue to the lifetime fluence without interruption. The irradiation temperature is 250°C. This temperature represents the inlet end of a CANDU fuel channel and is the temperature of operation at which the fracture properties are degraded most [*1,2*].

The microstructure resulting from extrusion and cold-work consists of thin, platelet-like, hexagonal close-packed (hcp) α-zirconium grains (containing up to about 1 wt% Nb) interspersed with a network of metastable body-centered-cubic (bcc) β-zirconium (containing about 20 wt% Nb). Irradiation at moderate temperatures changes the microstructure of the pressure tube [*3*]: dislocation loops are generated from the point defects and β-Nb precipitates from the supersaturated α-phase and the β-phase changes. These changes have been evaluated using X-ray diffraction and transmission electron microscopy (TEM).

Experimental Procedures

Material

Zr-2.5Nb pressure tubes for CANDU reactors are manufactured by extrusion, after β-quenching, of hollow forged billets at a temperature of about 815 to 850°C, i.e., in the (α+β)-phase field. The tubes are 27% cold-drawn to give a final tube thickness of about 4.2 mm and inside diameter of about 103 mm, followed by an autoclave treatment at 400°C for 24 h. The tube selected for the test material was H737; it had a texture typical of that found in CANDU pressure tubes and was made using the process used for other pressure tubes [*4*]. The material was given a simulated autoclave treatment since H737 was rejected before that operation. The principal elements in the chemical analysis are given in Table 1.

TABLE 1—*Chemical composition of tube H737.*

Element	Weight
Niobium	%
Oxygen	ppm
Carbon	ppm
Chromium	ppm
Hydrogen	ppm
Iron	ppm
Nickel	ppm
Nitrogen	ppm
Silicon	ppm
Chlorine	ppm
Phosphorus	ppm
Tantalum	ppm

Preparation of Specimens

The transverse tensile specimens were machined from flattened rings cut from the mid-length of tube H737. After flattening, the strips were stress relieved for 24 h at 400°C, in vacuum, simulating the autoclave treatment given production tubes. Specimens oriented for loading in the transverse direction were then machined with a round cross section of diameter, 3.6 mm, and a gage length of 16 mm.

For fracture toughness testing, 17-mm-wide curved compact specimens were machined directly from the mid-length of tube H737. The 17-mm-wide specimen is the standard-width specimen used for testing CANDU reactor pressure tube material [*5*], but due to space limitations in the OSIRIS insert, the height of the current specimens was reduced from 20.4 to 18.4 mm. The crack plane was the radial-longitudinal with the crack running in the longitudinal direction.

The cantilever beam specimens, 38 by 3.2 by 4 mm [*2*], used for the DHC experiments had a radial-longitudinal crack plane with the crack running in the radial direction. They were hydrided gaseously and homogenized at 400°C for 72 h, giving a hydrogen concentration of 100 wt ppm (0.90 at%). Therefore, after machining, the tensile and fracture toughness specimens were heat treated at 400°C in vacuum to produce a similar stress-relieved condition, the former being heat treated for an additional 48 h (total of 72 h) and the latter for 72 h.

The metastable β-phase filaments in the microstructure decomposed partially during this final stress-relief treatment of 72 h at 400°C to give a mixture of Nb-depleted, hcp ω-phase embedded in the remaining Nb-enriched, bcc β-phase.

Irradiation Conditions

Specimens were irradiated in the OSIRIS high-flux reactor and in NRU, which has a flux spectrum close to that of a CANDU power reactor.

OSIRIS

Specimens were irradiated in a central site of the OSIRIS reactor where the flux is 1.8×10^{18} $n \cdot m^{-2} \cdot s^{-1}$. The OSIRIS insert, containing 16 transverse tensile, 16 cantilever beam DHC, and 16 curved compact specimens, was designed so that specimens in the bottom half

could be replaced periodically, allowing a number of different neutron fluences to be obtained. Specimens were replaced after 2, 7, and 17 reactor cycles, giving specimen sets of 2, 5, 10, 34, and 51 cycles with maximum fluences of 0.7, 1.7, 2.8, 12, and 17 $\times$ 10^{25} $n \cdot m^{-2}$, respectively. Each reactor cycle is 20 days, and with shutdowns the total elapsed time for the irradiation was approximately seven years. There was a cosine flux distribution along the insert, and the minimum fluence received by any specimen in a set was 74% of the maximum. The specimens were irradiated at a temperature of 250°C in NaK to remove the γ heat. Both copper and nickel wire flux monitors were located at different parts of the insert to give the flux profile.

In OSIRIS, heat is deposited in the specimens by γ radiation, which is proportional to the fast flux and thus varies both with axial distance in the insert and with time as the power from the fuel decreases. They γ heating gives rise to a maximum calculated temperature difference of 11°C from the center to the surface in the fracture toughness specimens, but this gradient varies from specimen to specimen depending on its position in the insert.

NRU

Most of the irradiation in NRU took place in a light water insert attached to the U5 loop. The flux in this reactor position is approximately 1.5 $\times$ 10^{17} $n \cdot m^{-2} \cdot s^{-1}$. The insert was operated at 265°C. The fluences received were between 0.29 and 0.95 $\times$ 10^{25} $n \cdot m^{-2}$. Specimens irradiated to 0.3 and 0.6 $\times$ 10^{25} $n \cdot m^{-2}$ were irradiated in the U5 loop, but the loop was shut down before a fluence of 0.95 $\times$ 10^{25} $n \cdot m^{-2}$ was reached and the irradiation was continued in the U2 loop in a materials test bundle (MTB). The flux in the MTB was 4.5 $\times$ 10^{17} $n \cdot m^{-2} \cdot s^{-1}$ at a temperature of 267°C.

Testing of Transverse Tensile and Fracture Toughness Specimens

The transverse tensile specimens were tested in duplicate at 240°C in an air furnace at constant displacement rate corresponding to a nominal strain rate of 10^{-3} s^{-1}.

The fracture toughness specimens were also tested at 240°C following the standard method for fracture toughness testing of CANDU reactor pressure tubes [*5*]. After fatigue precracking, the fracture testing was carried out at a constant displacement rate corresponding to an initial rate of increase of the stress intensity factor of about 1 MPa$\sqrt{m \cdot s^{-1}}$. The d-c potential-drop method was used to monitor the crack growth. At the end of a test, the final crack front position was marked either by fatigue (unirradiated control specimens) or by heat tinting (irradiated specimens) before breaking open the specimens to determine the initial and final crack lengths. The total crack extension was then used to calibrate the potential drop signal for each specimen individually. For the high-flux irradiation program, a single irradiated specimen was available for each different fluence. However, duplicate specimens were available for the unirradiated and irradiated (NRU control) tests.

A crack growth resistance (or *J-R*) curve was produced for each fracture toughness test following the procedures in Ref *5*. Due to the reduced height of the curved compact specimens, corrections were required to the standard equations for the elastic compliance and elastic stress intensity factor. Each *J-R* curve was characterized using the following parameters:

(*a*) Crack initiation toughness, $J_{0.2}$, i e., the *J*-integral value at the intersection of the 0.2 mm offset line and *J-R* curve.

(*b*) $J_{1.5}$, i.e., the *J*-integral value at the intersection of the 1.5-mm offset line and the *J-R* curve.

(*c*) $J_{3.0}$, i.e., the *J*-integral value at the intersection of the 3.0-mm offset line and the *J-R* curve.

(*d*) Maximum load toughness, J_{mt}, i.e., the *J*-integral value corresponding to the maximum load point.

(*e*) Initial crack growth toughness, dJ/da, i.e., the linear regression slope of the *J-R* curve between the 0.15 and 1.5 mm offset lines.

Testing of DHC Specimens

The DHC tests to measure the crack velocity in the radial direction were performed according to a standard procedure [2]. In this procedure, the test temperature is attained by cooling from a higher temperature (peak temperature) to achieve supersaturation of the zirconium matrix with hydrogen to assure the maximum value of crack velocity. Ideally, the peak temperature should exceed the solvus temperature of hydrogen in zirconium for a given hydrogen concentration to achieve complete dissolution of zirconium hydrides. However, in irradiated material, to prevent annealing of irradiation damage, the peak temperature should not exceed the irradiation temperature by more than 10 to 15°C. In these experiments, the peak temperature was set to 270°C and the test temperature was derived by trial experiments in which the test temperature was decreased until the maximum velocity was obtained. The test temperature was then set to 240°C. Once the test temperature was attained, the specimen was loaded in bending to a stress intensity factor of about 17 MPa$\sqrt{m}$. After a sufficient crack growth was indicated by acoustic emission, e.g., about 0.5 mm, the specimen was broken open and the fracture area measured. The crack velocity was calculated from the average crack growth and the time during which cracking occurred.

X-ray and TEM Analysis

X-ray diffraction (XRD) specimens about 100 mm^2 in area by 0.5 mm thick were prepared by cutting slices from the curved compact specimens with normals corresponding to each of the three principal tube axes, i.e., perpendicular to the radial (R), longitudinal (L), and transverse (T) directions of the tubes. Each specimen was chemically polished using a solution of 5% HF, 45% HNO_3, and 50% H_2O to remove at least 0.025 mm (the depth of damage from the low-speed diamond wheel used to cut the specimen). Dislocation densities and lattice parameters were determined from line-broadening analysis of X-ray diffraction peaks obtained using a Rigaku diffractometer with a 12-kW (rotating anode) generator with Ni-filtered, CuK_α radiation and, for high diffraction angles, a Siemens diffractometer and a 1-kW X-ray generator with Ni-filtered, CuK_α radiation. Measurements of the bcc (200) lattice parameter give information about the state of the beta-phase [2]. Measurements on the broadening of the $(30\bar{3}0)$ and $(11\bar{2}0)$ prism-plane diffraction lines of the hcp α-phase (referred to as L(3030) and R(1120), respectively, in the figures) give information about **a**-component dislocation densities and measurements of the broadening of the (0004) basal-plane diffraction lines (referred to as L(0004) and R(0004), respectively) give information about **c**-component dislocation densities [6].

Transmission electron microscopy (TEM) specimens were prepared by punching 3-mm-diameter disks out of 0.1-mm-thick slices whose surfaces were perpendicular to the longitudinal direction of the tube. Foils were made from the disks by electropolishing with a solution of 10% perchloric acid in methanol at about −40°C with a current density of about 0.01 A mm^{-2} using a Materials Science Northwest twin-jet apparatus. TEM analysis was performed using a Philips CM 30 (300-kV) electron microscope. Microchemical analyses were obtained by energy dispersive X-ray analysis (EDXA) using a Link ISIS analyzer

system and super atmospheric thin window (SATW) detector. The spatial resolution for microchemical analysis was about 5 to 8 nm.

Results

Transverse Tensile Strength

In a previous study on the first set of NRU specimens and on the first, second, and third sets of OSIRIS specimens [*3*], the UTS occurred at very low plastic strains close to the 0.2% offset, indicating the low work-hardening capacity of the irradiated material up to maximum load. Thus the peak or ultimate tensile strength (UTS) values differed little from the engineering (0.2% offset) yield stress values, and the UTS values are considered more reliable. After the peak load, there was evidence of strain localization or discontinuous yield in many cases, as indicated by a series of serrations in the load-displacement output. This was also shown by the presence of intense deformation bands on the surface of the specimens at an angle of 45° to the tensile axis. The final fracture surface consisted of central flat fracture zone, with shear lips following these bands.

Figure 1 summarizes the UTS results obtained from the different specimen sets as a function of the fast neutron fluence. In the earlier work [*3*], it was noted that the results showed an initial steep transient at low fluences (<2 to 3 × 10^{24} n·m^{-2}) with little further increase in UTS for the first three sets of OSIRIS specimens irradiated to fluences of up to

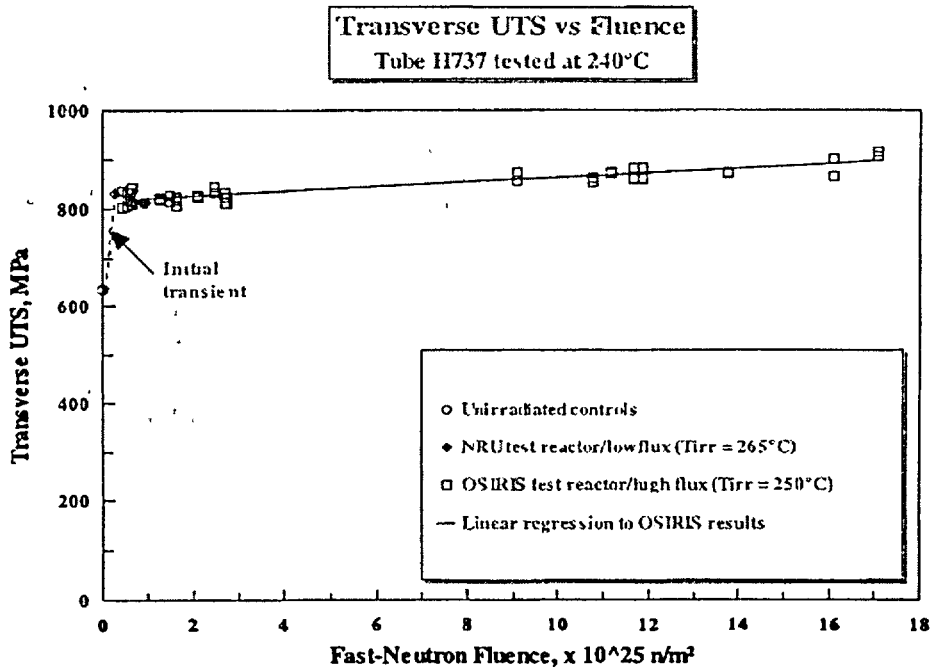

FIG. 1—*Transverse UTS of single pressure tube H737 (tested at 240°C) irradiated in NRU and OSIRIS test reactors showing linear increase in transverse UTS with fast neutron fluence after initial transient.*

2.7×10^{25} n·m^{-2}. However, inclusion of the results from the fourth and fifth sets of OSIRIS specimens here shows a small, but measurable, further increase in strength at higher fluences.

A linear regression analysis of the OSIRIS test results produced the following relationship between the transverse UTS and fluence for a fluence range of 0.45×10^{25} to 1.7×10^{26} n·m^{-2}:

$$\sigma_u = 815 + 4.7 \cdot \phi t \qquad R = 0.92$$

σ_u = UTS in units of MPa,
ϕt = fast neutron fluence in units of 10^{25} n·m^{-2}, and
R = correlation coefficient.

The upper and lower 95% confidence limits for the slope are 5.4 and 4.0, respectively, indicating that the slope is significantly different from zero.

Alternatively, the initial transverse tensile strength UTS of tube H737 was 635 MPa, giving an increase in transverse UTS with fluence for this tube of

$$\Delta\sigma_u = 180 + 4.7 \cdot \phi t \qquad R = 0.92$$

The value of the constant (initial increase in transverse UTS with irradiation) of 180 MPa is in good agreement with previous results from eight different pressure tubes irradiated in NRU to a fluence of 0.21×10^{25} n·m^{-2} [3].

As in the previous case for the first set of specimens [3], the results from the second and third sets of NRU specimens are in good agreement with those obtained from the OSIRIS irradiation, i.e., results from the lower-flux (NRU) irradiation are in good agreement with those from the higher-flux (OSIRIS) irradiation over the limited fluence range of the NRU test results, i.e., $<1 \times 10^{25}$ n·m^{-2}. This agreement between the two sets of results suggests that while the fluence has an effect, there is little effect of fast neutron flux on strength.

Fracture Toughness

Figure 2 shows a plot of the initial crack growth toughness, dJ/da versus fast neutron fluence, with the results from NRU included for comparison.

As in the previous study for specimens irradiated to lower fluences [3], the present results exhibit significant scatter. For the OSIRIS specimens the scatter may be due partly to the effects of γ-heating associated with a high-flux test facility. Other factors contributing to this variability in results include variations in (*a*) irradiation temperature during operation of the test facilities, and (*b*) material properties from specimen to specimen.

The results from the NRU specimens were generally within the band of results for those from the OSIRIS irradiation (Fig. 2). This agreement indicates that the high-flux facility can provide results equivalent to those of a lower-flux test facility, i.e., there appears to be no significant effect of neutron flux on the change in toughness. The results continue to demonstrate that the major degradation in toughness of Zr-2.5Nb pressure tube material occurs at low fluences $<3 \times 10^{24}$ n·m^{-2}, with little further change with increasing irradiation [3].

Linear regression analysis to the OSIRIS test results produced the following relationships between the different toughness parameters and fluence for a fluence range of 4.0×10^{24} to 17.1×10^{25} n·m^{-2}:

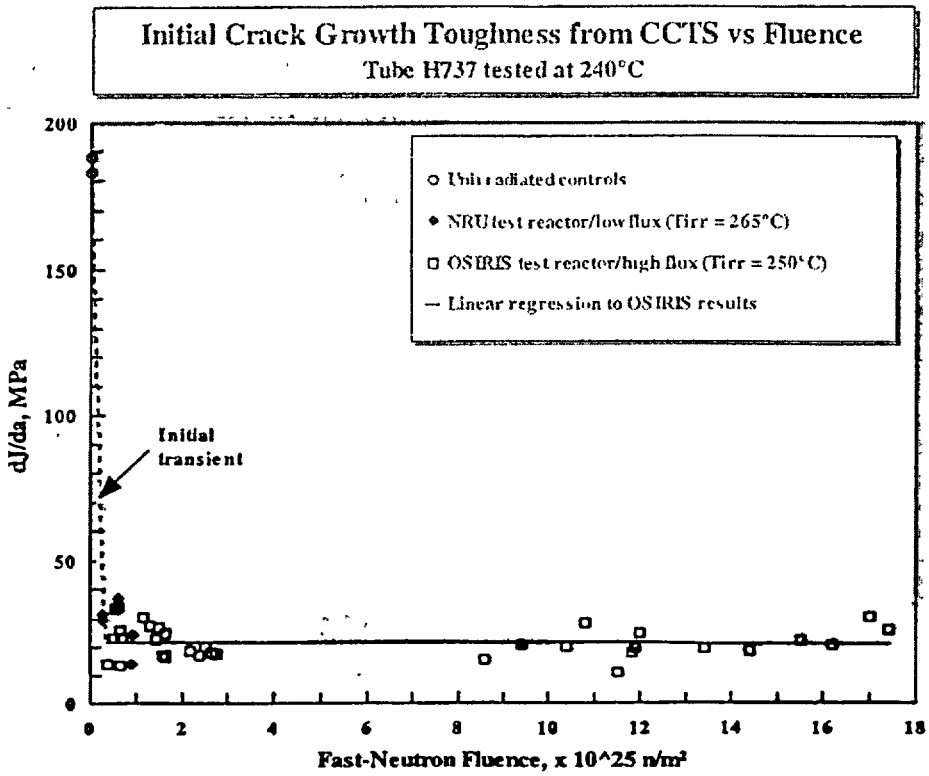

FIG. 2—*Initial crack growth toughness,* dJ/da, *at 240°C of single pressure tube H737 (from CCTS) irradiated in NRU and OSIRIS test reactors showing toughness to be almost independent of fast neutron fluence after initial transient.*

1. $J_{0.2} = 10.6 + 0.054 \cdot \phi_t \qquad R = 0.25$
   or $J_{0.2} = 10.9$ (assuming zero slope)
2. $J_{1.5} = 39.7 + 0.027 \cdot \phi_t \qquad R = 0.021$
   or $J_{1.5} = 39.8$ (assuming zero slope)
3. $J_{30} = 81.9 - 0.57 \cdot \phi_t \qquad R = 0.29$
4. $J_{ml} = 55.2 - 0.53 \cdot \phi_t \qquad R = 0.38$
   (maximum load occurs between 1.3 and 2.3 mm of crack growth)
5. $dJ/da = 21.7 - 0.034 \cdot \phi_t \qquad R = 0.036$
   (regression fit between 0.15 and 1.5 mm offset lines)

where the J-values are in units of kJ · m^{-2} and dJ/da is in units of MPa. Apart from the equations for J_{ml} and J_{30}, the slopes are not significantly different from zero. The much lower values obtained here for the correlation coefficients, R, compared with those for the tensile test results, reflects clearly the increased sensitivity of the J-R curve to variations in the microstructure, as well as the other factors mentioned above, compared with the tensile strength.

Such results confirm that, after the initial transient, there is little effect of fluence on toughness, and any effect is only apparent at the largest crack extensions, i.e., greater than about 1.5-mm crack growth. For example, after the initial decrease in toughness, the effect of an increase in fluence of 1×10^{25} n·m^{-2} is predicted to be a reduction in the $J_{3.0}$, J_{ss}, and dJ/da parameters of only 0.57 kJ·m^{-2}, 0.53 kJ·m^{-2}, and 0.034 MPa, respectively.

Early CANDU reactor pressure tubes exhibited large variations in toughness, primarily due to variations in the concentration of trace elements, notably chlorine and phosphorus [3,7–9]. The results obtained here for tube H737 (Cl = 4 wt ppm, P = 4 wt ppm) may be considered characteristic of tubes of low toughness Other programs are in place to study the behavior of tubes of intermediate and high toughness.

DHC

Crack velocity tests were performed on unirradiated control specimens and on specimens irradiated in the ERABLE insert. The results show that the crack velocity does not completely saturate with fluence at 1×10^{25} n·m^{-2}, as indicated previously from limited data [2], but continues to increase at a significantly reduced rate, Fig. 3.

X-ray and TEM

Dislocation Structure

Irradiation resulted in the formation of a high density of a-type dislocation loops, i.e., dislocation loops having Burgers vectors of $1/3<11\bar{2}0>$. In general, the a-type dislocation

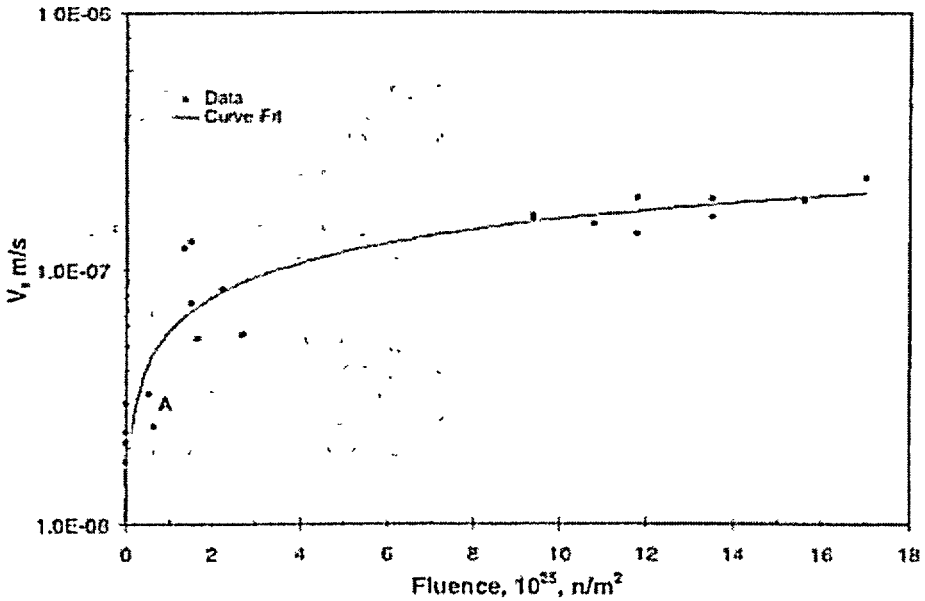

FIG. 3—*Dependence of radial DHC velocity at 240°C on irradiation fluence. Point A marks the fluence at which recrystallization of the β-phase completes.*

density increases rapidly at low fluences ($<1 \times 10^{25}$ n·m^{-2}) and there is little further change in the a-type dislocation structure detectable by either TEM or XRD analysis. The c-component dislocation structure, however, evolves at a slower rate, over longer periods of the irradiation. The development of the a- and c-type dislocation structure is illustrated by the plots of prism- and basal-plane line-broadening as a function of fluence, Fig. 4. The change in c-component dislocation structure is most apparent in those α-grains having their c-axis oriented towards the radial direction, Fig. 5. The increased line-broadening in this case is associated with climb of existing c-component dislocations of screw character [*10,11*]. The tendency for increased line-broadening for grains with their c-axis oriented towards the radial direction appears to be a direct consequence of the preferred nucleation of c-component dislocation loops on existing screw dislocations to form helices, screw dislocations being more prevalent in these grains. The initial transient line-sharpening for grains with their c-axis oriented towards the transverse direction can be attributed to splitting of the (predominantly edge type) c-component dislocations in these grains [*3,6*]. This splitting comes about initially during irradiation because the high strain energy associated with double-layer dislocations of this type can be reduced by climb of one layer with respect to the other in a direction perpendicular to the Burgers vector. Such climb doubles the total line length but reduces the strain energy per unit length by a factor of four. Helical climb of screw dislocations in grains with their c-axis oriented towards the radial direction (Fig. 4), however, increases the total strain energy and the total line-length, resulting in increased line-broadening.

From XRD and TEM data the a-type dislocation structure appears not to be evolving further after the initial transient, i.e., for fluences $>1 \times 10^{25}$ n·m^{-2}. However, both TEM and XRD show that the c-component dislocation structure is evolving gradually with in-

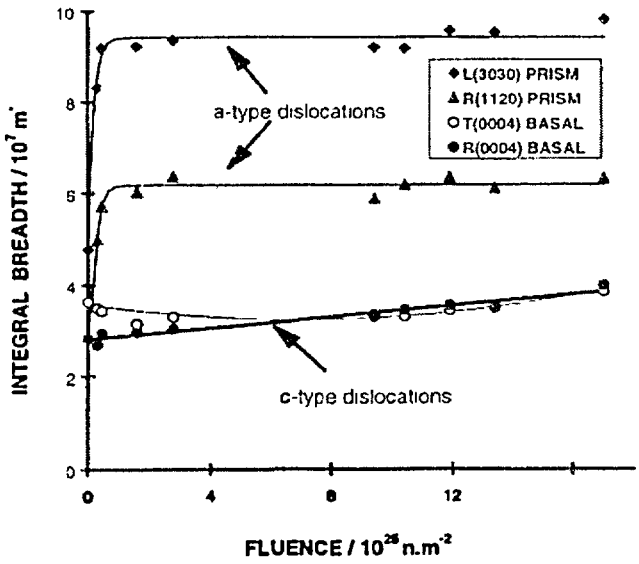

FIG. 4—*Variation of integral breadths for prism- and basal-plane diffraction lines in tested H737 curved compact specimens as a function of fluence.*

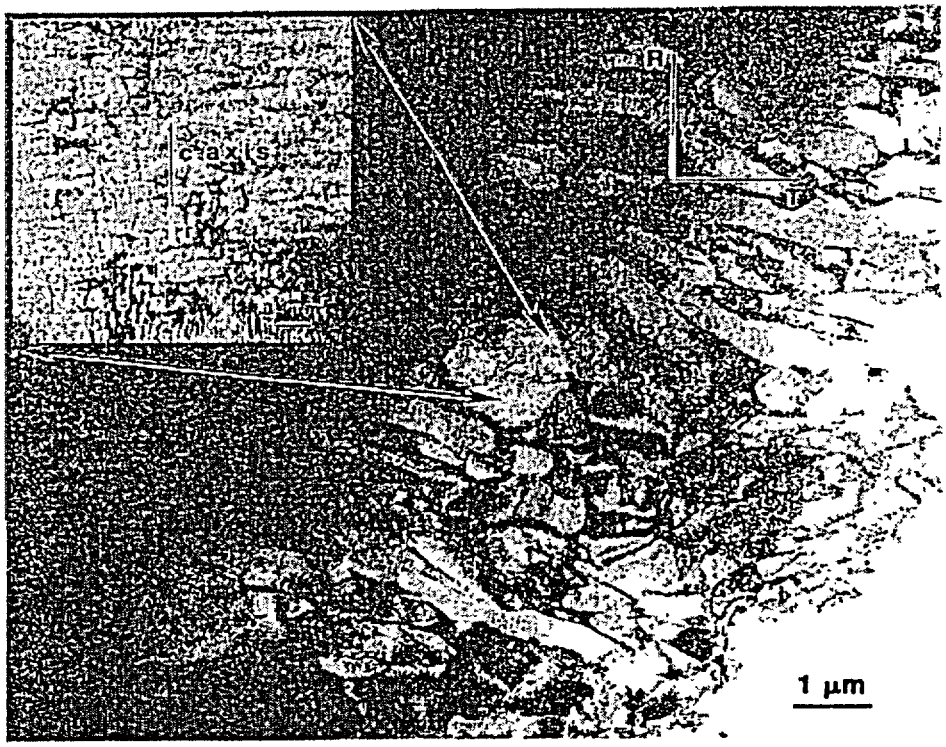

FIG. 5—*Micrograph illustrating the microstructure in H737 curved compact tension specimens after irradiation to a fluence of* 17×10^{25} $n \cdot m^{-2}$ *at 250°C. Grains with their c-axis in the radial* (R) *direction contain a high density of c-component dislocations* (inset).

creasing high fluences, particularly for grains oriented with their c-axis towards the radial direction of the original pressure tube.

Phase Stability

The β-phase structure of the pressure tube material irradiated in OSIRIS changes significantly as a result of irradiation at 250°C. There is a lattice expansion in the β-phase observed during irradiation that can be interpreted as a reduction of the Nb concentration in solution, Fig. 6. There is a corresponding reduction in the relative volume fraction of omega-phase in the "beta-phase" filaments, indicating that the reduced Nb concentration is the result of an increase in the volume fraction of the Nb-rich bcc component of the "beta-phase" filaments. The amount of Nb present before irradiation will depend on any prior heat treatment. The current specimens were heated for 72 h at 400°C instead of the standard 24 h, and this additional treatment would produce more Nb in solution initially but the equilibrium concentration after irradiation will eventually be the same.

The α-phase structure also changes with Nb-rich precipitates forming from the supersaturated solid solution at high fluences, Fig. 7.

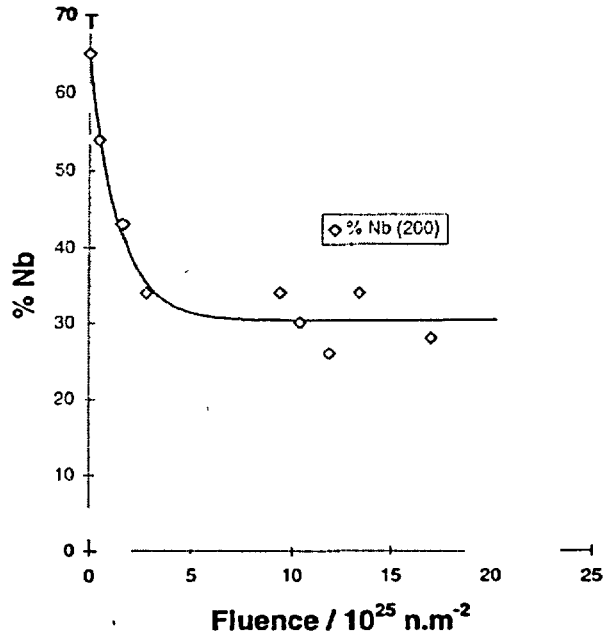

FIG. 6—*Nb concentration of the β-phase (determined from bcc lattice parameters) as a function of fluence for curved compact specimens of H737 irradiated in the OSIRIS reactor at 250°C.*

Discussion

Irradiation changes the microstructure of the pressure tube and the changes in the mechanical properties are a result of this. Thus, it is relevant to discuss the microstructural changes first.

The TEM and XRD data confirm the previous conclusions that the a-type dislocation structure evolves very rapidly in the early stages of irradiation due to a-type dislocation loop formation with little further change with increasing fluence. The change in a-type dislocation density relates directly to the changes in UTS, Fig. 1. The inverse dependence on the temperature of irradiation for the measured increment in UTS in CANDU pressure tubes is also consistent with the inverse dependence on temperature of irradiation of a-type dislocation density reported previously [2]. The c-component dislocation structure evolves over a longer period and is most pronounced in grains with their c-axis oriented towards the radial direction. The c-component dislocation loops that are observed evolving in these particular grains have c and a-components to their Burgers vectors (normally $1/6\langle 20\bar{2}3\rangle$). Calculations converting the line-broadening data to dislocation densities (using two orders of reflection) suggest that there may be a gradual change in a-type dislocation density with increasing fluence that is not apparent from the TEM observations. However, when one takes into account that there is an increase in c-component dislocation density with increasing fluence, it is feasible to consider that the apparent change in a-type dislocation density arises from the increasing a-component contribution from the c-component dislocations.

Previously it was conjectured that there might be an acceleration in the evolution of the a-dislocation density at a fluence of 8×10^{25} n·m^{-2} [3]. The results from OSIRIS, Fig. 4, show that there is a steady small increase in the dislocation density with fluence.

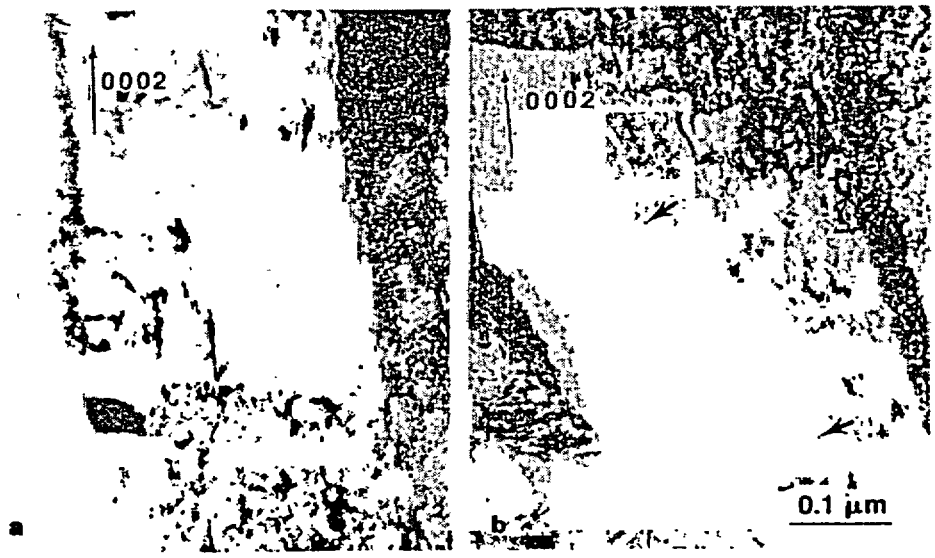

FIG. 7—*Micrographs illustrating the evolution of β-Nb precipitates in H737 curved compact specimens after irradiation to a fluence of.* (a) 2.8×10^{25} $n \cdot m^{-2}$, *and* (b) 17×10^{25} $n \cdot m^{-2}$ *at 250°C. Precipitates* (arrowed) *are visible only at the higher fluence.*

After an initial decrease, the fracture toughness remains constant except at larger crack extensions. However, even at larger crack extensions (>1 mm) the change in toughness with fluence is small (<1% decrease per increase in fluence of 1×10^{25} $n \cdot m^{-2}$) and is masked by the specimen-to-specimen variability. Thus, the conclusion is that the fracture toughness remains constant after the initial transient.

Two parameters have been identified that affect the DHC crack velocity in preirradiated Zr-2.5Nb pressure tube material [2]:

Irradiation hardening, where the crack velocity increases with increase in strength.
Hydrogen diffusivity. Hydrogen diffuses faster in the β-phase than in the α-phase, but as the β-phase decomposes and disintegrates from a continuous phase containing 20% Nb to a discontinuous one containing about 80% Nb, the diffusivity decreases. Also, the β-phase allows more hydrogen in solution than the α-phase and consequently allows better transport but as the β-phase decomposes less hydrogen can diffuse through it [*13*]. As the β-phase becomes more continuous and its volume fraction increases, the faster the hydrogen can diffuse giving increased DHC crack velocities.

The strength initially increases rapidly with fluence followed by a much reduced rate of increase thereafter, Fig. 1, whereas the fluence dependence of the crack velocity has a more gradual initial transient but does reflect the long-term increase in strength, Fig. 3. The transient in the crack velocity is complicated by the partial reconstitution of the β-phase, Fig. 6. This reconstitution contributes to the increase in crack velocity, but the change is complete after about 3×10^{25} $n \cdot m^{-2}$ rather than after about 0.5×10^{25} $n \cdot m^{-2}$ for the strength

transient; thus, the values of DHC velocity at low fluences, A in Fig. 3, are lower than expected if they were completely controlled by strength.

Summary

The results from the OSIRIS reactor show that all mechanical properties measured exhibit an initial transient and then either a slow change or no change with further irradiation. The results from OSIRIS and NRU show that the difference of the fluxes of the two reactors has no effect on the mechanical properties. This gives confidence in our understanding and predictions for the future operation of Zr-2.5Nb pressure tubes in CANDU reactors.

Acknowledgments

The authors would like to thank J. W. Bowden, M. A. Miller, A. Celovsky, J. M. Smeltzer, G. C. Longhurst, W. G. Newell, A. D. Lepage, J. F. Mecke, D. Phillips, J. R. Kelm, R. C. Stothers, and D. H. Rose for their technical help in the preparation, testing, and examination of the specimens. We would also like to acknowledge the services of CEA, Saclay, for the irradiation, especially those of Y. Bouilloux.

References

[1] Chow, C. K., Coleman, C. E., Hosbons, R. R., Davies, P. H., Griffiths, M., and Choubey, R., "Fracture Toughness of Irradiated Zr-2.5Nb Pressure Tubes from CANDU Reactors," *Zirconium in the Nuclear Industry: Ninth International Symposium, ASTM STP 1132,* 1991, pp. 245–275.

[2] Sagat, S., Coleman, C. E., Griffiths, M., and Wilkins, B. J. S., "The Effect of Fluence and Irradiation Temperature on Delayed Hydride Cracking in Zr-2.5Nb," *Zirconium in the Nuclear Industry: Tenth International Symposium ASTM STP 1245,* 1994, pp. 35–61.

[3] Davies, P. H., Hosbons, R. R., Griffiths, M., and Chow, C. K., "Correlation between Irradiated and Unirradiated Fracture Toughness of Zr-2.5Nb Pressure Tubes," *Zirconium in the Nuclear Industry: Tenth International Symposium, ASTM STP 1245,* American Society for Testing and Materials, 1995, pp. 135–167.

[4] Coleman, C., "Effect of Texture on Hydride Reorientation and Delayed Hydrogen Cracking in Cold-Worked Zr-2.5Nb," *Zirconium in the Nuclear Industry: Fifth International Symposium, ASTM STP 754,* American Society for Testing and Materials, 1982, pp. 393–411.

[5] Simpson, L. A., Chow, C. K., and Davies, P. H., "Standard Test Method for Fracture Toughness of CANDU Pressure Tubes," CANDU Owner's Group Report No. COG-89-110-1, AECL Research, September 1989.

[6] Griffiths, M., Winegar, J. E., Mecke, J. F., and Holt, R. A., "Determination of Dislocation Densities in HCP Metals using X-Ray Diffraction and Transmission Electron Microscopy," *Advances in X-ray Analysis,* Vol. 35, 1992, pp. 593–599 (issued as RC-776).

[7] Aitchison, L. and Davies, P. N., "Role of Microsegregation in Fracture of Cold-Worked Zr-2.5Nb Pressure Tubes," *Journal of Nuclear Materials,* Vol. 203, 1993, pp. 206–220.

[8] Davies, P. H., Aitchison, L., Himbeault, D. D., Järvine, A. K., and Watters, J. F., "On the Fracture of Cold-Worked Zr-2.5Nb Pressure Tubes Fabricated from 100% Recycled Material," *Special Canadian Edition of Fatigue and Fracture of Engineering Materials and Structures,* Vol. 18, 1995, pp. 789–800.

[9] Theaker, J. R., Choubey, R., Moan, G. D., Aldridge, S. A., Davis, L., Graham, R. A., and Coleman, C. E., "Fabrication of Zr-2.5Nb Pressure Tubes to Minimize the Harmful Effects of Trace Elements," *Zirconium in the Nuclear Industry: Tenth International Symposium, ASTM STP 1245,* American Society for Testing and Materials, 1994, pp. 221–242.

[10] Holt, R. A., Causey, A. R., Woo, C. H., Griffiths, M., Christodoulou, N., and Ho, E. T. C., "Non-Linear Deformation of Zr-Alloy Nuclear Reactor Core Components during Irradiation," *Zirconium*

in the Nuclear Industry: Eleventh International Symposium, ASTM STP 1295, American Society for Testing and Materials, 1996, pp 623–637 (issued as RC-1466).

[*11*] Holt, R. A., Causey, A. R., Griffiths, M., and Ho, E. T C., "High-Fluence Irradiation Growth in Cold-Worked Zr-2.5Nb," submitted to *Zirconium in the Nuclear Industry: Twelfth International Symposium*, Toronto, Canada, June 1998, this publication, pp. 86–104

[*12*] Griffiths, M., Mecke, J. F., and Winegar, J. E., "Evolution of Microstructure in Zirconium Alloys during Irradiation," *Zirconium in the Nuclear Industry· Eleventh International Symposium, ASTM STP 1295*, American Society for Testing and Materials, 1996, pp. 580–602.

[*13*] Cann, C. D., Sexton, E E., Duclos, A M., and Smith, G. G., "Effect of Decomposition of β-phase Zr-20%Nb on Hydrogen Partitioning with α-Zr," *Journal of Nuclear Materials*, Vol. 210, 1994, pp. 6–10.

DISCUSSION

B. Cox[1] (*written discussion*)—If you are getting tunneling in your fracture toughness specimens, are you getting some hardening of the surface by oxygen diffusion? Zr is a good getter for oxygen in Na/K, but, of course, any other oxygen-containing environment would give the same oxygen diffusion into the specimen.

R. R. Hosbons et al. (*author's closure*)—Tunneling occurs in both irradiated and unirradiated specimens. We do not believe oxygen has any effect on tunneling.

J. Harbottle[2] (*written discussion*)—You observe that ⟨c⟩ component dislocations only form in grains having radial texture. Have you been able to associate this result with any microstructural feature or change or with a decrease in the stacking fault energy?

M. Griffiths et al. (*authors' closure*)—TEM and XRD analyses indicated that the formation of ⟨c⟩ component dislocation loops was more pronounced in, but not restricted to, grains with a radial c-axis orientation. We believe that the reason for this is that there are more ⟨c⟩ component dislocation having screw orientations in grains with a radial c-axis orientation in the as-fabricated pressure tube, and the c-component dislocation loops form preferentially on these dislocations in a manner similar to helical climb. The preponderance of c-component dislocations in radial c-axis grains is the result of their orientation (being favorable oriented for c+a slip during the final cold working of the pressure tubes), and their morphology. Orientation mapping has shown that many of the large "prior alpha" grains that appear equiaxed when viewed down the axis of the tubes have c-axis close to radial orientations. We hypothesize that screw dislocations are more prevalent in these grains because there are fewer grain boundaries where they can be annihilated. The thin platelet grains tend to have their c-axis in the plane of the platelet and are mostly aligned in the transverse direction of the tubes; gliding c+a screw dislocations in these latter grains would soon encounter grain boundaries and would be annihilated.

K. L. Murty[3] (*written discussion*)—Can you comment on the crack orientation dependence of the fracture toughness and the effect of irradiation on it?

R. R. Hosbons et al. (*author's closure*)—In general, the fracture toughness in the circumferential direction is higher than in the axial direction. It is difficult to measure expect an initiation toughness because the crack runs out of plane.

J. Rashid[4] (*written discussion*)—Can you comment on the effect of residual stresses (as a result of flattening the specimens) on the fracture toughness?

R. R. Hosbons et al. (*author's closure*)—The fracture specimens were not flattened.

Young Suk Kim[5] (*written discussion*)—What is the expected delayed hydride crack growth rate, DHCV, at a fluence of 30×10^{25} $n \cdot m^{-2}$? What is the reason for using dJ/da as a measurement of the fracture toughness?

R. R. Hosbons et al. (*author's closure*)—The predicted DHCV at a fluence of 30×10^{25} $n \cdot m^{-2}$ is 2.6×10^{-7} $m \cdot s^{-1}$. dJ/da is used as a fracture toughness measurement because it

[1] University of Toronto, Toronto, Ont., Canada.
[2] Stoller Nuclear Fuel, Bristol, UK.
[3] North Carolina State University, Raleigh, NC.
[4] ANATECH, San Diego, CA.
[5] KAERI, Taejon, Korea.

is a measure of the crack growth toughness and is more sensitive than initiation toughness to changes in properties.

B. Kammenzind[6] *(written discussion)*—You mentioned that one detrimental factor regarding the presence of β-Zr on DHC is the higher diffusion rate of hydrogen in β-Zr. Is hydrogen also more soluble in β-Zr filaments and do you have information on the solubility of hydrogen in β-Zr in equilibrium with hydride precipitates in the α-phase?

R. R. Hosbons et al. (authors' closure)—Reference *13* in the text addresses this question.

[6] Bettis Laboratory, West Mifflin, PA.

Glen M. McDougall,[1] Vincent F. Urbanic,[2] and Olav Aarrestad[3]

Studies of Zirconium Alloy Corrosion and Hydrogen Uptake During Irradiation

REFERENCE: McDougall, G M , Urbanic, V. F., and Aarrestad, O , **"Studies of Zirconium Alloy Corrosion and Hydrogen Uptake During Irradiation,"** *Zirconium in the Nuclear Industry: Twelfth International Symposium, ASTM STP 1354,* G. P. Sabol and G. D. Moan, Eds , American Society for Testing and Materials, West Conshohocken, PA, 2000, 756–772.

ABSTRACT: The in-reactor corrosion and hydrogen pickup of Zircaloy-2 and Zr-2.5Nb pressure tube materials are being studied in two test loops: a light water loop in the NRU research reactor, and a new heavy water loop in the Halden reactor. The complimentary test programs examine the corrosion behavior of small specimens as a function of fast neutron flux and fluence, temperature, water chemistry, and specimen pre-oxidation

In NRU tests conducted over a range of reducing conditions (20 to 60 cm^3 $H_2 \cdot kg^{-1}$) at 568 K, Zr-2.5Nb specimens bearing "thin" prefilm oxides ($\leq$6 μm) experience a reduction in oxidation rate influx. However, samples with thick prefilm oxides exhibit higher rates, suggesting that, like Zircaloy-2, rates for Zr-2.5Nb may increase as the oxide film continues to thicken.

Initial results from the Halden program (5 to 7 cm^3 $D_2 \cdot kg^{-1}$) show that prefilmed specimens from tubes made of β-quenched material exhibit lower oxidation and deuterium pickup rates than tubes made from non-β-quenched materials Prefilmed tubes made from β-quenched material also pickup a lower percentage of the D generated by the corrosion reaction. At high flux levels, prefilmed specimens from tube made of both materials exhibit a narrow range of percentage pickup values (4 to 5%), irrespective of temperature. A preliminary examination of activation energies over the range 523 to 598 K suggests significant differences in the temperature dependencies for oxidation and deuterium pickup of prefilmed specimens of tubes made from β and non-β-quenched Zr-2.5Nb The differences are correlated with fast flux level

KEYWORDS: corrosion, irradiation, temperature, water chemistry, pre-oxidation, Zircaloy-2, Zr-2 5Nb, zirconium oxide, β quenching, deuterium pickup

In CANDU reactors, the lithiated heavy water coolant reacts with the inside surfaces of Zr-2.5Nb pressure tubes to form a zirconium oxide film and deuterium. A fraction of the deuterium generated by the corrosion reaction finds its way into the pressure tube. The key variables influencing the corrosion and deuterium uptake of pressure tubes are fast neutron flux and fluence, temperature, water chemistry, and oxide film thickness. Material variability (primarily differences in the as-fabricated microstructure and/or micro-chemistry of the tube) may also contribute to observed differences in behavior. While surveillance data are the logical choice for validating a mathematical model of corrosion and deuterium ingress, such data do not lend themselves to development of a model because of simultaneous variations in the key parameters along the length of the tube. Further, any dependencies that can be extracted from pressure tube data are not applicable to operating conditions beyond those to

[1] Scientist and [2] branch manager, respectively, AECL, Chalk River Laboratories, Chalk River, Ontario K0J 1J0, Canada.
[3] Division head, OECD Halden Reactor Project, P.O. Box 173, N-1751 Halden, Norway.

which the surveillance tubes were exposed. Therefore, to develop a capability for predicting corrosion and deuterium uptake along pressure tubes in both current and future reactor designs, these parameters must be evaluated independently and the various dependencies incorporated into a mathematical model of corrosion and deuterium ingress. To evaluate these parameters, experiments are in progress in two high-temperature, high-pressure loops: a light water loop in the NRU research reactor at Chalk River,[3] and a new heavy water loop in the Halden Boiling Water Reactor.[4] Both test programs involve in- and out-of-flux exposures of cold-worked Zr-2.5Nb and cold-worked Zircaloy-2 pressure tube materials. Cold-worked Zr-2.5Nb has a two-phase microstructure consisting of elongated α-Zr grains surrounding by a network of β-Zr. Zircaloy-2 has a single-phase microstructure, with α-Zr grains containing a low-volume fraction of second-phase intermetallic particles.

Experimental Procedure

Small specimens of pressure tube material are being irradiated in the U2 loop of the NRU reactor and in Loop 9 of the Halden reactor. The effects of fast neutron fluence, water chemistry, and specimen pre-oxidation are being studied in the light water U2 loop. Investigations of temperature and fast flux effects under CANDU chemistry conditions are underway in the Halden loop.

In the U2 experiments, small specimens (60 by 10 by 1 mm) are simultaneously exposed in a materials test bundle (MTB), and an out-of-flux position in the loop. For MTB tests, specimens are attached to holders inside hollow dummy fuel elements. They typically experience a fast neutron flux of $\sim 4.5 \times 10^{17}$ n · m^{-2} · s^{-1} ($E \geq 1.05$ MeV) at a temperature of 568 K. This approximates the temperature near the outlet end of a CANDU pressure tube. During each phase of testing, dissolved hydrogen and oxygen levels are monitored continuously using on-line Orbisphere gas analyzers and maintained according to the desired specifications for the particular test. Using an ion exchange column (resin in the hydroxide form), lithium additions are made as required to maintain a pH of 10 to 10.5 during all tests.

Specimens were prepared from a number of Zircaloy-2 and Zr-2.5Nb pressure tubes and tested in both pickled and pre-filmed conditions. Table 1 summarizes the fabrication data for the tubes and Table 2 the ingot composition specifications. The material condition for both alloys was that produced by the respective pressure tube fabrication process. The fabrication route for Zr-2.5Nb tubes involves hot extrusion at 1090 K and cold drawing 20 to 30%; with the exception of Tube H1831, a 24-h stress relief treatment (673 K light water steam) completed the fabrication process. Zircaloy-2 tubes were fabricated by a similar process.[5] Specimens from several Zircaloy-2 and Zr-2.5Nb tubes were pre-oxidized in 673 K heavy water steam. Exposure periods between 1 and 440 days were required to produce the desired range of oxide thicknesses. It has been recognized that this may not be the optimum prefilming treatment for Zr-2.5Nb because of the potential for microstructural changes to occur during the treatment [2]. It is believed that when prefilmed specimens are subsequently tested, these changes may result in persistence of an oxidation rate (and perhaps, a hydrogen pickup-rate) more characteristic of the prefilming temperature than of the test temperature.

[3] AECL, Chalk River Laboratories, Chalk River, Ontario, Canada.

[4] Institutt for energiteknikk, OECD Halden Reactor Project, Halden, Norway.

[5] Details of the fabrication route for Zr-2.5Nb pressure tubes have been reported elsewhere [*1*]. The route for producing (earlier) Zircaloy-2 tubes differed in the following ways: (1) lower forging and extrusion temperatures were used; (2) the extent of cold drawing was only 15 to 20%; and (3) the final stress relief period was 72 h.

TABLE 1—*Summary of fabrication data for Zr-2.5Nb and Zircaloy-2 pressure tubes.*

Tube Number	Alloy	Ingot Fabrication	
		TWCA,[a] heat no.	Beta Solution Anneal
		NRU Tests	
669	Zr-2.5Nb	377461	no
1980	Zr-2.5Nb	390597R	no
B381	Zr-2.5Nb	396221	no
C148	Zr-2.5Nb	396726	no
H1831	Zr-2.5Nb	213975Q	yes
693	Zircaloy-2	373854Q	yes
841	Zircaloy-2	374727Q	yes
XA032	Zircaloy-2	207682Q	yes
		Halden Tests	
669	Zr-2 5Nb	377461	no
B439	Zr-2 5Nb	396331	no
RX095	Zr-2.5Nb	233626Q	yes
W061	Zr-2.5Nb	230871Q	yes
Y321	Zr-2.5Nb	228391Q	yes

[a] Teledyne Wah Chang, Albany, NY.

As a result, initial oxidation and pickup rates for prefilmed specimens were corrected for this memory effect. In each phase of the U2 loop tests, two sets of specimens were exposed for an initial 70-day period. This served to condition the pre-oxidized specimens, minimizing any memory effect resulting from the 673 K steam treatment. After the first loop cycle, weight gains were measured on all specimens and representative hydrogen pickup data collected by destructive analysis of one set. The remaining specimens were returned to the loop for a second and third cycle, each of about 70 days duration. To correct for the pre-oxidation memory effect, the initial set of oxidation and hydrogen pickup rates for the latter specimens were determined between the first and second 70-day cycles.

The Halden heavy water loop consists of parallel zirconium alloy in-flux assemblies (IFAs) connected to a stainless steel out-of-core loop system. The tests reported here were performed in two IFAs: one operated at a low flux (peak = 2.1×10^{17} n · m^{-2} · s^{-1}, $E \geq 1.05$ MeV), the other at a higher flux (peak = 4.9×10^{17} n · m^{-2} · s^{-1}, $E \geq 1.05$ MeV). Inside each IFA, a cluster of fuel rods is arranged around a pair of vertical tests channels operated at 523 and 598 K, respectively. The flow rate along each test channel results in an in-pile residence time comparable to a CANDU fuel channel. To eliminate boiling along the high-temperature channels, coolant pressure is maintained at 15.5 MPa. In addition to the in-flux assemblies, loop coolant is also supplied to two out-of-flux autoclaves operated at 523 and 598 K.

While the loop is designed to accommodate a wide range of water chemistries, the Halden tests are being performed under conditions typical of a CANDU reactor A pH[6] of 10.2 to 10.8 is maintained by lithium additions (ion exchange resin in the deuteroxide form). The

[6] For the Halden tests, hydrogen ion activities are reported as $pH_{a,RT}$, the *apparent, room temperature* value, i.e., the value measured in a heavy water solution using a pH electrode calibrated in light water buffers at the same temperature

TABLE 2—*Chemical composition specifications for Zr-2.5Nb and Zircaloy-2 ingots used to prepare pressure tubes*

Alloying Element	Zr-2.5Nb[a]	Zr-2 5Nb[b]	Zircaloy-2[c]
	Range, weight %		
Cr	...[d]	...[d]	0 05–0.15
Fe	...[d]	...[d]	0 07–0 20
Nb	2 40–2.80	2 5–2 8	...[d]
Ni	...[d]	...[d]	0 03–0 08
Fe+Cr+Ni	...[e]	...[e]	0.18–0 38
O	0 09–0 13	0.10–0 13	0.09–0.14
Sn	...[d]	...[d]	1.20–1 70
Zr	balance	balance	balance
Impurity Element	Maximum, ppm, wt		
Al	75	75	75
B	0 5	0.5	0 5
C	270	125	270
Cd	0.5	0 5	0.5
Co	20	20	20
Cr	200	100	...[f]
Cu	50	50	50
Fe	1500	650	...[f]
H	25	5	25
Hf	50	50	50
Mg	20	20	20
Mn	50	50	50
Mo	50	50	50
N	65	65	65
Ni	70	35	...[f]
P	[e]	12	[e]
Pb	130	50	130
Si	120	120	200
Sn	100	100	...[f]
Ta	200	100	200
Ti	50	50	50
U	3.5	3 5	3.5
V	50	50	50
W	100	50	100

[a] For ingots 377461, 390597R, 396221, 396726, 213975Q, and 396331.
[b] For ingots 233626Q, 230871Q, and 228391Q.
[c] All Zircaloy-2 ingots listed in Table 1.
[d] Impurity element.
[e] Not included in specification.
[f] Alloying element.

same water chemistry conditions are provided at the inlets to all test channels. Both inlet and outlet coolant streams from each channel are routinely analyzed, both by continuous on-line instrumentation and by periodic grab sampling. Dissolved deuterium and oxygen concentrations are monitored using on-line Orbisphere gas analyzers and maintained at 5 to 7 $cm^3 \cdot kg^{-1}$ and <5 $\mu g \cdot kg^{-1}$, respectively.

Identical sets of small specimens (30 by 10 by 1 mm) occupy holders inside each test channel. These include Zircaloy-2 and Zr-2.5Nb pressure tube materials in both pickled and

prefilmed conditions The latter tubes are representative of those operating in all current CANDU reactors. A portion of the specimens were pre-oxidized for 24 h in 673 K light water steam

At the conclusion of each Halden reactor year (nominally 185 days), all specimens are ultrasonically cleaned and weighed. Selected specimens are removed for destructive examination To date, examinations have been completed only on those specimens removed after the first 185-day exposure. Since only one set of weight gain/deuterium pickup data exists, it is not yet possible to correct the prefilmed specimen results for memory effects. Differential oxidation and pickup rates will be calculated once the second set of samples (removed after 370 days) has been analyzed. The planned duration of the Halden test program is five years.

Prior to post-irradiation examination, NRU specimens were decrudded in a room temperature bath of 50% (vol/vol) hydrochloric acid (HCl) for 12 h. Halden specimens were decrudded in the same bath, but at 333 K for 4 h. Oxidation rates for both sets of specimens were determined from weight gain measurements to the nearest 0.01 mg. Both hydrogen (NRU specimens) and deuterium concentrations (Halden specimens) were determined by hot vacuum extraction mass spectrometry.

Results and Discussion

Effect of Prefilm Oxide Thickness

One approach to predicting the long-term behavior of pressure tubes is to measure the corrosion behavior of specimens bearing thick prefilm oxides Following the practice established in earlier tests [2], pre-oxidation treatments were carried out in 673 K steam While it is recognized that the resulting oxide layers may not simulate all properties of reactor-grown films, the thermal treatment does result in some decomposition of the β-Zr network in the underlying alloy. This decomposition is observed in pressure tubes operated in power reactors and is believed to contribute to the in-reactor corrosion behavior of Zr-2.5Nb [3].

Continuing the work during earlier phases of the U2 loop test program [2], two new phases have now been completed. Phase III was operated with a dissolved hydrogen level of 20 to 30 $cm^3 \cdot kg^{-1}$; during the Phase IV test, a level of 40 to 60 $cm^3 \cdot kg^{-1}$ was maintained. Both tests involved exposure of groups of prefilmed specimens for two periods: one group for about 70 days, and a second for a total of about 210 days. During the first 70-day exposure, the specimens were conditioned to the test temperature and particular water chemistry under investigation. Based on results of other tests (specimens pre-oxidized in 763 K steam, then conditioned in 568 K water), it appears that the 70-day conditioning period was sufficient to eliminate any memory effects associated with the earlier 673 K treatment. All specimens were removed from the test after 70 days of exposure and a first set of weight gain data collected. One group of specimens was then set aside for subsequent examination. Following a second 70-day exposure, the remaining specimens were removed for examination and the oxidation rates between 70 and 140 days determined from the two sets of measurements. After a third exposure, the specimens were again measured and a second set of oxidation rates calculated between 140 and 210 days. It was assumed that these rates would represent oxidation rates for pressure tubes bearing oxides characteristic of varying periods of service under the specific chemistry conditions of the tests.

A comparison of the results for bare (pickled only) and prefilmed Zr-2.5Nb specimens is shown in Fig. 1. The derived oxidation rates are the average for pairs of individual specimens, with the range of data shown as a bar. Where no vertical bar exists, the range of data lies within the size of symbol used. When oxides are thin (less than ~ 6 μm), irradiated specimens exhibit a suppressed corrosion rate. This effect is attributed to microstructural change

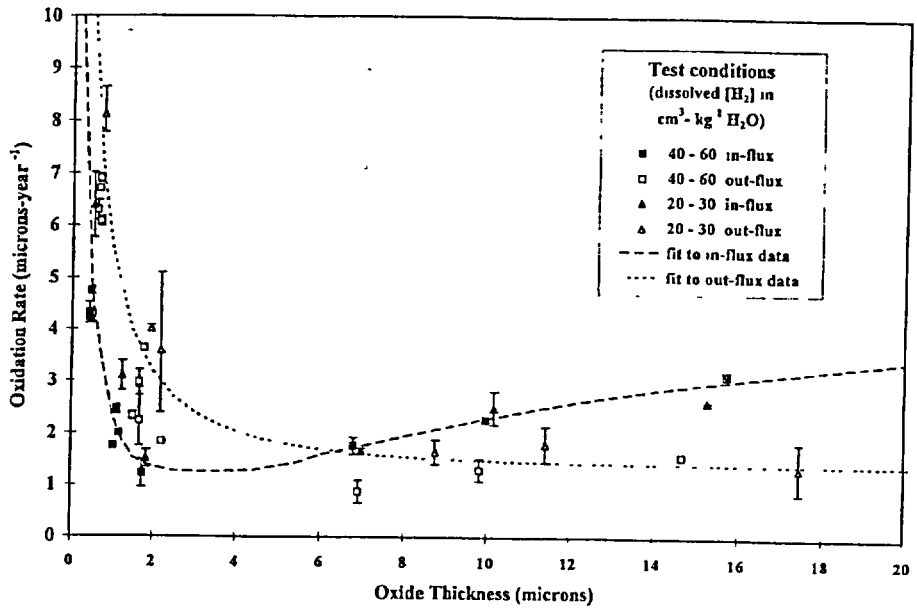

FIG. 1—*Oxidation rate of bare and prefilmed Zr-2.5Nb pressure tube specimens in 568 K water in the U2 loop of NRU.*

in the base alloy induced by the flux of fast neutrons, as reported previously [*3*]. However, as the oxide thickens, in-flux specimens experience an increased corrosion rate relative to their out-of-flux counterparts. At present, the reasons for this are unclear, but may involve a combination of the following phenomena: (1) saturation of the microstructural changes responsible for the earlier suppression of corrosion; (2) development of oxide porosity allowing for lithium accumulation (and, consequently, accelerated rates of corrosion [*4*]); and, (3) the establishment of unique coolant chemistry in such pores, potentially supporting the onset of radiolysis at or near the metal-oxide interface [*5*].

As shown in Fig. 2, different behavior is observed for Zircaloy-2 from the same tests. When exposed either in- or out-of-flux, coupons bearing very thin oxides (less than ~3 μm) experience a rapidly decreasing oxidation rate; however, over this thickness range, rates for in-flux coupons are always higher. As the oxide thickens, out-of-flux coupons show only a small increase in oxidation rate, while the corresponding in-flux specimens undergo a substantial increase in oxidation rate up to a thickness of ~15 μm. Beyond a prefilm thickness of 20 μm, some of the observed variability in oxidation data may be attributed to microspalling. This problem may be related to the choice of pre-oxidation conditions used to produce oxides of this thickness. For this reason, new pre-oxidation methods are being explored.

Effect of β Quenching

Of the Zr-2.5Nb pressure tubes used to prepare Halden specimens, four were made from material water quenched from the β-phase field prior to extrusion. For comparison, specimens were also prepared from three tubes made from material that was air-cooled, rather than

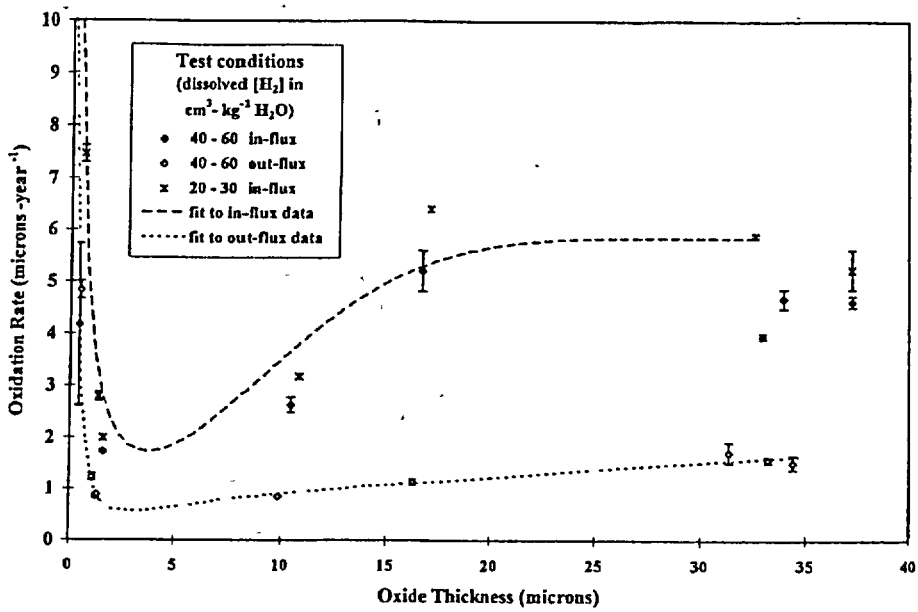

FIG 2—*Oxidation rate of bare and prefilmed Zircaloy-2 pressure tube specimens in 568 K water in the U2 loop of NRU.*

quenched from the β-phase field. While earlier CANDU reactors (for example, Pickering A NGS) utilized tubes made from non-β-quenched material, newer units (for example, Wolsung 1) use exclusively tubes made from β-quenched material.

Figure 3 depicts oxidation rates for two sets of prefilmed specimens after 185 days. The first set was prepared from two pressure tubes made from non-β-quenched material; the second set was from three tubes made of β-quenched material. Each data point represents a single specimen. Up to $\sim 2 \times 10^{17}$ n · m^2 · s^{-1} specimens made from non-β-quenched materials show a suppression of corrosion rate at 523 K and an enhancement at 598 K. As flux is increased beyond this value, materials tested at 523 K show a slight decrease in oxidation rate, while there is (in general) no change in rate at 598 K. In contrast, at 523 K, specimens made from β-quenched materials show a small increase in corrosion rate with increasing flux; at high flux levels, results for tubes made from β and non-β-quenched material are practically indistinguishable. As observed in 598 K tests of specimens from tubes made of non-β-quenched material, increases in fast flux over the range 2 to 4.6×10^{17} n · m^2 · s^{-1} appear only to narrow the range of corrosion rates for specimens from tubes of β-quenched material. Importantly, at a temperature (523 K) and flux similar to the region near a pressure tube inlet, specimens from tubes made of β-quenched material exhibit lower oxidation rates than those from tubes of non-β-quenched material. At 598 K, and for flux values experienced between the mid-channel and outlet locations in a CANDU pressure tube, tubes made from β-quenched material also show lower corrosion rates. Finally, while at 523 K there is a significant separation between out-of-flux rates for specimens from tubes made of β and non-β-quenched materials; the respective data sets overlap at 598 K. This has important implications for modeling the corrosion behavior at the ends of pressure tubes in CANDU fuel channels, where flux levels decrease rapidly.

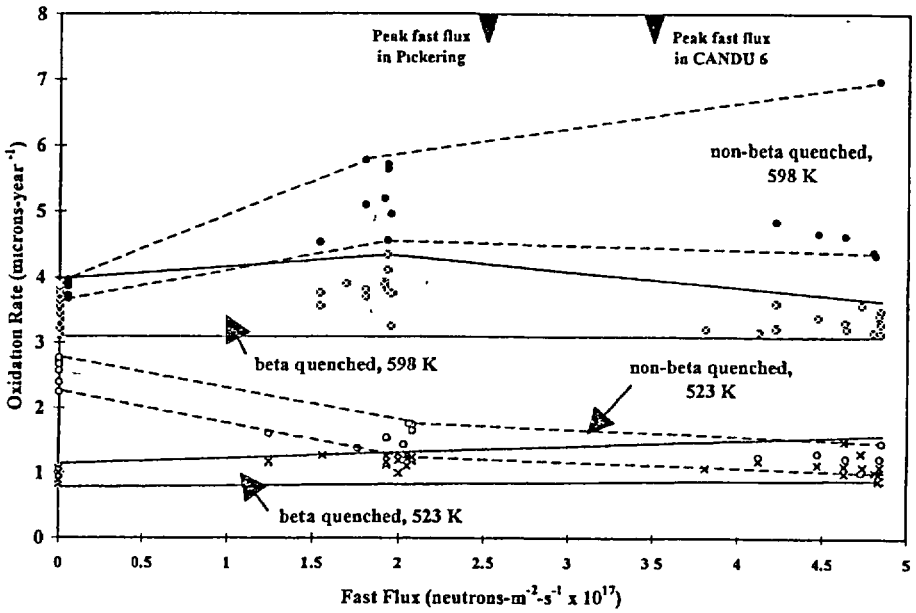

FIG. 3—*Oxidation rate of prefilmed Zr-2 5Nb pressure tube specimens in 523 and 598 K heavy water in Halden. The markers along the upper axis indicate the peak fast flux in two CANDU reactors*

Figure 4 summarizes deuterium pickup rates for a subset of the specimens described above. Each data point represents the average of two analyses of a single specimen. The figure demonstrates several interesting points. First, regardless of the processing route for the material from which the pressure tube was made, or the test temperature, deuterium uptake is always higher for the in-flux specimens that their out-of-flux counterparts. Second, analogous to the situation for oxidation, tubes made from β-quenched material showed significantly lower pickup rates at both 523 and 598 K over the complete range of fast flux studied. It should be noted that for tubes made of non-β-quenched material, there is an interesting parallel between the flux dependencies for pickup rate and oxidation rate, i.e., at both temperatures the rates tend to saturate at a flux of $\sim 2 \times 10^{17}$ n · m^2 · s^{-1}. However, the lack of data at fluxes immediately below this level makes if difficult to determine where the saturation occurs. In any event, while oxidation rates for specimens made from tubes of non-β-quenched material show the opposite flux dependence between 0 and $\sim 2 \times 10^{17}$ n · m^2 · s^{-1} (decreasing at 523 K, increasing at 598 K), deuterium pickup rates increase at both temperatures. For fluxes beyond this level, specimens made from tubes of non-β-quenched material assume a constant pickup rate at either temperature, the same trend observed for oxidation rates.

Among the specimens tested in Phase IV of the U2 program, a number were prepared from a pressure tube made of non-β-quenched material (No 669). Specimens from this tube were also tested in Halden. While the dissolved hydrogen level in the two tests differed significantly (40 to 60 cm^3 H_2 · kg^{-1} in U2 loop versus 5 to 7 cm^3 D_2 · kg^{-1} in Halden), both conditions are reducing. Thus, some comparisons may be warranted. Figure 5 summarizes oxidation rates for prefilmed coupons of Tube 669 in the two tests as a function of fast flux. Examining the in- and out-of-flux results for exposures at 523 K (Halden loop)

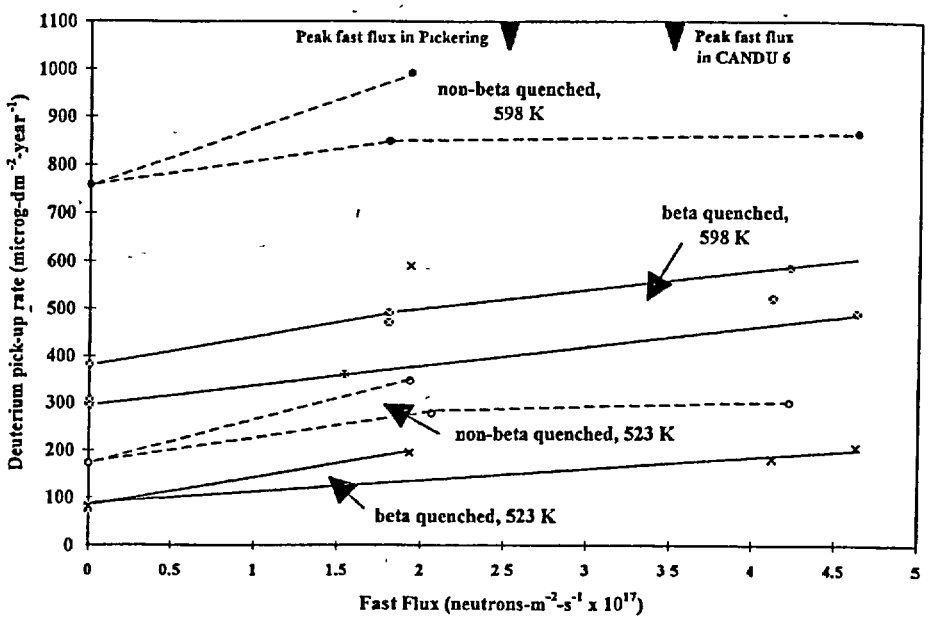

FIG 4—*Deuterium pickup rate of prefilmed Zr-2.5Nb pressure tube specimens in 523 and 598 K heavy water in Halden. The markers along the upper axis indicate the peak fast flux in two CANDU reactors*

and 568 K (U2 loop), it is clear that both sets of samples exhibit a suppression of corrosion rate with increasing flux, although the lack of low flux data at 568 K precludes any meaningful comparison of the form of the respective flux dependencies. There are two plausible explanations for overlap in oxidation rates for out-of-flux specimens at 568 and 598 K. First, the latter (Halden) specimens had a greater average prefilm thickness (0 54 versus 0.20 μm) than the U2 specimens; differences in the initial surface finish of each set may have resulted in a differing oxidation rate during prefilming A shown in Fig. 1, oxidation rate decreases rapidly with increasing oxide thickness. Thus, it would not be unreasonable that over the course of a short-term test, specimens bearing a thin prefilm oxide would exhibit a corrosion rate approaching that for specimens bearing a thicker prefilm oxide, but tested at a higher temperature. Second, while the out-of-flux autoclaves in the Halden loop have independent temperature controls, out-of-flux samples in U2 tests are suspended in the coolant stream emerging from the in-flux portion of the loop Thus, while in-flux specimens experience a temperature of 568 K, estimates have placed the out-of-flux specimen temperature as high as 579 K. Coupled with the possible influence of thin prefilm oxides, this size of temperature difference could easily explain the corrosion rates exhibited by out-of-flux Phase IV specimens.

The results in Fig. 5 imply that any temperature "threshold" (above which one would observe an enhancement of corrosion with increasing flux) must lie between 568 and 598 K. This has important implications for understanding the performance of early CANDU reactors, which utilized (primarily) non-β-quenched pressure tubes and operated with outlet temperatures in the range 568 to 578 K. To the extent that reducing chemistry was maintained in units with an outlet temperature of 568 K, the present data suggest that corrosion rates

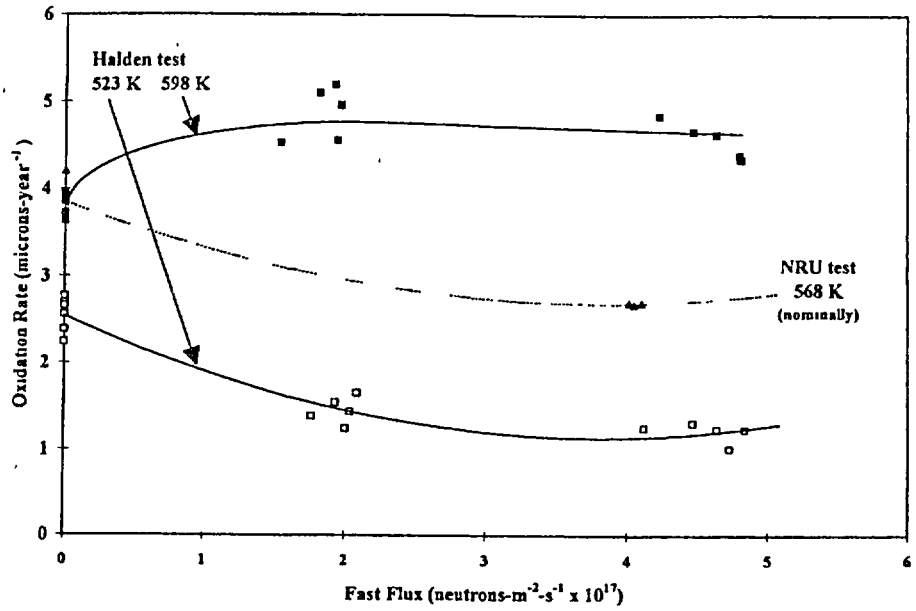

FIG 5—*Oxidation rate of prefilmed Zr-2.5Nb pressure tube specimens in 523 and 598 K heavy water (Halden) and 568 K light water (U2 loop). All specimens are from the same pressure tube.*

were suppressed over the entire length of the pressure tubes, at least early in life. Additional work will be required to establish the flux dependence of oxidation rate between 568 and 598 K.

Hydrogen/Deuterium Uptake

Table 3 compares the percentage uptake data for pickled specimens of Zr-2.5Nb exposed in the Phase IV test in the U2 loop, with estimates for the corresponding specimens in Halden. The U2 loop data (568 K exposures) are based on hydrogen pickup. For each specimen, pickup was calculated by difference, i.e., the average of two post-irradiation measurements less the average for two archived samples of the same specimen. The tabulated

TABLE 3—*Comparison of the percentage theoretical uptake for bare Zr-2.5Nb specimens exposed in heavy water (Halden) and in light water (U2 loop). All data are for exposures at a fast neutron flux of 4.4 × 10^{17} n·m^{-2}·s^{-1}.*

		Theoretical Uptake, percent		
Source Material for Pressure Tube	Temperature Test	523 K Halden	568 K NRU	598 K Halden
Non-β quenched	..	17.3	9 8–10 1	6.7
β quenched	..	13.5	9 9	7 0

TABLE 4—*Comparison of the percentage theoretical uptake of deuterium for prefilmed Zr-2 5Nb specimens exposed in heavy water in Halden.*

Source Material for Pressure Tube	Temperature, K Fast Flux[a]	Theoretical Deuterium Uptake, percent					
		523			598		
		Zero	Low	High	Zero	Low	High
Non-β quenched	..	1.9	4 4–7.9	5 1	5 6	4.8–5 0	4.7
β quenched	..	2 7–3 1	4.4–11.8	4 3–4.7	2 5–2 8	2.6–3.8	4.1–4.9

[a] Fast flux ranges ($E \geq 1\ 05$ MeV). low = 1 54 to 1.93 × 10^{17} n · m² · s⁻¹; high = 4 12 to 4 63 × 10^{17} n · m² · s⁻¹.

values represent the average for at least two specimens. Since few Halden specimens were exposed at the same fast flux as the Phase IV MTB (average = 4 4 × 10^{17} n · m² · s⁻¹), pickup values were interpolated from graphs showing the flux dependence of deuterium pickup for specimens tested at 523 and 598 K.

On the basis of Table 3, two observations can be made. First, despite differing levels of dissolved hydrogen in the Halden and NRU tests (5 to 7 cm³ D_2 · kg⁻¹ and 40 to 60 cm³ H_2 · kg⁻¹, respectively), the percentage uptake for specimens from tubes of a given material show a consistent trend Comparing specimens from tubes made of β and non-β-quenched materials, values for the 568 K NRU test are bracketed by the 523 and 598 K Halden data. This implies a smooth decline in percentage uptake over the temperature range 523 and 598 K. Second, while tests at 523 K reveal some difference in percentage pickup between specimens made form tubes of β and non-β-quenched materials, very similar pickup values are observed for specimens from tubes of either type when exposed at each of two higher temperatures—568 K in NRU (9.8 to 10.1%) and 598 K in Halden (6.7 to 7%).

By way of comparison, Table 4 summarizes the range of percentage uptake values observed for prefilmed Halden specimens. The values represent the respective ranges for two non-β-quenched and three β-quenched tubes. In out-of-flux tests, while percentage pickup values for β-quenched materials tested at 523 K practically overlap with the corresponding 598 K data, there is a substantial separation between the low- and high-temperature results for non-β-quenched tubes. When tested in-flux, 523 K β-quenched samples display a slightly higher pickup value that their 598 K counterparts, at least until higher fluxes are reached. (Note that a low flux result of 11.8% is the average for two specimens exposed under identical conditions.[7]) For non-β-quenched tubes, fewer specimens were removed for examination; of the specimens that were, the majority of the reported results are for a single tube. As such, it may be premature to infer any trends, in particular for specimens exposed at 523 K (where considerable variation was observed among low-flux specimens). At 598 K, the available data from non-β-quenched tubes suggest a linear decrease in percentage uptake with increasing flux. Consistent with the results for specimens of β-quenched material, the gap between 523 and 598 K data for specimens of non-β-material tends to decrease with increasing flux. At high flux levels (>4 × 10^{17} n · m² · s⁻¹), percentage uptake values for specimens from both types of tubes fall within a narrow range (4.1 to 5.1%) irrespective of temperature. This is in contrast to the behavior of bare specimens exposed at a high flux value, shown in Table 3. At 568 and 598 K, specimens for both β and non-β-quenched

[7] The individual pickup values were 4.2 and 19.4%. We have no explanation for the latter value.

material exhibit very consistent percentage uptake values, but only at the respective test temperatures.

Temperature Dependence of Oxidation and Deuterium Uptake

Oxidation rates for specimens exposed at 523 and 598 K in Halden may include memory effects stemming from the 673 K pre-oxidation treatment. Since the magnitude and/or duration of this effect may be influenced by microstructure, contributions to the weight gain data for sets of specimens prepared from different pressure tubes could likewise vary. Thus, some uncertainty in the data for prefilmed specimens must be acknowledged.

As a result, a precise determination of the oxidation kinetics must await destructive examination of specimens removed after 370 days. However, for purposes of a qualitative comparison of the temperature dependence of oxidation for various specimens, average rates were calculated based on weight gains during testing. Arrhenius plots were constructed using the rates for specimens from tubes made of β and non-β-quenched material, exposed out-of-flux and under low- and high-flux conditions (defined in Table 4) The oxidation rate, S (in μm per year), can then be expressed as:

$$S = A \exp(-E_a/RT) \tag{1}$$

where A = pre-exponential factor in $\mu m \cdot yr^{-1}$, E_a = activation energy in $J \cdot mol^{-1}$, R = $8.314\ J \cdot K^{-1} \cdot mol^{-1}$, and T = temperature in K. Figure 6 summarizes the average activation energies for two sets of specimens, one prepared from three tubes of β-quenched material and the other set from two tubes made from non-β-quenched material. Values for specimens from tubes made of β-quenched material are relatively independent of flux, except for values ($>4.1 \times 10^{17}\ n \cdot m^2 \cdot s^{-1}$) that exceed the peak in CANDU reactors. In contrast, specimens from tubes made of non-β-quenched material show a distinct increase in the activation energy for oxidation when influx. For irradiated specimens, the values for low- and high-flux exposures are quite similar; this is consistent with oxidation data shown in Fig. 3.

Figure 7 compares the activation energy for deuterium pickup by the same set of prefilmed specimens. For consistency with Fig. 6, average pickup rates were calculated Arrhenius plots were then used to derive the activation energies for exposures under different fast flux regimes. Figure 7 suggests that while activation energies for deuterium pickup by specimens from tubes of β and non-β-quenched material are quite similar at zero and high flux, there is a distinct difference for exposures at low flux. This may have important implications for CANDU reactors, as the peak flux levels experienced by pressure tubes (2.5 to 3.5×10^{17} $n \cdot m^2 \cdot s^{-1}$) are bracketed by the Halden "low" and "high" flux datasets.

Finally, a comparison was made of the temperature dependence for oxidation for prefilmed Zr-2.5Nb specimens (Tube 669) exposed both in the Halden and U2 loops. Average weight gains were calculated for Halden specimens exposed out of flux and influx (4.2 to $4.7 \times 10^{17}\ n \cdot m^2 \cdot s^{-1}$) at 523 and 598 K, and for Phase IV U2 specimens exposed out of flux and influx ($4.1 \times 10^{17}\ n \cdot m^2 \cdot s^{-1}$) at 568 K. Figure 8 shows the average oxidation rates as a function of temperature for specimens from the Halden (185 day) and U2 (161 day) tests. The range of data is shown as a bar; where no bar exists, the range lies within the size of the symbol used. Oxidation rates (S, in $\mu m \cdot year^{-1}$) were derived from linear regression fits to the respective data (terms as defined for Eq 1). These equations apply for relatively thin oxides (about 2 μm or less) and may be expected to change somewhat for thicker films. For the reasons cited earlier (thinner prefilm oxides and a potentially higher exposure temperature), the average oxidation rate for specimens tested out of flux in the U2 loop falls somewhat above the best fit line. However, the influx data suggest that in spite of differing levels

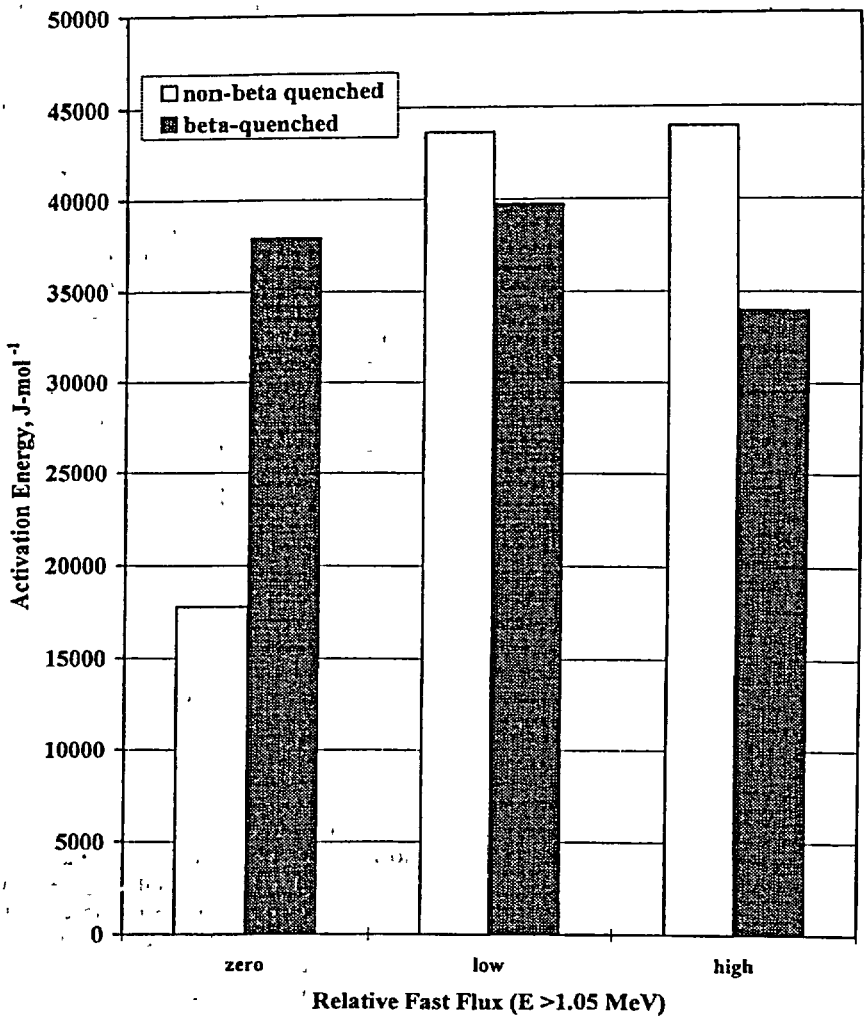

FIG. 6—*Activation energy for oxidation of prefilmed Zr-2.5Nb pressure tube specimens in 523 and 598 K heavy water in Halden*

of dissolved hydrogen, the oxidation behavior of specimens in the Halden and NRU Phase IV tests are quite consistent.

Summary

Complimentary in-reactor programs have been established to evaluate the influence of key variables on the corrosion of zirconium alloys. The programs are ongoing and will continue

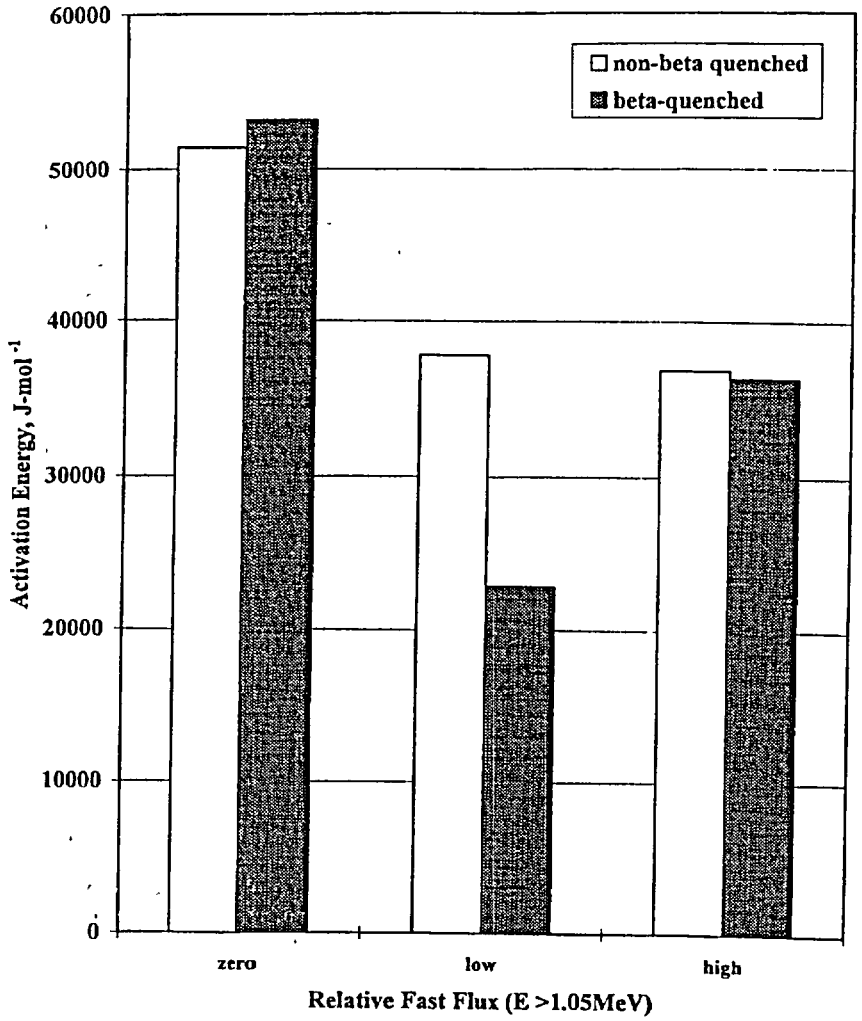

FIG. 7—*Activation energy for deuterium pickup of prefilmed Zr-2 5Nb pressure tube specimens in 523 and 598 K heavy water in Halden.*

to generate useful data in the future. On the basis of loop tests completed to date, the following observations can be made:

1. Up to an oxide thickness of ~6 μm, oxidation rates for Zr-2.5Nb are suppressed in-reactor relative to rates for out-of-flux specimens. As the oxide thickens, the in-reactor rate increases, eventually surpassing that for corresponding out-of-flux specimens The inference is that increased oxidation may occur in the long term.

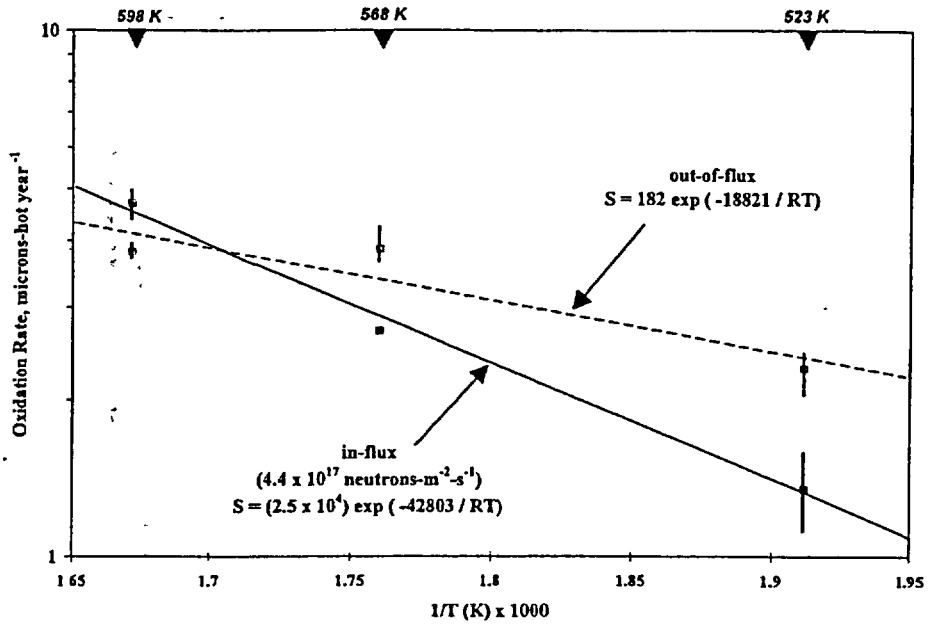

FIG 8—*Effect of temperature on the oxidation rate of prefilmed Zr-2.5Nb pressure tube specimens in 523 and 598 K heavy water (Halden) and 568 K light water (U2 loop) All specimens are from the same pressure tube. Activation energies are in J · mol⁻¹ and pre-exponential factors in microns · year⁻¹.*

2. Over the range of oxide thickness studied, in-reactor oxidation rates for Zircaloy-2 specimens consistently exceed those for corresponding out-of-flux specimens. Irradiated specimens experience a rapid increase in oxidation rate for oxide films in the range 5 to 15 μm

3. The above observations are valid over a broad range of water chemistry (20 to 60 cm^3 $H_2 \cdot kg^{-1}$), indicating that under reducing conditions, oxidation rates are not strongly dependent on the dissolved hydrogen concentration.

4. There is a pronounced influence of β quenching on the flux and temperature dependence of both oxidation and deuterium uptake of Zr-2.5Nb. At both 523 and 598 K, prefilmed specimens from pressure tubes made of β-quenched material show lower oxidation and deuterium pickup rates relative to those from tubes made of non-β-quenched material. Over the range of fast flux relevant to CANDU, prefilmed specimens from tubes made of β-quenched material exhibit a steady increase in percentage pickup as a function of flux; higher values are consistently observed at lower temperatures. In general, percentage pickup values for specimens from tubes of β-quenched material (2.5 to 5%) are lower than those from tubes made of non-β-quenched material (2 to 8%).

5. At high flux levels ($\geq 4 \times 10^{17}$ n · m^2 · s^{-1}), percentage pickup values for prefilmed specimens from tubes made of β and non-β-quenched materials fall within a narrow range (4 to 5%), irrespective of temperature. This convergence of percentage pickup values at high flux extends to bare specimens of β and non-β-quenched materials, but only when exposed at the same temperature (568 and 598 K).

6. A preliminary examination of the temperature dependencies for oxidation and deuterium pickup of Zr-2.5Nb pressure tube material suggests that the respective activation energies are strongly influenced by β quenching and the local fast flux level. Additional data will be required to confirm these results.

Acknowledgments

The authors gratefully acknowledge technical assistance from members of the Fuel Channel, the Health, Chemistry and Environment, and Nuclear Operations Divisions within AECL, and staff of the OECD Halden Reactor Project in obtaining the data presented in this paper. Valuable discussions with Dr. A. A. Bahurmuz are also acknowledged. The work presented herein was funded by the CANDU Owners Group (COG).

References

[1] Theaker, J. R., Choubey, R., Moan, G. D., Aldridge, S. A., Davis, L., Graham, R. A., and Coleman, C. E., "Fabrication of Zr-2 5Nb Pressure Tubes to Minimize the Harmful Effects of Trace Elements," *Zirconium in the Nuclear Industry: Tenth International Symposium, ASTM STP 1245*, A. M. Garde and E. R. Bradley, Eds., American Society for Testing and Materials, Philadelphia, 1994.

[2] Urbanic, V. F., Choubey, R., and Chow, C. K., "Investigation of Variables That Influence Corrosion of Zirconium Alloys During Irradiation," *Zirconium in the Nuclear Industry: Ninth International Symposium, ASTM STP 1132*, C. M. Eucken and A. M. Garde, Eds., American Society for Testing and Materials, Philadelphia, 1991.

[3] Urbanic, V. F. and Gilbert, R. W., "Effect of Microstructure on the Corrosion of Zr-2.5Nb Alloy," *IAEA Technical Committee Meeting on Fundamental Aspects of Corrosion of Zirconium Based Alloys*, Portland, Oregon, 1989.

[4] Ramasubramanian, N. and Balakrishnan, P. V., "Aqueous Chemistry of Lithium Hydroxide and Boric Acid and Corrosion of Zircaloy-4 and Zr-2.5Nb Alloys," *Zirconium in the Nuclear Industry: Tenth International Symposium, ASTM STP 1245*, A. M. Garde and E. R. Bradley, Eds., American Society for Testing and Materials, Philadelphia, 1994.

[5] Johnson, A. B., Jr., "Oxide Thickness Effects on Zircaloy Oxidation and Hydriding Under Irradiation," *Zirconium Alloy Oxidation and Hydriding Under Irradiation: Review of Pacific Northwest Laboratories' Test Program Results (Section 6), EPRI NP-5132*, Electric Power Research Institute, Palo Alto, CA, 1987.

DISCUSSION

Young Suk Kim[1] *(written discussion)*—What is the oxide thickness of the thin and thicker oxide described in the paper? Could you comment on why β-quenched Zr-2 5Nb had lower oxidation and hydrogen pickup compared to non-β-quenched Zr-2.5Nb?

G. McDougall (authors' closure)—Zr-2.5Nb and Zircaloy-2 materials were tested in both the bare and pre-filmed conditions. Specimens were pre-filmed to thickness spanning the following ranges: Zr-2.5Nb 0.2 to ~17 μm, and Zircaloy-2 0.8 to 37 μm At present we do not have a complete explanation for the observed differences in oxidation and deuterium pickup between the groups of β-quenched and non-β-quenched pressure tubes studied.

G. Sabol[2] *(written discussion)*—What was the effect of hydrogen over pressure, if any, on the theoretical hydrogen pickup?

G McDougall (authors' closure)—As yet, no H pickup data are available for tests operated at a single temperature but over a range of dissolved hydrogen concentrations. However, we have compared the percentage theoretical uptake values for bare Zr-2.5Nb specimens exposed in the U2 loop under a relatively high dissolved hydrogen concentration (40–60 cm^3 H_2 per kg H_2O) and under a lower concentration (5–7 cm^3 D_2 per kg D_2O) in the Halden loop. For specimens prepared from pressure tubes of β-quenched and non-β-quenched material, respectively, uptake values for specimens exposed at 568 K in the U2 loop are bracketed by values for similar specimens exposed at 523 and 598 K in Halden.

A. Motta[3] *(written discussion)*—In studying the effect of neutron flux on the hydrogen pickup rate, how do you separate the effect of the flux in increasing the hydrogen source term (by radiolysis) from the effect of the flux on the pickup process?

G. McDougall (authors' closure)—In the flux dependence studies performed at Halden, both in- and out-of-flux specimens were exposed to a single coolant stream containing a carefully controlled dissolved deuterium concentration. Reducing water chemistry was maintained at all times, resulting in dissolved oxygen levels of ≤ 5 $\mu g \cdot kg^{-1}$. This confirms that radiolysis was suppressed in the bulk coolant passing over the in-flux specimens. It is true that, on the basis of the U2 loop results (showing increasing oxidation rates for coupons bearing oxide films thicker than ~6 μm), we have extended A. B. Johnson's "thick film" hypothesis to Zr-2.5Nb. However, the maximum oxide thickness achieved by coupons in the Halden test was 3 μm, far below the threshold at which we postulate the presence of pores or cracks capable of supporting radiolysis independent of the bulk coolant chemistry. On this basis, we believe that the corrosion and deuterium pickup results (shown in Figs. 3 and 4) represent the response of the Zr-2.5Nb specimens only to imposed changes in fast flux, rather than any combined effect of fast flux and water chemistry variations in the bulk coolant or within pre-filmed oxides.

[1] KAERI, Taejon, Korea.
[2] Westinghouse, Pittsburgh, PA.
[3] Penn State University, University Park, PA.

Vincent, F. Urbanic[1] *and Malcolm Griffiths*[1]

Microstructural Aspects of Corrosion and Hydrogen Ingress in Zr-2.5Nb

REFERENCE: Urbanic, V. F. and Griffiths, M., **"Microstructural Aspects of Corrosion and Hydrogen Ingress in Zr-2.5Nb,"** *Zirconium in the Nuclear Industry: Twelfth International Symposium, ASTM STP 1354,* G. P. Sabol and G. D. Moan, Eds., American Society for Testing and Materials, West Conshohocken, PA, 2000, 641–657.

ABSTRACT: Zr-2.5Nb alloy pressure tubes for CANDU® reactors are nominally extruded at 815°C, cold-worked about 27%, and stress-relieved at 400°C for 24 h. The resulting structure consists of elongated α-Zr grains interspersed with a network of thin β-Zr filaments. Corrosion tests on unirradiated and preirradiated material have investigated the effects of microstructure and microchemistry on corrosion and hydrogen ingress. In two-phase (α-Zr+β-Zr) structures, the corrosion and hydrogen pickup increases with increasing volume fraction of β-Zr. Corrosion is highest for single β-phase material although hydrogen pickup reverts to a minimum value. Tests on alloys with low Nb concentration show that the optimum corrosion resistance occurs at a Nb content of about 0.1 wt% Nb. Thermal aging the metastable two-phase structure reduces corrosion and is consistent with a lower β-phase volume fraction and a lower concentration of Nb in the α-phase.

Cold working the as-extruded two-phase structure up to about 80%, prior to stress relieving, reduces the out-reactor corrosion by about a factor of two. However, in-reactor, the benefits of cold work are negligible since there is a suppression of corrosion in irradiated Zr-2.5Nb that dominates all other effects. Irradiation results in an increase in dislocation density due to dislocation loop formation and also enhances the progression to an equilibrium α-phase composition manifested by the appearance of Nb-rich precipitates. Both of these effects of irradiation on microstructure are associated with improved corrosion properties based on tests of materials with controlled microstructures and microchemistry. Any thermally induced decomposition of the α-phase, resulting from the stress-relief heat-treatment, is slowed or even reversed by irradiation, depending on flux and temperature, and is therefore unlikely to have a significant effect on corrosion of irradiated materials. One of the most important factors leading to improved corrosion properties in Zr-2.5Nb pressure tubing seems to be the precipitation of β-Nb particles and the concomitant reduction of Nb in the matrix of the α-Zr grains during irradiation. Apart from any direct effects of cold-working or dislocation loop formation, it is likely that increased dislocation densities will also enhance Nb precipitation.

KEYWORDS: microstructure, corrosion, Zr-Nb alloys, irradiation damage, diffusion

Zr-2.5 Nb pressure tubes for CANDU reactors are formed by extrusion at a temperature about 815°C. They are then cold-drawn about 27% to give a final tube length of 6.3 m with a final tube thickness of about 4.3 mm and an inside diameter of about 104 mm. The tubes contain a mixture of a- and c-component dislocations with densities of about 4×10^{14} m^{-2} and 1×10^{14} m^{-2}, respectively, and have a dual-phase alpha/beta structure. The alpha-phase grains are platelets (containing about 0.6 to 1 wt% Nb in solution) with aspect ratios of about 1, 10, and 40 in the radial, transverse, and longitudinal directions, respectively.

[1] Senior research scientists, Atomic Energy of Canada Limited, Chalk River Laboratories, Chalk River, Ontario K0J 1J0, Canada.

They are mostly oriented with prism $\{11\bar{2}0\}$ planes perpendicular to the radial direction, prism $\{10\bar{1}0\}$ planes perpendicular to the longitudinal direction, and basal (0001) planes perpendicular to the transverse direction. The α-grains are stacked together and separated by a nonequilibrium β-phase containing about 20 wt% Nb. A final autoclaving treatment results in partial decomposition of the β-phase with the formation of Nb-depleted ω precipitates in a Nb-enriched matrix (up to about 50 wt%); the average composition in the β-phase remains at about 20 wt%. The β-phase itself has a characteristic texture with (200) planes oriented perpendicular to the radial direction and the (110) planes oriented perpendicular to the longitudinal and transverse directions. The width of the beta phase in the radial direction is about one-tenth that of the alpha base. The width of the alpha phase is typically about 0.3 μm at the end of the tube corresponding with the back end of the extrusion and 0.5 μm at the end of the tube corresponding with the front end of the extrusion. The grain size varies along the length of the tubes because the tubes cool during the extrusion process so that the front end is extruded at a higher temperature compared with the back end, thus affecting the final grain size. A typical microstructure is illustrated in Fig 1.

Previous work has shown that corrosion of Zr-2.5Nb can be very sensitive to microstructure [*1*] and that the corrosion of resistance Zr-2.5Nb improves with irradiation [*1–3*]. This improvement has been attributed to changes in the microstructure that occur during irradiation [*4*]. The aim of the current work is to investigate in more detail the relationship between the as-fabricated microstructure and the impact of its evolution during irradiation on subsequent corrosion and deuterium ingress.

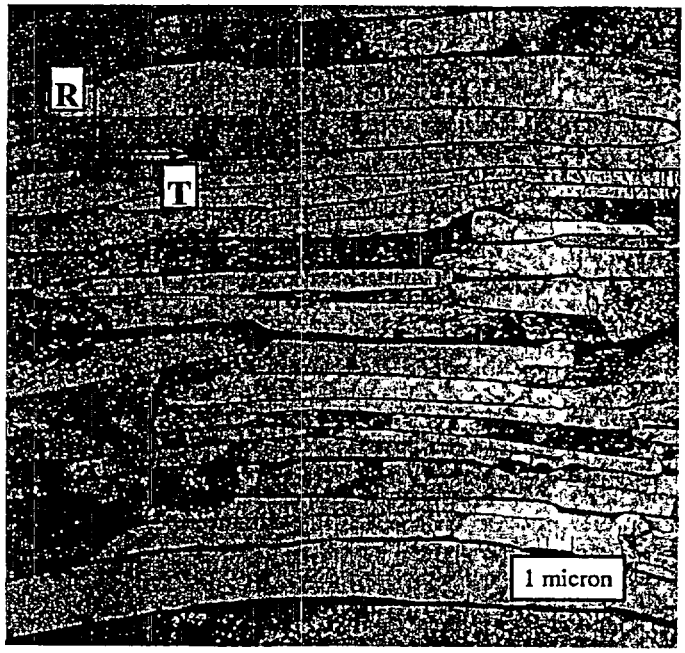

FIG. 1—*Typical grain structure in Zr-2.5Nb pressure tubing looking down the axis of the tube. The light colored α-phase platelets are interspersed with dark-colored β-phase filaments*

Experimental

Samples were prepared to evaluate the impact of various pressure tube microstructural features on corrosion and deuterium ingress. The sources of material for testing were both Zr-2.5Nb pressure tubes and Zr-Nb binary alloy sheets (Table 1). These materials were subjected to mechanical and thermal treatments to produce a variety of microstructural differences relevant to pressure tubes. The main variables investigated were:

- Volume fraction of the β-Zr phase.
- Cold work.
- Thermal decomposition of the B-Zr phase.
- Nb concentration in the α-Zr phase
- Microstructural and microchemical changes due to irradiation.

Corrosion samples were prepared from the source materials by machining to a thickness of about 1 mm. Samples were then chemically polished with a solution of 10% HF + 15% HNO_3 + 30% H_2SO_4 + 45% H_2O to remove any damaged layer introduced by the machining operation Dimensions and weights were measured prior to testing. Tests in out-reactor static autoclaves were carried out in 300°C heavy water; tests under irradiation were carried out in light water in the U2 loop of the NRU research reactor at a temperature of 295°C and a fast neutron flux of 4×10^{17} n/m^2 ($E >$ MeV). In some cases, tests were carried out in oxygenated water in static autoclaves at 300°C to reveal any differences in a shorter time. The oxygen levels ranged from 1000 ppb at the start of each exposure to about 400 ppb at the end of each exposure.

The corrosion was measured as a weight gain for all specimens using a Metler AE163 balance to an accuracy of 0 01 mg and normalized according to the unit area from the measured dimensions. Visual examinations were performed after each exposure to check for obvious changes in appearance.

TABLE 1—*Details of test specimens used for corrosion testing.*

Alloy		Treatment	Attribute
Zr-1Nb	(S)[a]	850°C/1 h air cooled	α Zr + β Zr
Zr-2.5Nb	(S)	850°C/1 h air cooled	α Zr + β Zr
Zr-5Nb	(S)	850°C/1 h air cooled	α Zr + β Zr
Zr-20Nb	(S)	850°C/1 h air cooled	β-Zr
Zr-2.5Nb	(PT)[b]	cold-worked	0–80% cw
Zr-2.5Nb	(PT)	extruded + cold-worked	27% Nb in β-Zr phase
		extruded + 400°C/24 h	48% Nb in β-Zr phase
		extruded + 400°C/100 h	68% Nb in β-Zr phase
		extruded + 400°C/1000 h	75% Nb in β-Zr phase
		extruded + 450°C/100 h	85% Nb in β-Zr phase
Zr 0.02 Nb	(S)	1000°C/1 h/WQ	0 02% Nb in solid solution
Zr 0.07 Nb	(S)	1000°C/1 h/WQ	0 07% Nb in solid solution
Zr 0.15 Nb	(S)	1000°C/1 h/WQ	0.15% Nb in solid solution
Zr 0.3 Nb	(S)	1000°C/1 h/WQ	0.3% Nb in solid solution
Zr 0.68 Nb	(S)	1000°C/1 h/WQ	0 68% Nb in solid solution
Zr 1.35 Nb	(S)	1000°C/1 h/WQ	1.35% Nb in solid solution

[a] S = Sheet
[b] PT = Pressure Tube.

At the end of the corrosion tests, deuterium concentration was measured in selected samples by hot-vacuum-extraction mass spectroscopy techniques.

The microstructural and microchemical composition of various samples were investigated by X-ray diffraction (XRD), neutron diffraction, and transmission electron microscopy.

XRD specimens that were about 1 cm^2 by 0.5 mm thick were prepared by cutting slices out of the pressure tube perpendicular to each of the three principal component axes. The specimens were labeled according to their normals related to the directions in the original tube, i.e., perpendicular to the radial direction (RN), the transverse direction (TN), and the longitudinal direction (LN). Each specimen was then chemically polished to remove any damaged layer introduced by the preparation using a solution of 45% HNO_3, 45% lactic acid ($C_3H_6O_3$), and 5% HF. In this case at least 0 025 mm was removed, that being the depth of damage made by the diamond wheel used to cut the sample.

XRD analyses using second- and third-order $\{10\bar{1}0\}$ and (0002) diffracting planes were performed in a Rigaku diffractometer with a rotoflex rotating-anode generator operating at 12 kW with CuKα radiation. Analyses using first- and second-order $\{11\bar{2}0\}$ diffracting planes were performed in a Siemens Type F diffractometer with a Crystalloflex generator operating at 1 kW with CuKα radiation. Measurements on peak position gives information on lattice strain or chemical composition [*2,3*], and measurements on integral breadth gives information on dislocation densities [*4*].

Interplanar spacings were also determined from neutron diffraction measurements using a neutron diffractometer. Diffraction peaks were collected by scanning a single ^3He detector through a range of scattering angle and counting neutrons. The angular divergences of the incident and diffracted beams were defined by Soller slit collimators to be approximately 0 5° in the scattering plane. Each diffraction peak was fitted with a Gaussian function on a sloping background to determine the mean scattering angle to a typical precision of ±0 003°. Spacings were calculated from the angle of the diffraction peak maximum using Bragg's law.

Samples for transmission electron microscopy were prepared as 0.1-mm-thick, 3-mm-diameter disks. They were polished to electron transparency using a Materials Science Northwest Metalthin twin-jet electropolisher using 10% perchloric acid in ethanol at −40°C. The samples were examined in a Philips CM30 electron microscope.

Results

Effect of the β-Zr Phase Volume Fraction

Zr-1Nb, Zr-2.5Nb, Zr-5Nb, and Zr-20Nb alloys are annealed at 850°C for 1 h to produce samples with varying amount of β-Zr phase. The volume fraction of β-Zr phase increases with Nb content of the alloy. Autoclave corrosion test results after exposures to 300°C deoxygenated water are shown in Fig. 2. The results show that both corrosion and deuterium ingress increase with increasing amounts of β-Zr present. However, the behavior of single-phase β-Zr (Zr-20Nb alloy) is not consistent with the trend exhibited by the two-phase materials; it exhibits the lowest deuterium pickup even though it suffers the greatest corrosion.

Effect of Cold Work

Sections of an as-extruded pressure tube were cold worked by rolling to produce a suite of samples ranging from 0 to 80% cold work. Results of exposures to 295°C deoxygenated water in a reactor loop at both in and out of flux positions are shown in Fig. 3. In the absence

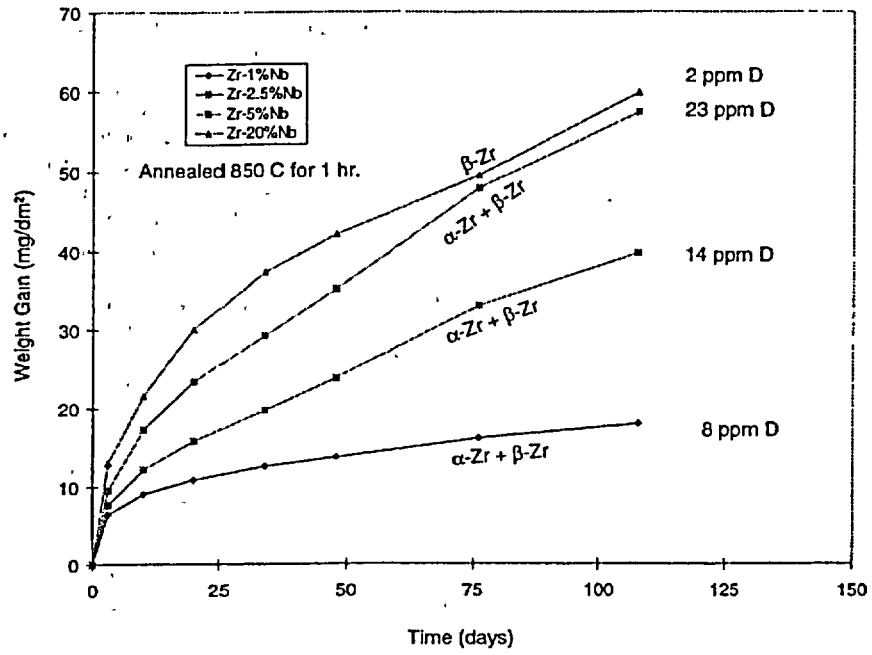

FIG. 2—*Effect of volume fraction of the β-Zr phase on corrosion and deuterium pickup (volume fraction increases with increasing Nb content in these alloys). Deuterium pickup at the end of the test is expressed as ppm D.*

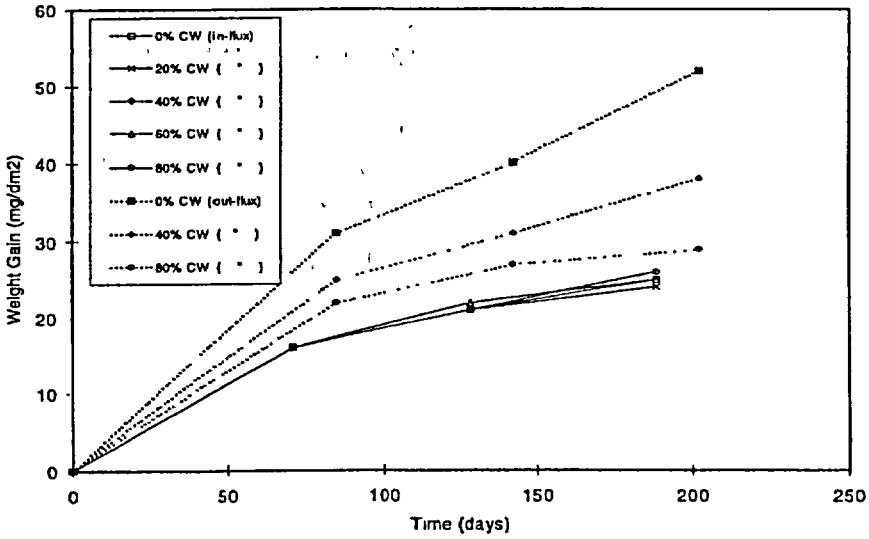

FIG 3—*Effect of cold work on corrosion of Zr-2 5Nb pressure tube material*

of irradiation, corrosion was seen to decrease with increasing cold work. However, under irradiation, corrosion was consistently less than that seen out of flux and there was no evidence for any dependence on cold work.

Effect of Thermal Decomposition of the β-Zr Phase

Pressure tube sections were heated at 400 to 450°C for times ranging from 24 to 1000 h to produce samples with varying amounts of β-Zr decomposition. Results of out-reactor autoclave tests to show the effect of this decomposition on corrosion and deuterium uptake in 300°C oxygenated water (400 to 1000 ppb dissolved oxygen) are given in Fig. 4. Corrosion and deuterium pickup after 280 days exposure are significantly reduced as the amount of β-Zr phase is changed by the heat treatment, with the fully decomposed structure displaying the least corrosion and deuterium pickup.

Effect of Nb Concentration in the α-Zr Phase

Nb is soluble in the α-Zr phase up to concentrations between 0 6 and 1 0 wt%. The effect of Nb concentration in the α-Zr phase was studied using binary alloys containing 0 02 to 1.35 wt% Nb. Alloys were homogenized at 1050°C and water quenched to retain all the Nb in solid solution. The results of samples tested in autoclaves in 300°C deoxygenated water are shown in Fig. 5. The results show that corrosion and deuterium pickup are at a minimum when the Nb concentration is in the range 0.07 to 0.15 wt%.

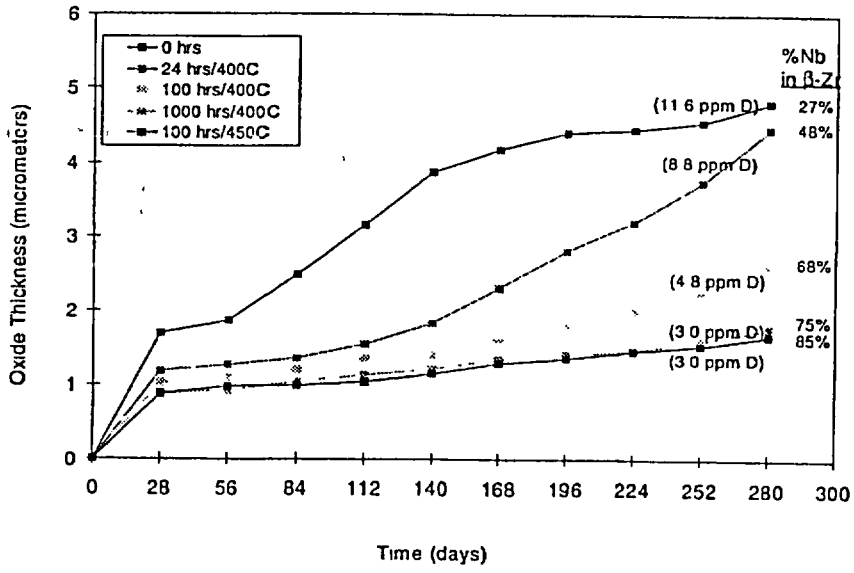

FIG. 4—*Effect of the decomposition of the β-Zr phase on corrosion and deuterium ingress of Zr-2 5Nb pressure tube material Deuterium pickup at the end of the test is expressed as ppm D*

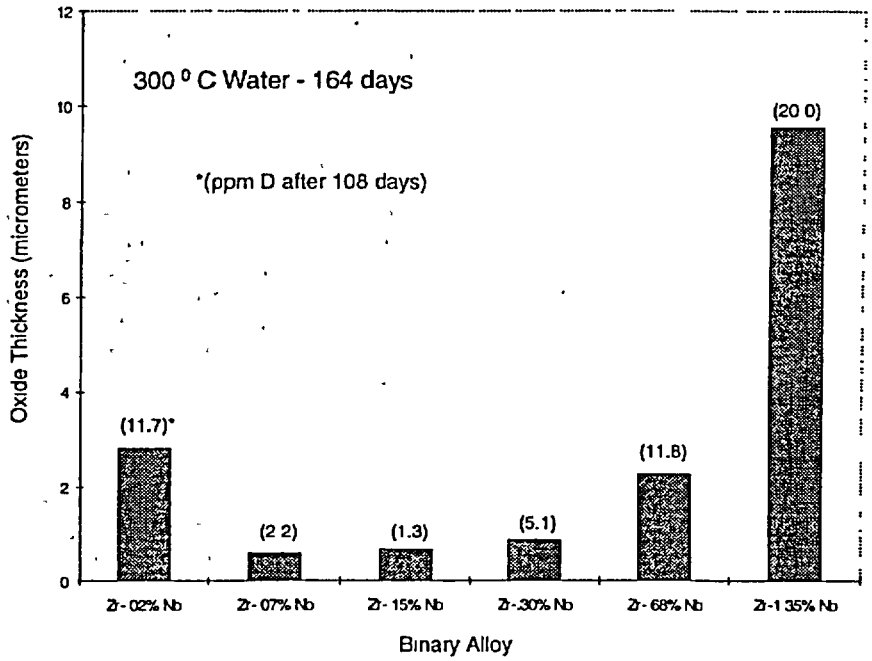

FIG. 5—*Effect of the Nb composition of the α-Zr phase on corrosion and deuterium ingress of Zr-2.5Nb binary alloys.*

Effect of Irradiation-Induced/Enhanced Microstructural Changes

Corrosion samples were prepared from irradiated pressure tubes that had been removed from operating reactors. The fluences of for these tubes ranged from 0.6×10^{25} to 10.4×10^{25} n/m/s^2. Results for zero fluence are for samples of pressure tube offcuts that are archive material from finished tubes just before they are installed. The results from post-irradiation corrosion tests in autoclaves in 300°C deoxygenated water are shown in Fig. 6. The corrosion of pre-irradiated material is lowered as a consequence of the reactor irradiation. The reduction in corrosion response appears to saturate after a fluence of about 1.5×10^{25} n/m^2; however, more testing is required before any definitive statement can be made with regard to an apparent increase for high-fluence samples. Also shown for comparison is the result for an electron-irradiated sample exposed under identical test conditions [*5*].

One of the primary effects of irradiation is to produce dislocation loops in the α-phase. The evolution of these loops was monitored as a function of fluence by measuring the X-ray diffraction line-broadening [*2–4*]. In Fig. 7, prism plane line-broadening shows that the dislocation loop structure evolves rapidly, initially reaching a steady-state density that is primarily a function of temperature. The steady-state condition is achieved after a fluence of about 0.5×10^{25} n/m^{-2} and corresponds with a dislocation density of about 8×10^{14} m^{-2} at the inlet temperature of about 250°C and 6×10^{14} m^{-2} at the outlet temperature of about 300°C.

During the course of irradiation, the partially decomposed β-Zr phase evolves to a steady-state condition (measured from the concentration of Nb in the beta-phase) depending on the

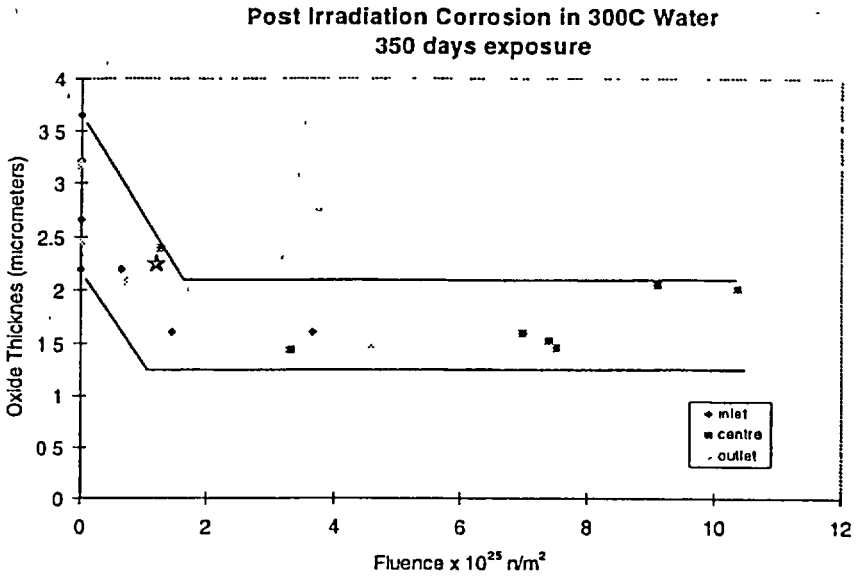

FIG. 6—*Effect of fluence on out-reactor post-irradiation corrosion for Zr-2 5Nb pressure tubes originally irradiated in CANDU reactors. (★ denotes pressure tube material irradiated with electrons)*

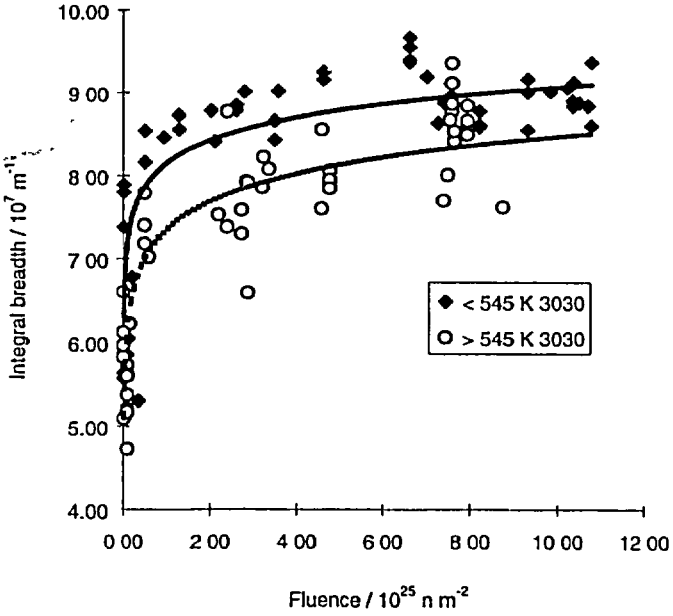

FIG. 7—*Variaton in ⟨a⟩-dislocation density (measured as an integral breadth) for Zr-2.5Nb pressure tubing as a function of fluence in CANDU reactors.*

temperature and flux, Fig. 8. The temperature increases from about 250°C at the inlet to about 300°C at the outlet of a CANDU pressure tube. At the peak flux in a CANDU reactor (about 2×10^{17} n/m^{-2}/s^{-1}), for temperatures between 250 and 300°C, the initial decomposition introduced by autoclaving (as measured by XRD, [4]) is unchanged or reversed, Fig. 9. Although evidence for a reversal in state is not strong (measurement errors being typically <5%), reversal in the thermally decomposed state has been previously observed for well-characterized materials irradiated in controlled reactor conditions [4]. As the flux drops at each end of the tubes, (i.e., where the fluences are low), the β-Zr phase is more decomposed compared to the initial condition. As the temperature increases towards the outlet, the thermal decomposition dominates even though the flux may be significant.

The other main microstructural feature that changes during irradiation is the chemical distribution of the α-phase. Irradiation results in the production of small (2 to 5 nm) Nb-rich precipitates visible after fluences approaching 1×10^{25} n/m^{-2} at 300°C, Fig. 10. Although it is difficult to estimate how the number density of precipitates varies with temperature and fluence (due to difficulties in measuring foil thicknesses for small-grained irradiated material) the size of the precipitates increases with fluence, increasing from <3 nm in diameter at 1×10^{25} n/m^{-2} to between 5 and 10-nm diameter for fluences $> 5 \times 10^{25}$ n/m^{-2} at 300°C. Precipitation is more apparent at 300°C compared with 250°C for similar fluences [6], indicating that there is a slight temperature dependence for precipitation. These β-Nb precipitates are stable during post-irradiation thermal treatment at 500°C, indicating that they are a stable phase at temperatures ≤500°C (Fig. 11)

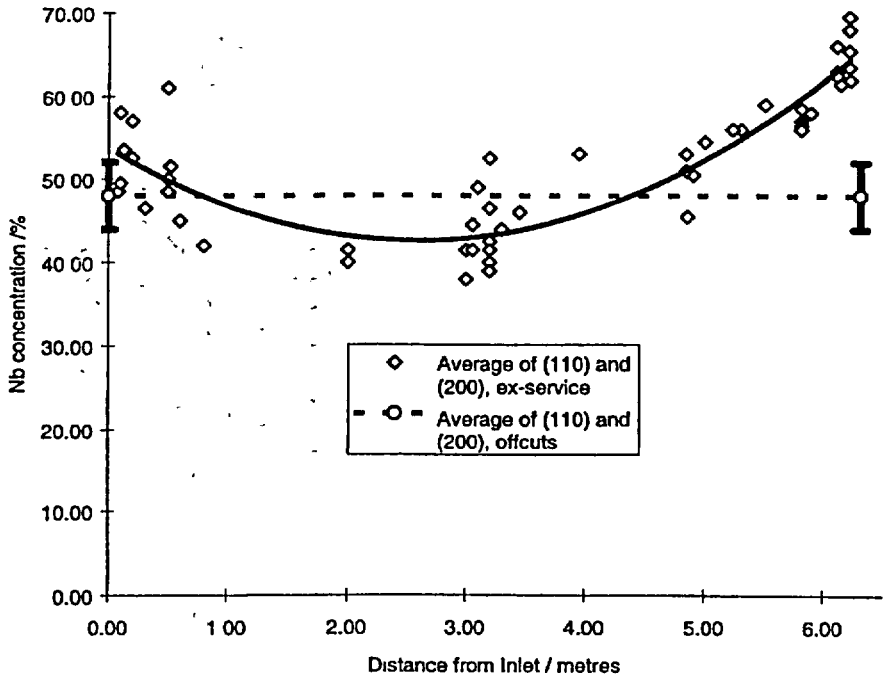

FIG. 8—*Nb concentration in the β-phase of Zr-2 5Nb pressure tubes as a function of position relative to the inlet in CANDU reactors.*

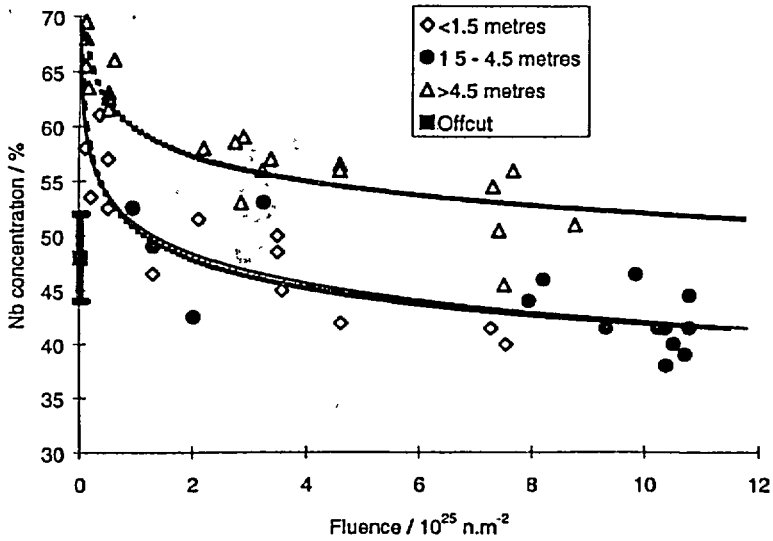

FIG. 9—*Nb concentration in the β-phase of Zr-2 5Nb pressure tubes as a function of fluence at inlets, centers, and outlets in CANDU reactors.*

Direct measurement of the composition of these small precipitates, or the composition of the matrix (irradiated and unirradiated), in an electron microscope is subject to large experimental errors. However, their composition can be measured indirectly from the α-phase lattice parameters. As Nb is an undersized solute [*7*], the lattice parameters decrease with increasing Nb content and vice-versa. Measurements using neutron diffraction on samples

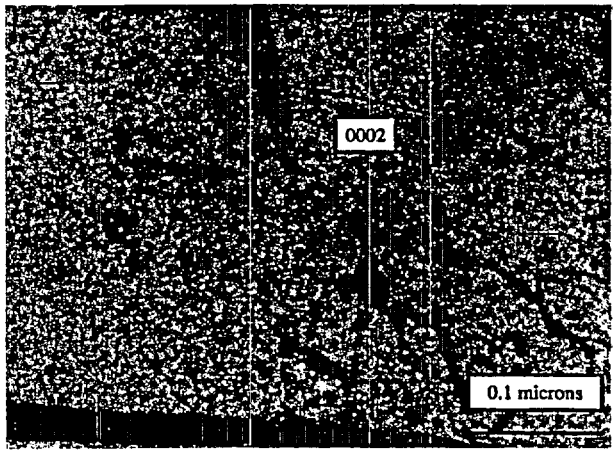

FIG 10—*Micrographs showing β-Nb precipitates (arrowed) in Zr-2 5Nb irradiated at 573 K to a fluence of 0.9 × 10²⁵ n/m⁻².*

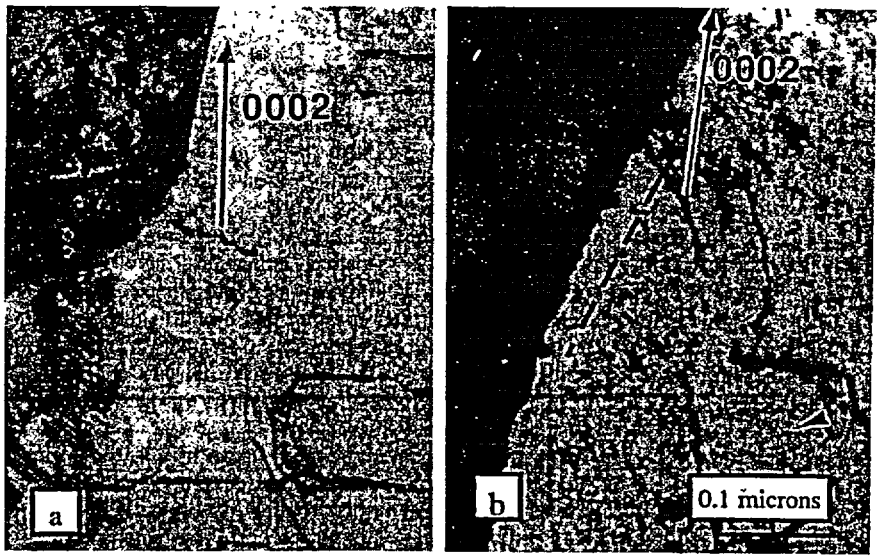

FIG. 11—*Effect of irradiation on Nb precipitation (arrowed in* (b) *in Zr-2.5Nb pressure tubing;* (a) *unirradiated;* (b) *irradiated at 546 K to a fluence of* 6.2×10^{25} n/m^{-2} *plus 1 h at 773 K. The denuded zone at the grain boundary (dotted line) is about 30 mm.*

tested in this study showed that the lattice strains of each irradiated sample increased relative to the unirradiated state, and the change was consistent with a decrease in Nb concentration of about 0.3 wt% using low Nb standards (Table 2).

Discussion

Following forging and fabrication into hollow billets, Zr-2.5Nb pressure tubes are extruded at temperatures of about 815°C in a range where both the α-Zr and β-Zr phases are stable. Examination of the metal-oxide interface regions of pressure tube material after oxidation has shown thicker oxide ridges penetrating into the β-Zr phase in those structures. Therefore, greater amounts of β-Zr phase in two-phase structures have a negative impact on corrosion and deuterium pickup (Fig. 2). Despite the high corrosion, pure β-Zr shows remarkably low deuterium pickup, which seems to be associated with the formation of a more homogeneous

TABLE 2—*Lattice strain measurements measured by neutron diffraction, averaged over six different reflections, for irradiated pressure tube samples relative to unirradiated offcuts.*

Sample	Tempeature/°C	Fluence ($\times 10^{25}$ m/m^{-2})	Strain, 10-4
P4F17	269	1.3	3.7 ± 0.6
B2X14	286	3 03	4 2 ± 0.6
P4N16	267	7.25	3 5 ± 0 6
P3J09	268	7.56	3.3 ± 0 6

oxide compared to more heterogeneous and porous oxides that form on the two-phase α-Zr + β-Zr structures [*8*].

Pressure tubes are cold drawn about 27% to attain their final wall thickness. The ends of the tubes experience an additional 12 to 13% cold work when the mechanical rolled joints are made with the stainless steel end-fitting during installation into the reactor. The implication from Fig. 3 is that there would be a slight benefit of this rolling on corrosion at the pressure tube ends where the neutron flux is negligible. The reason for the observed corrosion reduction with cold work is not completely understood. Work on Zircaloy-2 indicates that cold-working up to 40% does not significantly alter the corrosion and H uptake characteristics [*9*]. It is possible that cold-working in a binary Zr-Nb alloy such as Zr-2.5Nb could enhance the precipitation of Nb from supersaturated solid solution either during thermal aging (which would occur to some extent during a corrosion test) and that this could lead to an improvement in corrosion properties [*1*]. However, in-reactor the impact of irradiation-induced effects is so overwhelming that the dependence on cold work seen out of flux is not observed. Thus, any requirement for a reduction in cold work, for example, to help mitigate pressure tube creep, would not affect the corrosion behavior of the tubes.

Pressure tubes are given a final stress relief treatment in steam at 400°C. During this treatment the metastable β-Zr phase will undergo some thermal decomposition with further decomposition occurring during service. From Fig. 4 this thermal decomposition is beneficial, contributing to reductions in both corrosion and deuterium pickup. The benefit is likely due to the decomposition of the metastable β-Zr phase, leading to a smaller volume fraction of total β-phase [*10*]. However, any change in volume fraction due to one 24-h heat treatment at 400°C is small and is unlikely to be significant relative to other factors affecting long-term corrosion, primarily α-phase composition.

In the as-fabricated condition, the α-Zr platelets are supersaturated with respect to Nb, containing between 0.6 and 1.0 wt% Nb, amounts that are established by the fabrication process and the Zr-Nb phase diagram. At reactor operating temperatures, Nb solubility is lower so there is the potential for β-Nb precipitation to occur with a concomitant reduction in the matrix Nb concentration. The results from Fig. 5 suggest that, if this process does occur, the associated reduction in matrix concentration contributes to a reduction in the corrosion and deuterium uptake.

The reduction in corrosion observed on pre-irradiated pressure tube material, Fig. 6, is a result of changes that occurred to the base metal structure during service under irradiation. The increased dislocation density during irradiation (Fig. 7) is consistent with the improvements in corrosion resistance due to cold-working. However, it is probable that any improvement due to the increased dislocation density is due to the enhancement of precipitation of Nb, especially given the results of tests on material irradiated at high temperatures showing evidence for improved corrosion resistance in materials where Nb has precipitated but in the absence of dislocation loops [*5*].

X-ray diffraction measurements show that the thermal decomposition of the β-phase is suppressed during irradiation and even reversed at a sufficiently low temperature and sufficiently high flux [*4*] (Fig. 8). The change in state of the β-phase with increasing fluence (Fig. 9) occurs over the same fluence range as the change in corrosion properties (Fig. 6). However, the effect of irradiation is to increase, rather than decrease, the volume fraction of metastable β-Zr [*4*], and there is a significant difference at the inlets compared with outlets; neither of these factors are consistent with the corrosion data (Figs. 2 and 6). Therefore, it is unlikely that changes to the β-phase during irradiation are responsible for the improvement in corrosion properties and may, in fact, have a negative impact on corrosion.

During irradiation, not only does the state of the β-Zr phase change with time, but the Fe, initially segregated in the β-Zr phase, is dispersed into the α-Zr phase [*2–4*]. The matrix

iron concentration is gradually increased over a fluence range of about 2×10^{25} n/m^{-2}. Again, comparison with other work on Zircaloys [*11*] suggests that an increase in the amount of Fe dispersed in the α-phase results in increased uniform corrosion and therefore is unlikely to have anything other than a negative impact on corrosion resistance in this case unless there are synergistic effects with Nb that are different from those with Sn.

The main factor leading to improvement in corrosion properties in Zr-2.5Nb pressure tubing in-reactor then appears to be the reduction in Nb content in the α-phase due to the precipitation of β-Nb precipitates. In this respect, dislocations introduced by cold-work and dislocation loops produced by irradiation probably play a role in assisting nucleation of Nb from solution. The rate of precipitation during irradiation is a balance between irradiation-induced mixing causing shrinkage and radiation-enhanced diffusion-causing growth [*12*]. Previous work [*13*] has shown that precipitation occurs inhomogeneously (at dislocations) during irradiation at 500°C but is not observed during thermal treatment at the same time and temperature in the absence of irradiation. In the same work [*13*], post-irradiation annealing at 500°C of material that had previously been irradiated at 300°C showed that the β-Nb precipitates coarsened, indicating that Nb mobility was not a limiting factor for Nb precipitation during thermal treatments at temperatures of about 500°C, this is consistent with rate-theory calculations.

During irradiation, the concentrations of point defects in a metal are given by the following rate equations:

$$G - k^2(v)\, D(v)C(v) - RC(v)\, C(i) = \dot{C}\,(v) \tag{1}$$

$$G - k^2(i)\, D(i)C(i) - RC(v)\, C(i) = \dot{C}\,(i) \tag{2}$$

where $k^2(v)$ and $k^2(i)$ are the sink strengths of various microstructural features such as a-type and c-type dislocations and grain boundaries, $D(v)$ and $D(i)$ are the diffusion coefficients, and $C(v)$ and $C(i)$ are the point defect concentrations for vacancies and interstitials, respectively. G is the damage production rate, and R is a recombination rate parameter [*14*].

After an initial transient in microstructure evolution (due mainly to a-type dislocation loop formation for fluences $< 1 \times 10^{25}$ n/m^{-2}), any further evolution of the sink structure occurs primarily by climb of existing defects and slowly varies with time. At any one instant in this regime, one can assume that the sink strength is constant, as the time taken for the point defect concentrations to reach steady-state values is very small compared with the rate of change in the sink structure. In these circumstances the steady-state point defect concentrations satisfy the following simultaneous equations:

$$G - k^2(v)\, D(v)C(v) - RC(v)C(i) = 0 \tag{3}$$

$$G - k^2(i)\, D(i)C(i) - RC(v)C(i) = 0 \tag{4}$$

Solving these equations using appropriate temperature-dependent sink densities relevant to Zr-2.5Nb pressure tubes yields values for steady-state point defect concentrations. From the vacancy concentrations, the effect on thermal diffusion coefficients of Nb Zr in α-Zr [*15*] can be calculated. From the diffusion coefficients, values for mean-free paths of Nb and Zr for a typical CANDU reactor irradiation lasting one year have been calculated and are plotted in Fig. 12. Also shown in Fig. 12 are similar plots for Zr to illustrate that Nb has a higher diffusion rate compared with Zr self-diffusion. The graph shows that at 500°C thermal diffusion dominates any irradiation enhancement. It also shows that at reactor operating temperatures of about 250 to 300°C, the mean-free path for Nb is about 10 nm, which is

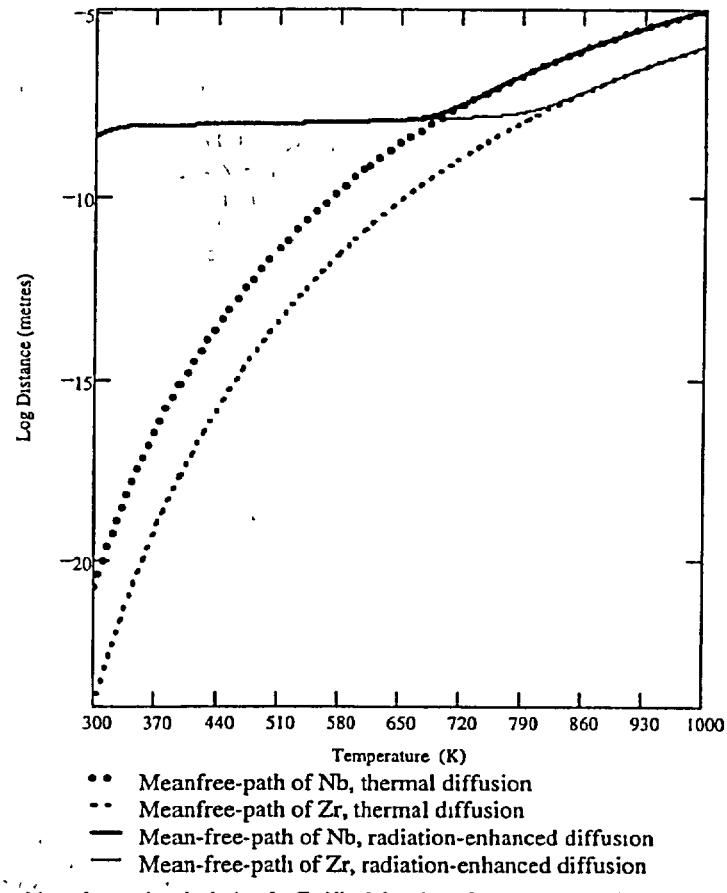

FIG. 12—*Mean-free path calculation for Zr-Nb alpha phase for one year irradiation, i e., for a fluence of about 0.7 × 10^{25} n/m^{-2} at the center of a CANDU reactor.*

comparable with the denuded zone width for β-Nb precipitates close to grain boundaries (Fig. 11). These calculations imply that thermal diffusion at 500°C dominates any irradiation enhancement of diffusion. Therefore, a reduction of Nb concentration in the supersaturated α-phase could be achieved by thermal treatment at this temperature. The fact that precipitation is not observed during thermal treatment at 500°C implies that either the degree of undercooling is insufficient to induce precipitation or that the diffusion to existing sinks such as grain boundaries is sufficiently rapid to suppress any precipitation within the grains. However, the observation of precipitation during irradiation at 500°C but not during thermal treatment at the same temperature [*13*] indicates that irradiation introduces an added factor favoring precipitation. This could be the formation of jogs on existing dislocations or through the creation of an irradiation-induced supersaturation of Nb interstitial atoms that form clusters more easily than substitutionally diffusing species.

Conclusions

Out-reactor corrosion tests on dual-phase Zr-Nb alloys with controlled microstructures show that one of the most important factors affecting the corrosion properties the thermodynamic state of the α- and β-phases present. At equilibrium, the volume fraction of the β-phase and the concentration of Nb in the α-phase is minimized, resulting in lower corrosion rates. For Zr-2.5Nb pressure tubing operating in CANDU reactors, the most important factor leading to reduced corrosion rates is the precipitation of β-Nb particles and the concomitant reduction of Nb in the matrix of the α-Zr grains during irradiation.

Precipitate formation occurs as a result of a complex combination of factors: degree of supersaturation, density of nucleation sites, and diffusion rate (dependent on neutron flux and temperature). For CANDU reactor fluxes and temperatures, the irradiation enhancement of diffusion dominates over thermal diffusion, and the reduction in Nb concentration is assisted by precipitate formation at sinks.

Acknowledgments

This work was made possible by the collaboration of many groups at AECL, including L. Woodworth and D. Nye at the Whiteshell Laboratory, and at the Chalk River Laboratory: A. Shaddick, R Resmer, and T. G. Lamarche for the corrosion experiments and deuterium analyses; P. Clarke for the neutron diffraction measurements; J. F. Mecke and J. E. Winegar for the X-ray diffraction measurements; and D. Phillips for preparation of transmission electron microscopy specimens.

References

[1] Urbanic, V. F. and Gilbert, R W., "Effect of Microstructure on the Corrosion of Zr-2.5Nb Alloy," IAEA Technical Committee Meeting on Fundamental Aspects of Corrosion of Zirconium Based Alloys," Portland, OR, 1989.

[2] Griffiths, M., Chow, C. K., Coleman, C. E., Holt, R. A , Sagat, S , and Urbanic, V. F, "Evolution of Microstructure in Zr-Alloy Core Components during Service," *Effects of Radiation on Materials (16th Vol.), ASTM STP 1175,* 1993, p 1077, Issued as AECL 10844, COG-92-54.

[3] Urbanic, V F and Griffiths, M., "Corrosion Response of Pre-irradiated Zr-2 5Nb Pressure Tube Material," *Effects of Radiation on Materials: 17th International Symposium, ASTM STP 1270,* D. S. Gelles, R. K. Nanstad, A. S Kumar, and E A Little, Eds., American Society for Testing and Materials, West Conshohocken, PA, 1996, pp 1088–1106.

[4] Griffiths, M , Mecke, J. F., and Winegar, J. E., "Evolution of Microstructure in Zirconium Alloys during Irradiation," *Zirconium in the Nuclear Industry· Eleventh International Symposium, ASTM STP 1295,* E. R. Bradley and G. P. Sabol, Eds., American Society for Testing and Materials, West Conshohocken, PA, 1996, pp 580–602. Also as AECL Report RC-1477.

[5] Woo, O. T. et al., "Corrosion of Electron-Irradiated Zr-2 5Nb and Zircaloy-2," this publication.

[6] Hosbons, R. R. et al., "Effect of Long-term Irradiation on the Fracture Properties of Zr-2 5Nb Pressure tubes," this publication

[7] Douglas, D L , "The Physical Metallurgy of Zirconium," *International Atomic Review,* IAEA, Vienna, 1971.

[8] Urbanic, V. F., Chan, P. K , Khatamian, D , and Woo, O T., "Growth and Characterization of Oxide Films on Zirconium-Niobium Alloys," *Zirconium in the Nuclear Industry: Tenth International Symposium, ASTM STP 1245,* A. M. Garde and E. R. Bradley, Eds , American Society for Testing and Materials, Philadelphia, PA, 1994, pp 116–130.

[9] Burns, W. A and Maffei, H P., "Neutron Irradiation and Cold Work Effects on Zircaloy-2 Corrosion and Hydrogen Pickup," *ASTM STP 368,* 1963, pp. 101–117.

[10] Urbanic, V. F, Warr, B. D, Manolescu, A., Chow, C K, and Shanahan, M. W., "Oxidation and Deuterium Uptake of Zr-2.5Nb Pressure Tubes in CANDU-PHW Reactors," *Zirconium in the Nuclear Industry· Eighth International Symposium, ASTM STP 1023,* L F. P Van Swam and C. M. Eucken, Eds., American Society for Testing and Materials, Philadelphia, PA, 1989, pp. 20–34.

[11] Huang, P. Y., Mahmood, S. T., and Adamson, R. B, "Effects of Thermomechanical Processing on In-reactor Corrosion and Post-irradiation Mechanical Properties of Zircaloy-2," *Zirconium in the Nuclear Industry Tenth International Symposium, ASTM STP 1295,* E R. Bradley and G P Sabol, Eds., American Society for Testing and Materials, West Conshohocken, PA, 1996, pp 726–757.

[12] Nelson, R. S, Hudson, J. A., and Mazey, D. J, "The Stability of Precipitates in an Irradiation Environment," *Journal of Nuclear Materials,* Vol. 44, 1972, pp. 318–330.

[13] Coleman, C. E, Gilbert, R. W., Carpenter, G. J. C, and Weatherley, G. C., "Precipitation in Zr-2.5 wt% Nb During Neutron Irradiation in Phase Stability During Irradiation," J. R. Holand, L K Mansur, and D I. Potter, Eds., from *Phase Stability During Irradiation,* The Metallurgical Society of AIME, Pittsburgh, PA, 1981, pp. 587–599.

[14] Heald, P. T. and Speight, M. V, "Point Defect Behavior in Irradiated Materials," *Acta Metallurgica,* Vol. 23, 1975, p. 1389.

[15] Hood, G. M., "Nb-Diffusion in Single-crystal α-Zr," AECL report, RC-1674

DISCUSSION

B. Cox[1] (*written discussion*)—In your plot of post-irradiation corrosion rate as a function of neutron fluence you interpreted the results as a reduction with fluence followed by a plateau. A line through the actual plots would suggest a minimum in the curves. Is it reasonable to expect a minimum from other observations?

V. Urbanic et al. (*authors' closure*)—The observed reduction in the corrosion response with fluence is significant and most obvious and we argue in this paper that microstructural changes occurring in the α-Zr phase are largely responsible for this behavior As you point out, the data suggest that there may be a minimum in the response although we have indicated that the observed reduction with fluence is followed by a plateau. One might argue the possibility for a minimum based on the following. Figure 3 shows that corrosion is reduced as the β-Zr phase is decomposed. The date of Figs. 7 and 8 illustrate that decomposition of the β-Zr phase is reversed under irradiation. Thus, there is the possibility that the two data points at the highest fluence are showing an upward trend for this reason. However, we feel that additional exposures for these samples and on new samples with even higher fluences are required before a legitimate claim for a minimum in the response can be made.

R. Adamson[2] (*written discussion*)—What ideas do you have on *why* the effects of Nb on corrosion are as you describe them?

V. Urbanic et al (*authors' closure*)—The results of tests on dilute binary alloys show a minimum in corrosion around 0.1 wt% Nb. The solubility of Nb in Zr at 883 K is about 0.6 to 1.0 wt%. It is recognized that the solubility decreases with decreasing temperature; however, such data at lower temperatures is limited. Despite this, it is thought that the optimum behavior at about 0.1 wt% Nb may be related to the fact that this could be close to the solubility limit of Nb in Zr at the corrosion tests temperature of 573 K.

Y. Hatano[3] (*written discussion*)—Did you examine the chemical form of Nb in the oxide film?

V. Urbanic et al. (*authors' closure*)—In this work the chemical form of Nb in the oxide film was not investigated. However, we have investigated the chemical state of Nb in oxide films formed on Zr-20wt%Nb (the β-Zr phase composition) in earlier work (*ASTM STP 1245*). In that work there was evidence from XPS analyses for predominantly Nb^{+5} at the outer oxide regions. Within the oxide, niobium existed in the Nb^{5+} and Nb^{2+} states; however, evidence for its existence in the valence state lower than 2^+ was also found.

[1] University of Toronto, Toronto, Ont., Canada.
[2] GE NE, Pleasanton, CA.
[3] Toyama University, Toyama, Japan.

Vincent, F. Urbanic[1] and Malcolm Griffiths[1]

Microstructural Aspects of Corrosion and Hydrogen Ingress in Zr-2.5Nb

REFERENCE: Urbanic, V. F. and Griffiths, M., **"Microstructural Aspects of Corrosion and Hydrogen Ingress in Zr-2.5Nb,"** *Zirconium in the Nuclear Industry: Twelfth International Symposium, ASTM STP 1354,* G P. Sabol and G D. Moan, Eds., American Society for Testing and Materials, West Conshohocken, PA, 2000, 641–657.

ABSTRACT: Zr-2.5Nb alloy pressure tubes for CANDU® reactors are nominally extruded at 815°C, cold-worked about 27%, and stress-relieved at 400°C for 24 h. The resulting structure consists of elongated α-Zr grains interspersed with a network of thin β-Zr filaments. Corrosion tests on unirradiated and preirradiated material have investigated the effects of microstructure and microchemistry on corrosion and hydrogen ingress. In two-phase (α-Zr+β-Zr) structures, the corrosion and hydrogen pickup increases with increasing volume fraction of β-Zr. Corrosion is highest for single β-phase material although hydrogen pickup reverts to a minimum value. Tests on alloys with low Nb concentration show that the optimum corrosion resistance occurs at a Nb content of about 0.1 wt% Nb. Thermal aging the metastable two-phase structure reduces corrosion and is consistent with a lower β-phase volume fraction and a lower concentration of Nb in the α-phase.

Cold working the as-extruded two-phase structure up to about 80%, prior to stress relieving, reduces the out-reactor corrosion by about a factor of two. However, in-reactor, the benefits of cold work are negligible since there is a suppression of corrosion in irradiated Zr-2.5Nb that dominates all other effects. Irradiation results in an increase in dislocation density due to dislocation loop formation and also enhances the progression to an equilibrium α-phase composition manifested by the appearance of Nb-rich precipitates. Both of these effects of irradiation on microstructure are associated with improved corrosion properties based on tests of materials with controlled microstructures and microchemistry. Any thermally induced decomposition of the α-phase, resulting from the stress-relief heat-treatment, is slowed or even reversed by irradiation, depending on flux and temperature, and is therefore unlikely to have a significant effect on corrosion of irradiated materials. One of the most important factors leading to improved corrosion properties in Zr-2 5Nb pressure tubing seems to be the precipitation of β-Nb particles and the concomitant reduction of Nb in the matrix of the α-Zr grains during irradiation. Apart from any direct effects of cold-working or dislocation loop formation, it is likely that increased dislocation densities will also enhance Nb precipitation.

KEYWORDS: microstructure, corrosion, Zr-Nb alloys, irradiation damage, diffusion

Zr-2.5 Nb pressure tubes for CANDU reactors are formed by extrusion at a temperature about 815°C. They are then cold-drawn about 27% to give a final tube length of 6.3 m ith a final tube thickness of about 4.3 mm and an inside diameter of about 104 mm. The bes contain a mixture of a- and c-component dislocations with densities of about 4×10^{14} $^{-2}$ and 1×10^{14} m^{-2}, respectively, and have a dual-phase alpha/beta structure. The alpha- iase grains are platelets (containing about 0.6 to 1 wt% Nb in solution) with aspect ratios about 1, 10, and 40 in the radial, transverse, and longitudinal directions, respectively.

[1] Senior research scientists, Atomic Energy of Canada Limited, Chalk River Laboratories, Chalk River, tario K0J 1J0, Canada

They are mostly oriented with prism $\{11\bar{2}0\}$ planes perpendicular to the radial direction, prism $\{10\bar{1}0\}$ planes perpendicular to the longitudinal direction, and basal (0001) planes perpendicular to the transverse direction. The α-grains are stacked together and separated by a nonequilibrium β-phase containing about 20 wt% Nb. A final autoclaving treatment results in partial decomposition of the β-phase with the formation of Nb-depleted ω precipitates in a Nb-enriched matrix (up to about 50 wt%); the average composition in the β-phase remains at about 20 wt%. The β-phase itself has a characteristic texture with (200) planes oriented perpendicular to the radial direction and the (110) planes oriented perpendicular to the longitudinal and transverse directions. The width of the beta phase in the radial direction is about one-tenth that of the alpha base. The width of the alpha phase is typically about 0.3 μm at the end of the tube corresponding with the back end of the extrusion and 0.5 μm at the end of the tube corresponding with the front end of the extrusion. The grain size varies along the length of the tubes because the tubes cool during the extrusion process so that the front end is extruded at a higher temperature compared with the back end, thus affecting the final grain size. A typical microstructure is illustrated in Fig. 1.

Previous work has shown that corrosion of Zr-2.5Nb can be very sensitive to microstructure [*1*] and that the corrosion of resistance Zr-2.5Nb improves with irradiation [*1–3*]. This improvement has been attributed to changes in the microstructure that occur during irradiation [*4*]. The aim of the current work is to investigate in more detail the relationship between the as-fabricated microstructure and the impact of its evolution during irradiation on subsequent corrosion and deuterium ingress.

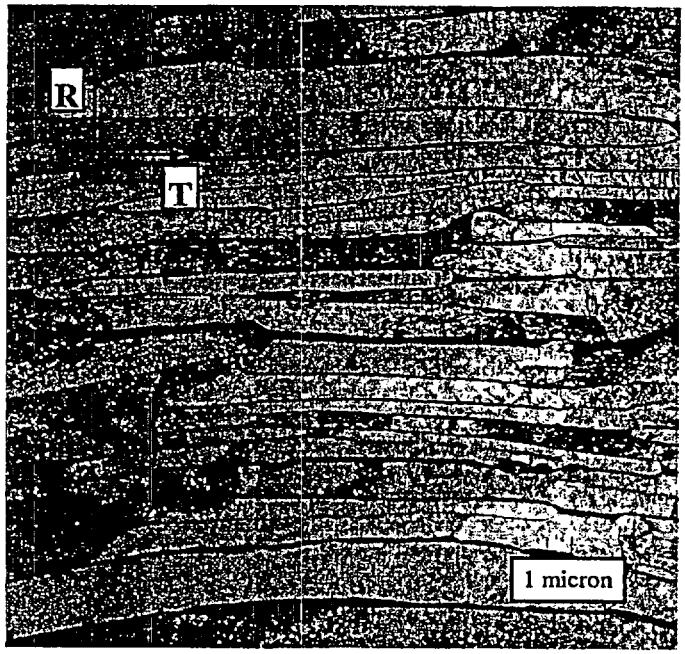

FIG. 1—*Typical grain structure in Zr-2.5Nb pressure tubing looking down the axis of the tube. The light colored α-phase platelets are interspersed with dark-colored β-phase filaments.*

Experimental

Samples were prepared to evaluate the impact of various pressure tube microstructural features on corrosion and deuterium ingress The sources of material for testing were both Zr-2.5Nb pressure tubes and Zr-Nb binary alloy sheets (Table 1). These materials were subjected to mechanical and thermal treatments to produce a variety of microstructural differences relevant to pressure tubes The main variables investigated were:

- Volume fraction of the β-Zr phase.
- Cold work.
- Thermal decomposition of the B-Zr phase.
- Nb concentration in the α-Zr phase.
- Microstructural and microchemical changes due to irradiation.

Corrosion samples were prepared from the source materials by machining to a thickness of about 1 mm Samples were then chemically polished with a solution of 10% HF + 15% HNO_3 + 30% H_2SO_4 + 45% H_2O to remove any damaged layer introduced by the machining operation. Dimensions and weights were measured prior to testing. Tests in out-reactor static autoclaves were carried out in 300°C heavy water; tests under irradiation were carried out in light water in the U2 loop of the NRU research reactor at a temperature of 295°C and a fast neutron flux of 4×10^{17} n/m^2 ($E >$ MeV). In some cases, tests were carried out in oxygenated water in static autoclaves at 300°C to reveal any differences in a shorter time. The oxygen levels ranged from 1000 ppb at the start of each exposure to about 400 ppb at the end of each exposure.

The corrosion was measured as a weight gain for all specimens using a Metler AE163 balance to an accuracy of 0.01 mg and normalized according to the unit area from the measured dimensions. Visual examinations were performed after each exposure to check for obvious changes in appearance.

TABLE 1—*Details of test specimens used for corrosion testing.*

Alloy		Treatment	Attribute
Zr-1Nb	(S)[a]	850°C/1 h air cooled	α Zr + β Zr
Zr-2 5Nb	(S)	850°C/1 h air cooled	α Zr + β Zr
Zr-5Nb	(S)	850°C/1 h air cooled	α Zr + β Zr
Zr-20Nb	(S)	850°C/1 h air cooled	β-Zr
Zr-2.5Nb	(PT)[b]	cold-worked	0–80% cw
Zr-2 5Nb	(PT)	extruded + cold-worked	27% Nb in β-Zr phase
		extruded + 400°C/24 h	48% Nb in β-Zr phase
		extruded + 400°C/100 h	68% Nb in β-Zr phase
		extruded + 400°C/1000 h	75% Nb in β-Zr phase
		extruded + 450°C/100 h	85% Nb in β-Zr phase
Zr 0.02 Nb	(S)	1000°C/1 h/WQ	0.02% Nb in solid solution
Zr 0 07 Nb	(S)	1000°C/1 h/WQ	0.07% Nb in solid solution
Zr 0.15 Nb	(S)	1000°C/1 h/WQ	0.15% Nb in solid solution
Zr 0.3 Nb	(S)	1000°C/1 h/WQ	0 3% Nb in solid solution
Zr 0 68 Nb	(S)	1000°C/1 h/WQ	0 68% Nb in solid solution
Zr 1.35 Nb	(S)	1000°C/1 h/WQ	1.35% Nb in solid solution

[a] S = Sheet
[b] PT = Pressure Tube.

At the end of the corrosion tests, deuterium concentration was measured in selected samples by hot-vacuum-extraction mass spectroscopy techniques.

The microstructural and microchemical composition of various samples were investigated by X-ray diffraction (XRD), neutron diffraction, and transmission electron microscopy.

XRD specimens that were about 1 cm^2 by 0.5 mm thick were prepared by cutting slices out of the pressure tube perpendicular to each of the three principal component axes. The specimens were labeled according to their normals related to the directions in the original tube, i.e., perpendicular to the radial direction (RN), the transverse direction (TN), and the longitudinal direction (LN). Each specimen was then chemically polished to remove any damaged layer introduced by the preparation using a solution of 45% HNO_3, 45% lactic acid ($C_3H_6O_3$), and 5% HF. In this case at least 0.025 mm was removed, that being the depth of damage made by the diamond wheel used to cut the sample.

XRD analyses using second- and third-order $\{10\bar{1}0\}$ and (0002) diffracting planes were performed in a Rigaku diffractometer with a rotoflex rotating-anode generator operating at 12 kW with CuKα radiation. Analyses using first- and second-order $\{11\bar{2}0\}$ diffracting planes were performed in a Siemens Type F diffractometer with a Crystalloflex generator operating at 1 kW with CuKα radiation. Measurements on peak position gives information on lattice strain or chemical composition [*2,3*], and measurements on integral breadth gives information on dislocation densities [*4*].

Interplanar spacings were also determined from neutron diffraction measurements using a neutron diffractometer. Diffraction peaks were collected by scanning a single ^3He detector through a range of scattering angle and counting neutrons. The angular divergences of the incident and diffracted beams were defined by Soller slit collimators to be approximately 0.5° in the scattering plane. Each diffraction peak was fitted with a Gaussian function on a sloping background to determine the mean scattering angle to a typical precision of ±0.003°. Spacings were calculated from the angle of the diffraction peak maximum using Bragg's law.

Samples for transmission electron microscopy were prepared as 0.1-mm-thick, 3-mm-diameter disks. They were polished to electron transparency using a Materials Science Northwest Metalthin twin-jet electropolisher using 10% perchloric acid in ethanol at −40°C. The samples were examined in a Philips CM30 electron microscope.

Results

Effect of the β-Zr Phase Volume Fraction

Zr-1Nb, Zr-2.5Nb, Zr-5Nb, and Zr-20Nb alloys are annealed at 850°C for 1 h to produce samples with varying amount of β-Zr phase. The volume fraction of β-Zr phase increases with Nb content of the alloy. Autoclave corrosion test results after exposures to 300°C deoxygenated water are shown in Fig. 2. The results show that both corrosion and deuterium ingress increase with increasing amounts of β-Zr present. However, the behavior of single-phase β-Zr (Zr-20Nb alloy) is not consistent with the trend exhibited by the two-phase materials; it exhibits the lowest deuterium pickup even though it suffers the greatest corrosion.

Effect of Cold Work

Sections of an as-extruded pressure tube were cold worked by rolling to produce a suite of samples ranging from 0 to 80% cold work. Results of exposures to 295°C deoxygenated water in a reactor loop at both in and out of flux positions are shown in Fig. 3. In the absence

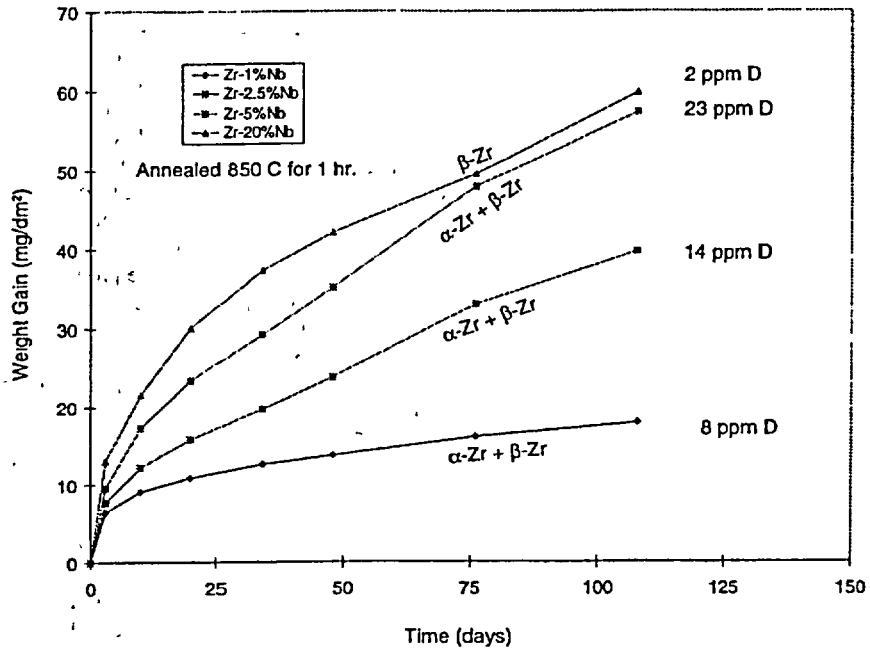

FIG 2—*Effect of volume fraction of the β-Zr phase on corrosion and deuterium pickup (volume fraction increases with increasing Nb content in these alloys). Deuterium pickup at the end of the test is expressed as ppm D.*

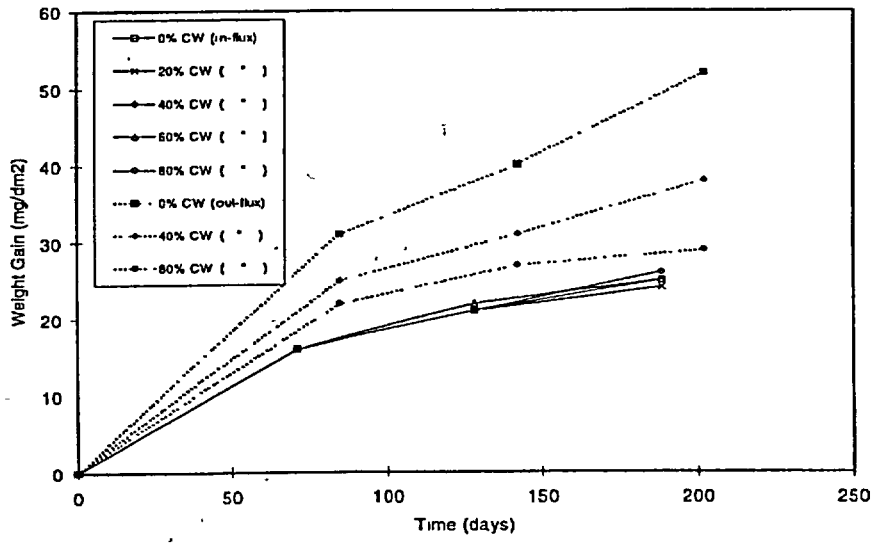

FIG. 3—*Effect of cold work on corrosion of Zr-2 5Nb pressure tube material*

of irradiation, corrosion was seen to decrease with increasing cold work. However, under irradiation, corrosion was consistently less than that seen out of flux and there was no evidence for any dependence on cold work.

Effect of Thermal Decomposition of the β-Zr Phase

Pressure tube sections were heated at 400 to 450°C for times ranging from 24 to 1000 h to produce samples with varying amounts of β-Zr decomposition. Results of out-reactor autoclave tests to show the effect of this decomposition on corrosion and deuterium uptake in 300°C oxygenated water (400 to 1000 ppb dissolved oxygen) are given in Fig. 4. Corrosion and deuterium pickup after 280 days exposure are significantly reduced as the amount of β-Zr phase is changed by the heat treatment, with the fully decomposed structure displaying the least corrosion and deuterium pickup.

Effect of Nb Concentration in the α-Zr Phase

Nb is soluble in the α-Zr phase up to concentrations between 0.6 and 1.0 wt%. The effect of Nb concentration in the α-Zr phase was studied using binary alloys containing 0 02 to 1 35 wt% Nb. Alloys were homogenized at 1050°C and water quenched to retain all the Nb in solid solution. The results of samples tested in autoclaves in 300°C deoxygenated water are shown in Fig. 5. The results show that corrosion and deuterium pickup are at a minimum when the Nb concentration is in the range 0 07 to 0.15 wt%.

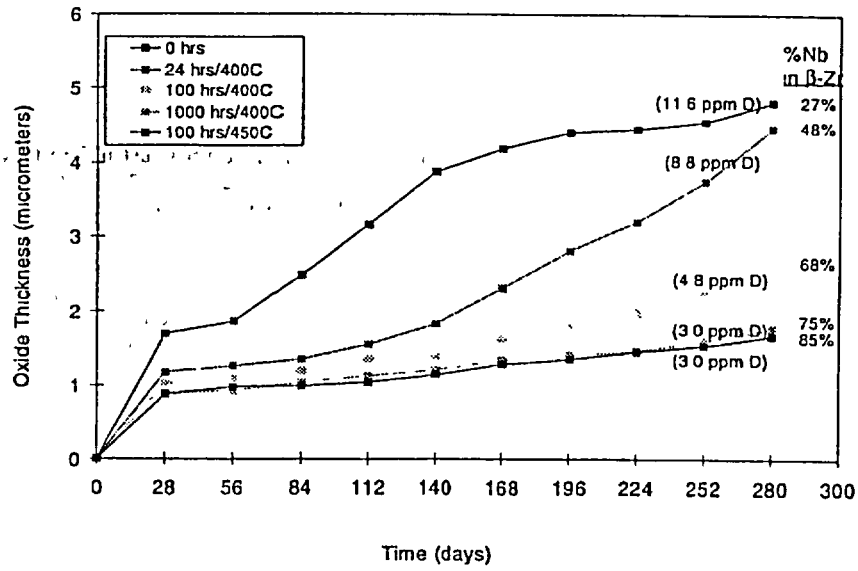

FIG. 4—*Effect of the decomposition of the β-Zr phase on corrosion and deuterium ingress of Zr-2 5Nb pressure tube material. Deuterium pickup at the end of the test is expressed as ppm D.*

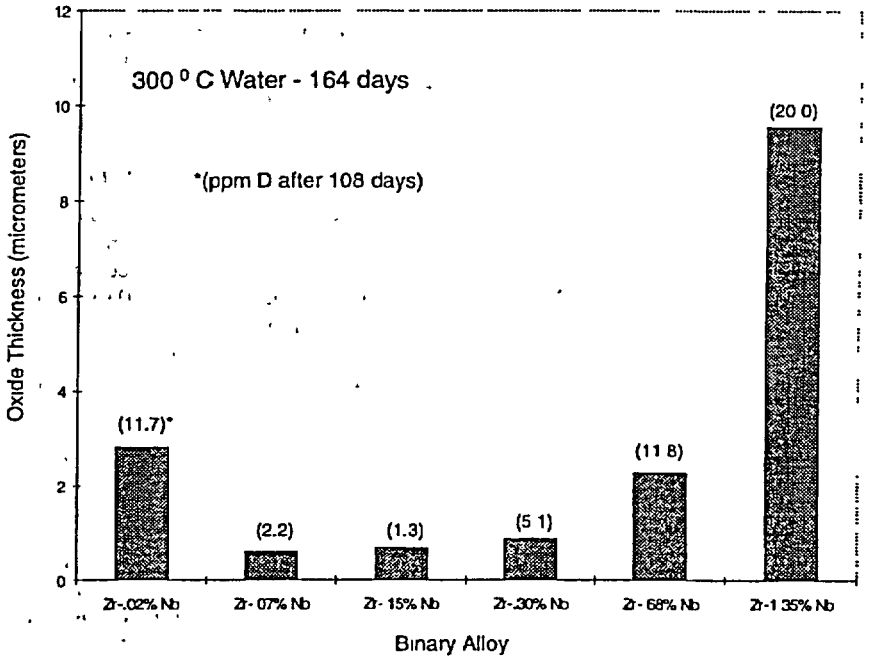

FIG. 5—*Effect of the Nb composition of the α-Zr phase on corrosion and deuterium ingress of Zr-2.5Nb binary alloys.*

Effect of Irradiation-Induced/Enhanced Microstructural Changes

Corrosion samples were prepared from irradiated pressure tubes that had been removed from operating reactors. The fluences of for these tubes ranged from 0.6×10^{25} to 10.4×10^{25} n/m/s^2. Results for zero fluence are for samples of pressure tube offcuts that are archive material from finished tubes just before they are installed. The results from post-irradiation corrosion tests in autoclaves in 300°C deoxygenated water are shown in Fig. 6. The corrosion of pre-irradiated material is lowered as a consequence of the reactor irradiation. The reduction in corrosion response appears to saturate after a fluence of about 1.5×10^{25} n/m^2; however, more testing is required before any definitive statement can be made with regard to an apparent increase for high-fluence samples. Also shown for comparison is the result for an electron-irradiated sample exposed under identical test conditions [5].

One of the primary effects of irradiation is to produce dislocation loops in the α-phase. The evolution of these loops was monitored as a function of fluence by measuring the X-ray diffraction line-broadening [2–4]. In Fig. 7, prism plane line-broadening shows that the dislocation loop structure evolves rapidly, initially reaching a steady-state density that is primarily a function of temperature. The steady-state condition is achieved after a fluence of about 0.5×10^{25} n/m^{-2} and corresponds with a dislocation density of about 8×10^{14} m^{-2} at the inlet temperature of about 250°C and 6×10^{14} m^{-2} at the outlet temperature of about 300°C.

During the course of irradiation, the partially decomposed β-Zr phase evolves to a steady-state condition (measured from the concentration of Nb in the beta-phase) depending on the

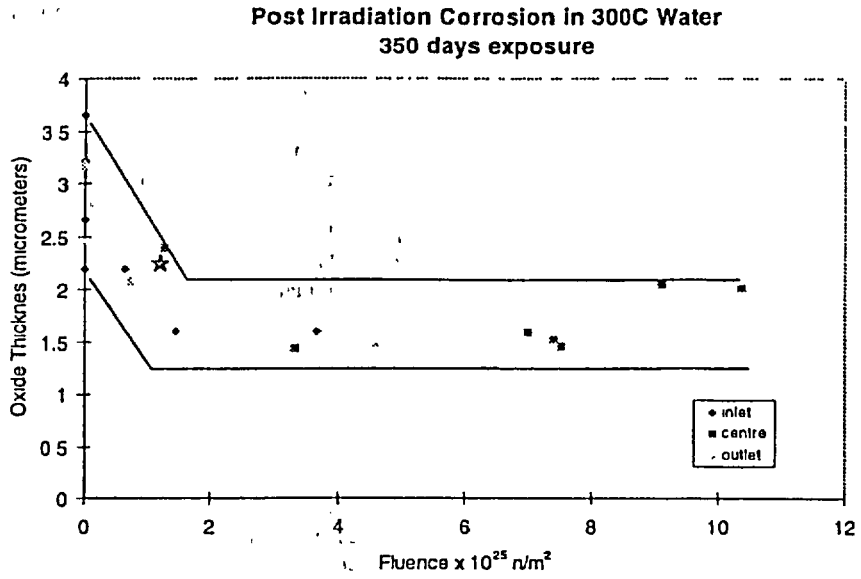

FIG. 6—*Effect of fluence on out-reactor post-irradiation corrosion for Zr-2.5Nb pressure tubes originally irradiated in CANDU reactors (★ denotes pressure tube material irradiated with electrons)*

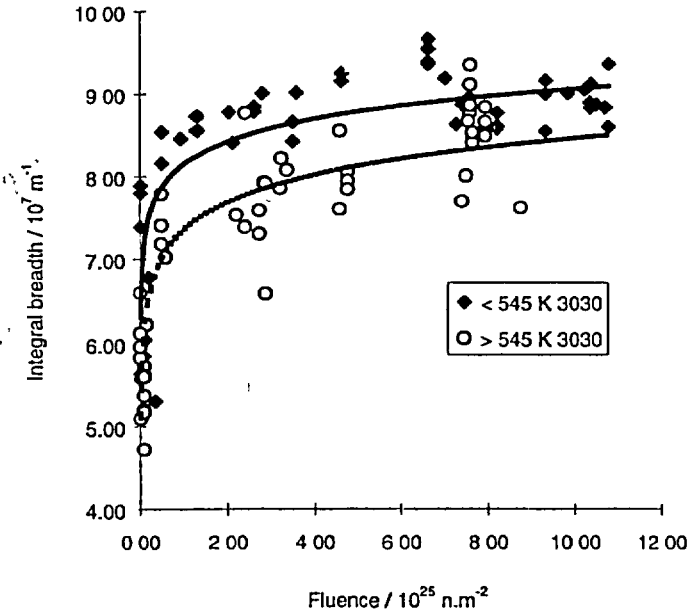

FIG. 7—*Variaton in ⟨a⟩-dislocation density (measured as an integral breadth) for Zr-2.5Nb pressure tubing as a function of fluence in CANDU reactors.*

temperature and flux, Fig. 8. The temperature increases from about 250°C at the inlet to about 300°C at the outlet of a CANDU pressure tube. At the peak flux in a CANDU reactor (about 2×10^{17} n/m^{-2}/s^{-1}), for temperatures between 250 and 300°C, the initial decomposition introduced by autoclaving (as measured by XRD, [4]) is unchanged or reversed, Fig. 9. Although evidence for a reversal in state is not strong (measurement errors being typically <5%), reversal in the thermally decomposed state has been previously observed for well-characterized materials irradiated in controlled reactor conditions [4]. As the flux drops at each end of the tubes, (i.e., where the fluences are low), the β-Zr phase is more decomposed compared to the initial condition As the temperature increases towards the outlet, the thermal decomposition dominates even though the flux may be significant.

The other main microstructural feature that changes during irradiation is the chemical distribution of the α-phase. Irradiation results in the production of small (2 to 5 nm) Nb-rich precipitates visible after fluences approaching 1×10^{25} n/m^{-2} at 300°C, Fig. 10. Although it is difficult to estimate how the number density of precipitates varies with temperature and fluence (due to difficulties in measuring foil thicknesses for small-grained irradiated material) the size of the precipitates increases with fluence, increasing from <3 nm in diameter at 1×10^{25} n/m^{-2} to between 5 and 10-nm diameter for fluences $> 5 \times 10^{25}$ n/m^{-2} at 300°C. Precipitation is more apparent at 300°C compared with 250°C for similar fluences [6], indicating that there is a slight temperature dependence for precipitation. These β-Nb precipitates are stable during post-irradiation thermal treatment at 500°C, indicating that they are a stable phase at temperatures ≤500°C (Fig. 11).

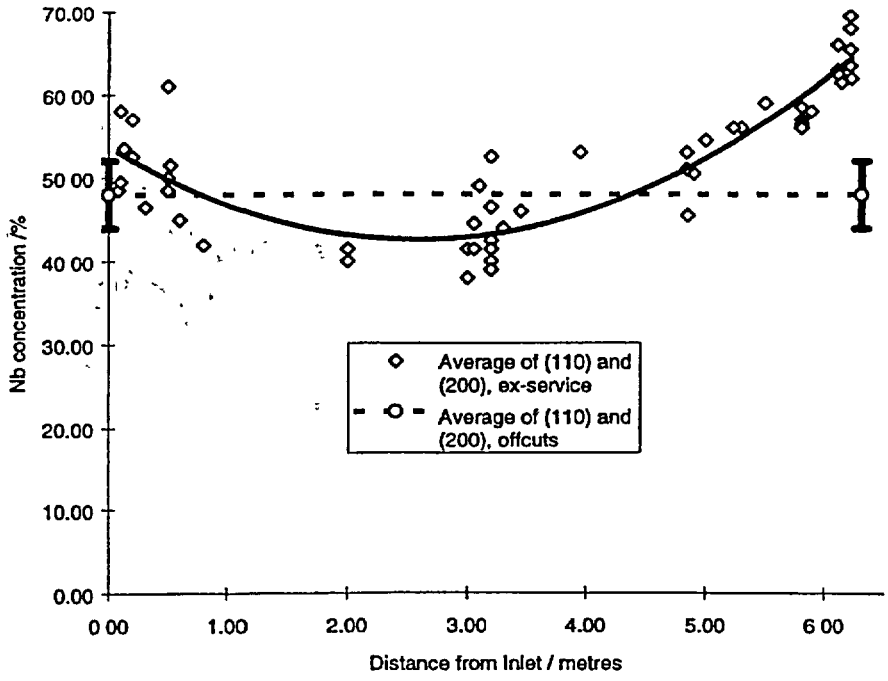

FIG. 8—*Nb concentration in the β-phase of Zr-2.5Nb pressure tubes as a function of position relative to the inlet in CANDU reactors.*

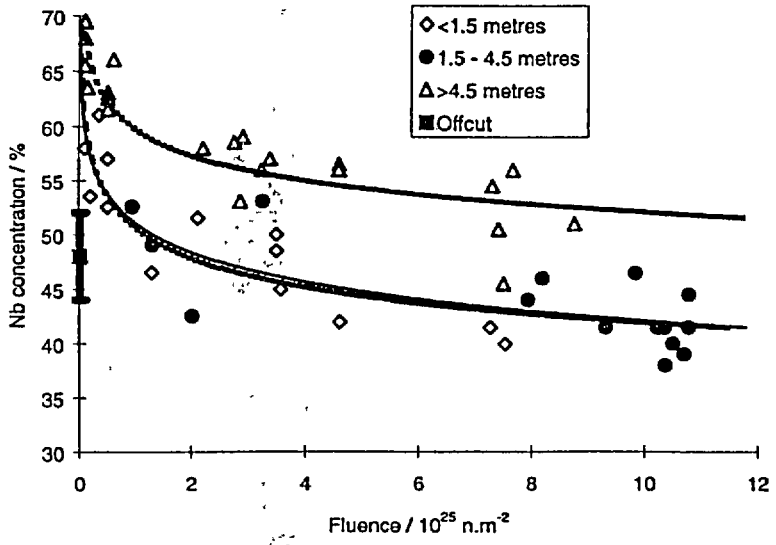

FIG. 9—*Nb concentration in the β-phase of Zr-2.5Nb pressure tubes as a function of fluence at inlets, centers, and outlets in CANDU reactors.*

Direct measurement of the composition of these small precipitates, or the composition of the matrix (irradiated and unirradiated), in an electron microscope is subject to large experimental errors. However, their composition can be measured indirectly from the α-phase lattice parameters. As Nb is an undersized solute [7], the lattice parameters decrease with increasing Nb content and vice-versa. Measurements using neutron diffraction on samples

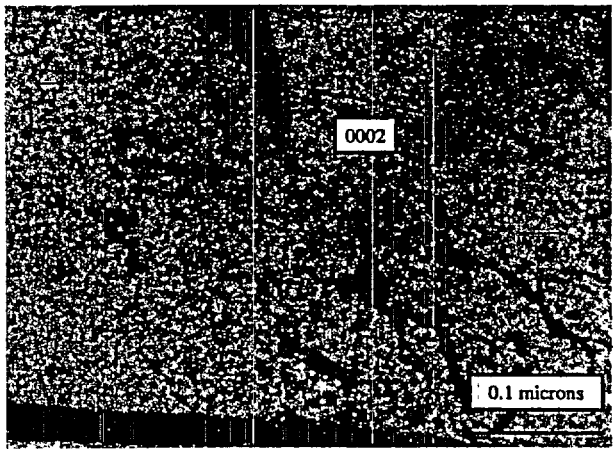

FIG. 10—*Micrographs showing β-Nb precipitates (arrowed) in Zr-2.5Nb irradiated at 573 K to a fluence of* 0.9×10^{25} *n/m*$^{-2}$.

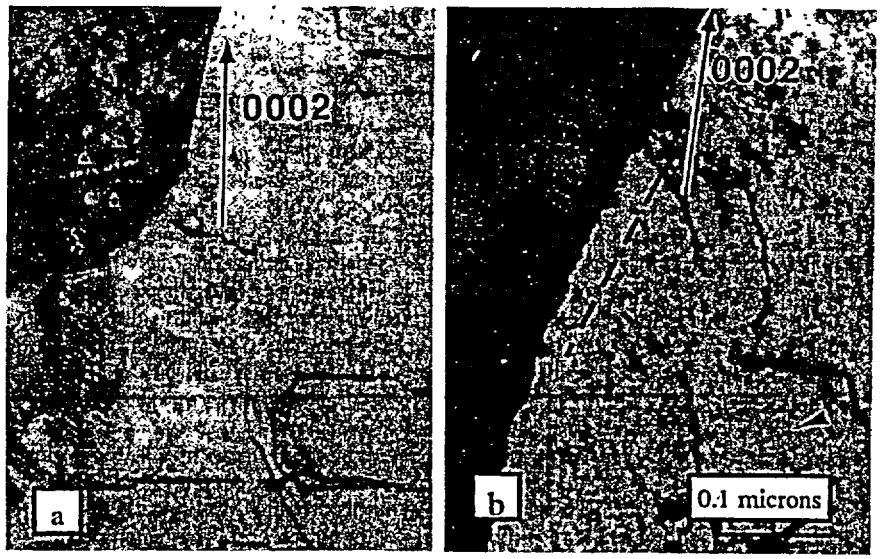

FIG. 11—*Effect of irradiation on Nb precipitation (arrowed in* (b) *in Zr-2.5Nb pressure tubing;* (a) *unirradiated;* (b) *irradiated at 546 K to a fluence of 6.2 × 10^{25} n/m^{-2} plus 1 h at 773 K. The denuded zone at the grain boundary (dotted line) is about 30 mm.*

tested in this study showed that the lattice strains of each irradiated sample increased relative to the unirradiated state, and the change was consistent with a decrease in Nb concentration of about 0.3 wt% using low Nb standards (Table 2).

Discussion

Following forging and fabrication into hollow billets, Zr-2.5Nb pressure tubes are extruded at temperatures of about 815°C in a range where both the α-Zr and β-Zr phases are stable. Examination of the metal-oxide interface regions of pressure tube material after oxidation has shown thicker oxide ridges penetrating into the β-Zr phase in those structures. Therefore, greater amounts of β-Zr phase in two-phase structures have a negative impact on corrosion and deuterium pickup (Fig. 2). Despite the high corrosion, pure β-Zr shows remarkably low deuterium pickup, which seems to be associated with the formation of a more homogeneous

TABLE 2—*Lattice strain measurements measured by neutron diffraction, averaged over six different reflections, for irradiated pressure tube samples relative to unirradiated offcuts*

Sample	Tempeature/°C	Fluence (× 10^{25} m/m^{-2})	Strain, 10-4
P4F17	269	1.3	3.7 ± 0 6
B2X14	286	3.03	4 2 ± 0 6
P4N16	267	7.25	3 5 ± 0 6
P3J09	268	7 56	3.3 ± 0 6

oxide compared to more heterogeneous and porous oxides that form on the two-phase α-Zr + β-Zr structures [8].

Pressure tubes are cold drawn about 27% to attain their final wall thickness. The ends of the tubes experience an additional 12 to 13% cold work when the mechanical rolled joints are made with the stainless steel end-fitting during installation into the reactor. The implication from Fig. 3 is that there would be a slight benefit of this rolling on corrosion at the pressure tube ends where the neutron flux is negligible. The reason for the observed corrosion reduction with cold work is not completely understood. Work on Zircaloy-2 indicates that cold-working up to 40% does not significantly alter the corrosion and H uptake characteristics [9]. It is possible that cold-working in a binary Zr-Nb alloy such as Zr-2.5Nb could enhance the precipitation of Nb from supersaturated solid solution either during thermal aging (which would occur to some extent during a corrosion test) and that this could lead to an improvement in corrosion properties [1]. However, in-reactor the impact of irradiation-induced effects is so overwhelming that the dependence on cold work seen out of flux is not observed. Thus, any requirement for a reduction in cold work, for example, to help mitigate pressure tube creep, would not affect the corrosion behavior of the tubes.

Pressure tubes are given a final stress relief treatment in steam at 400°C. During this treatment the metastable β-Zr phase will undergo some thermal decomposition with further decomposition occurring during service. From Fig. 4 this thermal decomposition is beneficial, contributing to reductions in both corrosion and deuterium pickup. The benefit is likely due to the decomposition of the metastable β-Zr phase, leading to a smaller volume fraction of total β-phase [10]. However, any change in volume fraction due to one 24-h heat treatment at 400°C is small and is unlikely to be significant relative to other factors affecting long-term corrosion, primarily α-phase composition.

In the as-fabricated condition, the α-Zr platelets are supersaturated with respect to Nb, containing between 0.6 and 1.0 wt% Nb, amounts that are established by the fabrication process and the Zr-Nb phase diagram. At reactor operating temperatures, Nb solubility is lower so there is the potential for β-Nb precipitation to occur with a concomitant reduction in the matrix Nb concentration. The results from Fig. 5 suggest that, if this process does occur, the associated reduction in matrix concentration contributes to a reduction in the corrosion and deuterium uptake.

The reduction in corrosion observed on pre-irradiated pressure tube material, Fig. 6, is a result of changes that occurred to the base metal structure during service under irradiation. The increased dislocation density during irradiation (Fig. 7) is consistent with the improvements in corrosion resistance due to cold-working. However, it is probable that any improvement due to the increased dislocation density is due to the enhancement of precipitation of Nb, especially given the results of tests on material irradiated at high temperatures showing evidence for improved corrosion resistance in materials where Nb has precipitated but in the absence of dislocation loops [5].

X-ray diffraction measurements show that the thermal decomposition of the β-phase is suppressed during irradiation and even reversed at a sufficiently low temperature and sufficiently high flux [4] (Fig. 8). The change in state of the β-phase with increasing fluence (Fig. 9) occurs over the same fluence range as the change in corrosion properties (Fig. 6). However, the effect of irradiation is to increase, rather than decrease, the volume fraction of metastable β-Zr [4], and there is a significant difference at the inlets compared with outlets; neither of these factors are consistent with the corrosion data (Figs. 2 and 6). Therefore, it is unlikely that changes to the β-phase during irradiation are responsible for the improvement in corrosion properties and may, in fact, have a negative impact on corrosion.

During irradiation, not only does the state of the β-Zr phase change with time, but the Fe, initially segregated in the β-Zr phase, is dispersed into the α-Zr phase [2–4]. The matrix

iron concentration is gradually increased over a fluence range of about 2×10^{25} n/m^{-2}. Again, comparison with other work on Zircaloys [*11*] suggests that an increase in the amount of Fe dispersed in the α-phase results in increased uniform corrosion and therefore is unlikely to have anything other than a negative impact on corrosion resistance in this case unless there are synergistic effects with Nb that are different from those with Sn.

The main factor leading to improvement in corrosion properties in Zr-2.5Nb pressure tubing in-reactor then appears to be the reduction in Nb content in the α-phase due to the precipitation of β-Nb precipitates. In this respect, dislocations introduced by cold-work and dislocation loops produced by irradiation probably play a role in assisting nucleation of Nb from solution. The rate of precipitation during irradiation is a balance between irradiation-induced mixing causing shrinkage and radiation-enhanced diffusion-causing growth [*12*]. Previous work [*13*] has shown that precipitation occurs inhomogeneously (at dislocations) during irradiation at 500°C but is not observed during thermal treatment at the same time and temperature in the absence of irradiation. In the same work [*13*], post-irradiation annealing at 500°C of material that had previously been irradiated at 300°C showed that the β-Nb precipitates coarsened, indicating that Nb mobility was not a limiting factor for Nb precipitation during thermal treatments at temperatures of about 500°C, this is consistent with rate-theory calculations.

During irradiation, the concentrations of point defects in a metal are given by the following rate equations:

$$G - k^2(v)\, D(v)C(v) - RC(v)\, C(i) = \dot{C}\,(v) \tag{1}$$

$$G - k^2(i)\, D(i)C(i) - RC(v)\, C(i) = \dot{C}\,(i) \tag{2}$$

where $k^2(v)$ and $k^2(i)$ are the sink strengths of various microstructural features such as a-type and c-type dislocations and grain boundaries, $D(v)$ and $D(i)$ are the diffusion coefficients, and $C(v)$ and $C(i)$ are the point defect concentrations for vacancies and interstitials, respectively. G is the damage production rate, and R is a recombination rate parameter [*14*].

After an initial transient in microstructure evolution (due mainly to a-type dislocation loop formation for fluences $< 1 \times 10^{25}$ n/m^{-2}), any further evolution of the sink structure occurs primarily by climb of existing defects and slowly varies with time. At any one instant in this regime, one can assume that the sink strength is constant, as the time taken for the point defect concentrations to reach steady-state values is very small compared with the rate of change in the sink structure. In these circumstances the steady-state point defect concentrations satisfy the following simultaneous equations:

$$G - k^2(v)\, D(v)C(v) - RC(v)C(i) = 0 \tag{3}$$

$$G - k^2(i)\, D(i)C(i) - RC(v)C(i) = 0 \tag{4}$$

Solving these equations using appropriate temperature-dependent sink densities relevant to Zr-2.5Nb pressure tubes yields values for steady-state point defect concentrations From the vacancy concentrations, the effect on thermal diffusion coefficients of Nb Zr in α-Zr [*15*] can be calculated. From the diffusion coefficients, values for mean-free paths of Nb and Zr for a typical CANDU reactor irradiation lasting one year have been calculated and are plotted in Fig. 12. Also shown in Fig. 12 are similar plots for Zr to illustrate that Nb has a higher diffusion rate compared with Zr self-diffusion. The graph shows that at 500°C thermal diffusion dominates any irradiation enhancement. It also shows that at reactor operating temperatures of about 250 to 300°C, the mean-free path for Nb is about 10 nm, which is

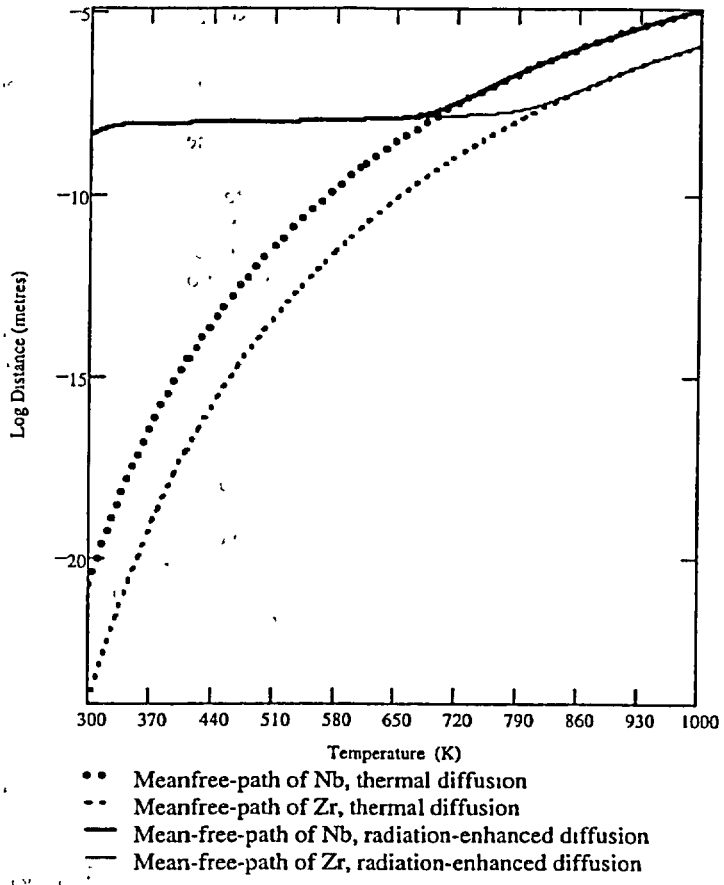

FIG. 12—*Mean-free path calculation for Zr-Nb alpha phase for one year irradiation, i e , for a fluence of about 0.7 × 10^{25} n/m^{-2} at the center of a CANDU reactor.*

comparable with the denuded zone width for β-Nb precipitates close to grain boundaries (Fig. 11). These calculations imply that thermal diffusion at 500°C dominates any irradiation enhancement of diffusion. Therefore, a reduction of Nb concentration in the supersaturated α-phase could be achieved by thermal treatment at this temperature. The fact that precipitation is not observed during thermal treatment at 500°C implies that either the degree of undercooling is insufficient to induce precipitation or that the diffusion to existing sinks such as grain boundaries is sufficiently rapid to suppress any precipitation within the grains. However, the observation of precipitation during irradiation at 500°C but not during thermal treatment at the same temperature [*13*] indicates that irradiation introduces an added factor favoring precipitation. This could be the formation of jogs on existing dislocations or through the creation of an irradiation-induced supersaturation of Nb interstitial atoms that form clusters more easily than substitutionally diffusing species.

Conclusions

Out-reactor corrosion tests on dual-phase Zr-Nb alloys with controlled microstructures show that one of the most important factors affecting the corrosion properties the thermodynamic state of the α- and β-phases present. At equilibrium, the volume fraction of the β-phase and the concentration of Nb in the α-phase is minimized, resulting in lower corrosion rates. For Zr-2.5Nb pressure tubing operating in CANDU reactors, the most important factor leading to reduced corrosion rates is the precipitation of β-Nb particles and the concomitant reduction of Nb in the matrix of the α-Zr grains during irradiation.

Precipitate formation occurs as a result of a complex combination of factors: degree of supersaturation, density of nucleation sites, and diffusion rate (dependent on neutron flux and temperature). For CANDU reactor fluxes and temperatures, the irradiation enhancement of diffusion dominates over thermal diffusion, and the reduction in Nb concentration is assisted by precipitate formation at sinks.

Acknowledgments

This work was made possible by the collaboration of many groups at AECL, including L. Woodworth and D. Nye at the Whiteshell Laboratory, and at the Chalk River Laboratory: A. Shaddick, R. Resmer, and T. G. Lamarche for the corrosion experiments and deuterium analyses; P. Clarke for the neutron diffraction measurements; J. F. Mecke and J E. Winegar for the X-ray diffraction measurements; and D. Phillips for preparation of transmission electron microscopy specimens.

References

[1] Urbanic, V. F. and Gilbert, R W, "Effect of Microstructure on the Corrosion of Zr-2.5Nb Alloy," IAEA Technical Committee Meeting on Fundamental Aspects of Corrosion of Zirconium Based Alloys," Portland, OR, 1989

[2] Griffiths, M., Chow, C. K., Coleman, C. E, Holt, R. A, Sagat, S., and Urbanic, V. F., "Evolution of Microstructure in Zr-Alloy Core Components during Service," *Effects of Radiation on Materials (16th Vol), ASTM STP 1175,* 1993, p. 1077, Issued as AECL 10844, COG-92-54

[3] Urbanic, V F. and Griffiths, M, "Corrosion Response of Pre-irradiated Zr-2.5Nb Pressure Tube Material," *Effects of Radiation on Materials· 17th International Symposium, ASTM STP 1270,* D. S. Gelles, R. K. Nanstad, A S. Kumar, and E A Little, Eds, American Society for Testing and Materials, West Conshohocken, PA, 1996, pp. 1088–1106.

[4] Griffiths, M., Mecke, J F., and Winegar, J E, "Evolution of Microstructure in Zirconium Alloys during Irradiation," *Zirconium in the Nuclear Industry: Eleventh International Symposium, ASTM STP 1295,* E R. Bradley and G P. Sabol, Eds., American Society for Testing and Materials, West Conshohocken, PA, 1996, pp. 580–602 Also as AECL Report RC-1477

[5] Woo, O. T. et al, "Corrosion of Electron-Irradiated Zr-2 5Nb and Zircaloy-2," this publication

[6] Hosbons, R. R. et al., "Effect of Long-term Irradiation on the Fracture Properties of Zr-2 5Nb Pressure tubes," this publication

[7] Douglas, D. L, "The Physical Metallurgy of Zirconium," *International Atomic Review,* IAEA, Vienna, 1971.

[8] Urbanic, V. F., Chan, P. K, Khatamian, D, and Woo, O. T., "Growth and Characterization of Oxide Films on Zirconium-Niobium Alloys," *Zirconium in the Nuclear Industry· Tenth International Symposium, ASTM STP 1245,* A. M. Garde and E. R. Bradley, Eds, American Society for Testing and Materials, Philadelphia, PA, 1994, pp 116–130.

[9] Burns, W. A. and Maffei, H. P., "Neutron Irradiation and Cold Work Effects on Zircaloy-2 Corrosion and Hydrogen Pickup," *ASTM STP 368,* 1963, pp. 101–117.

[10] Urbanic, V. F, Warr, B. D, Manolescu, A., Chow, C K., and Shanahan, M. W., "Oxidation and Deuterium Uptake of Zr-2.5Nb Pressure Tubes in CANDU-PHW Reactors," *Zirconium in the Nuclear Industry· Eighth International Symposium, ASTM STP 1023,* L. F. P Van Swam and C. M. Eucken, Eds, American Society for Testing and Materials, Philadelphia, PA, 1989, pp. 20–34.

[11] Huang, P. Y., Mahmood, S. T, and Adamson, R. B., "Effects of Thermomechanical Processing on In-reactor Corrosion and Post-irradiation Mechanical Properties of Zircaloy-2," *Zirconium in the Nuclear Industry: Tenth International Symposium, ASTM STP 1295,* E R. Bradley and G P Sabol, Eds., American Society for Testing and Materials, West Conshohocken, PA, 1996, pp. 726–757.

[12] Nelson, R. S, Hudson, J. A, and Mazey, D. J, "The Stability of Precipitates in an Irradiation Environment," *Journal of Nuclear Materials,* Vol. 44, 1972, pp. 318–330.

[13] Coleman, C E, Gilbert, R. W., Carpenter, G J C, and Weatherley, G. C., "Precipitation in Zr-2.5 wt% Nb During Neutron Irradiation in Phase Stability During Irradiation," J. R. Holand, L K. Mansur, and D. I. Potter, Eds, from *Phase Stability During Irradiation,* The Metallurgical Society of AIME, Pittsburgh, PA, 1981, pp. 587–599.

[14] Heald, P. T. and Speight, M. V., "Point Defect Behavior in Irradiated Materials," *Acta Metallurgica,* Vol. 23, 1975, p 1389

[15] Hood, G. M., "Nb-Diffusion in Single-crystal α-Zr," AECL report, RC-1674

DISCUSSION

B. Cox[1] (*written discussion*)—In your plot of post-irradiation corrosion rate as a function of neutron fluence you interpreted the results as a reduction with fluence followed by a plateau. A line through the actual plots would suggest a minimum in the curves. Is it reasonable to expect a minimum from other observations?

V. Urbanic et al (*authors' closure*)—The observed reduction in the corrosion response with fluence is significant and most obvious and we argue in this paper that microstructural changes occurring in the α-Zr phase are largely responsible for this behavior. As you point out, the data suggest that there may be a minimum in the response although we have indicated that the observed reduction with fluence is followed by a plateau. One might argue the possibility for a minimum based on the following. Figure 3 shows that corrosion is reduced as the β-Zr phase is decomposed The date of Figs. 7 and 8 illustrate that decomposition of the β-Zr phase is reversed under irradiation. Thus, there is the possibility that the two data points at the highest fluence are showing an upward trend for this reason. However, we feel that additional exposures for these samples and on new samples with even higher fluences are required before a legitimate claim for a minimum in the response can be made.

R. Adamson[2] (*written discussion*)—What ideas do you have on *why* the effects of Nb on corrosion are as you describe them?

V Urbanic et al. (*authors' closure*)—The results of tests on dilute binary alloys show a minimum in corrosion around 0.1 wt% Nb. The solubility of Nb in Zr at 883 K is about 0.6 to 1.0 wt%. It is recognized that the solubility decreases with decreasing temperature; however, such data at lower temperatures is limited. Despite this, it is thought that the optimum behavior at about 0 1 wt% Nb may be related to the fact that this could be close to the solubility limit of Nb in Zr at the corrosion tests temperature of 573 K.

Y. Hatano[3] (*written discussion*)—Did you examine the chemical form of Nb in the oxide film?

V. Urbanic et al. (*authors' closure*)—In this work the chemical form of Nb in the oxide film was not investigated. However, we have investigated the chemical state of Nb in oxide films formed on Zr-20wt%Nb (the β-Zr phase composition) in earlier work (*ASTM STP 1245*). In that work there was evidence from XPS analyses for predominantly Nb^{+5} at the outer oxide regions. Within the oxide, niobium existed in the Nb^{5+} and Nb^{2+} states; however, evidence for its existence in the valence state lower than 2^+ was also found.

[1] University of Toronto, Toronto, Ont., Canada
[2] GE NE, Pleasanton, CA.
[3] Toyama University, Toyama, Japan